DEVELOPMENT OF NANOCOMPOSITE ELECTRODES AND SEPARATORS FOR SUPERCAPACITORS

A THESIS SUBMITTED TO
THE GRADUATE SCHOOL OF NATURAL AND APPLIED SCIENCES
OF
MIDDLE EAST TECHNICAL UNIVERSITY

BY

ALPTEKİN AYDINLI

IN PARTIAL FULFILLMENT OF THE REQUIREMENTS
FOR
THE DEGREE OF DOCTOR OF PHILOSOPHY
IN
METALLURGICAL AND MATERIALS ENGINEERING

FEBRUARY 2022

Approval of the thesis:

DEVELOPMENT OF NANOCOMPOSITE ELECTRODES AND SEPARATORS FOR SUPERCAPACITORS

submitted by **ALPTEKİN AYDINLI** in partial fulfillment of the requirements for the degree of **Doctor of Philosophy** i**n Metallurgical and Materials Engineering, Middle East Technical University** by,

Prof. Dr. Halil Kalıpçılar
Dean, Graduate School of **Natural and Applied Sciences** _____

Prof. Dr. Cemil Hakan Gür
Head of the Department, **Metallurgical and Materials Eng.** _____

Prof. Dr. Hüsnü Emrah Ünalan
Supervisor, **Metallurgical and Materials Eng., METU** _____

Examining Committee Members:

Prof. Dr. Ali Çırpan
Chemistry, METU _____

Prof. Dr. Hüsnü Emrah Ünalan
Metallurgical and Materials Eng., METU _____

Prof. Dr. Tayfur Öztürk
Metallurgical and Materials Eng., METU _____

Prof. Dr. Zeki Aktaş
Chemical Engineering, Ankara University _____

Assoc. Prof. Dr. Burak Ülgüt
Chemistry, İhsan Doğramacı Bilkent University _____

Date: 10.02.2022

I hereby declare that all information in this document has been obtained and presented in accordance with academic rules and ethical conduct. I also declare that, as required by these rules and conduct, I have fully cited and referenced all material and results that are not original to this work.

Name Last name: Alptekin Aydınlı

Signature:

ABSTRACT

DEVELOPMENT OF NANOCOMPOSITE ELECTRODES AND SEPARATORS FOR SUPERCAPACITORS

Aydınlı, Alptekin
Doctor of Philosophy, Metallurgical and Materials Engineering
Supervisor: Prof. Dr. Hüsnü Emrah Ünalan

February 2022, 178 pages

Supercapacitors or electrochemical capacitors are known as one of the most promising energy storage systems for the 21st century. Having the potential to complement batteries, supercapacitors have received a lot of attention thanks to their high specific power and moderate energy densities. Supercapacitors have various application areas ranging from electric vehicles to portable systems and devices. In particular, their fast charge-discharge feature enables integration with consumer electronics, mobile devices and renewable energy systems. The widespread use of supercapacitors in many other electronic systems may also be possible if they gain new functions, such as flexibility, textile integration, environmentally friendly components and charge level indication. Supercapacitor electrodes with these multifunctional properties will be notable for both industrial and commercial applications.

The use of nanocomposite electrode materials is very attractive for supercapacitors. Many studies have been carried out to improve the performance of supercapacitors using nanocomposites and a wide knowledge has been gained in this

area. However, there are still many unknowns due to the variety of the combinations of the nanocomposite materials, and therefore further studies in this area ae required.

In this thesis study, carbon nanotube-polyaniline, expanded graphite-polypyrrole, carbon nanoflake-manganese dioxide, reduced graphene oxide-molybdenum disulfide and hexagonal boron nitride-molybdenum disulfide nanocomposites are investigated as active materials for supercapacitor electrodes. In addition, hexagonal boron nitride-polyvinyl alcohol nanocomposites are investigated as separators for supercapacitors. The use of nanocomposite materials has improved many performance characteristics of supercapacitors compared to pure components. Therefore, it is concluded that the commercialization of nanocomposite-based supercapacitors will continue to become widespread in the coming years.

Keywords: Supercapacitors, Nanocomposites, Energy Storage, Electrodes, Separators

ÖZ

SÜPERKAPASİTÖRLER İÇİN NANOKOMPOZİT ELEKTROTLAR VE AYIRAÇLARIN GELİŞTİRİLMESİ

Aydınlı, Alptekin
Doktora, Metalurji ve Malzeme Mühendisliği
Tez Yöneticisi: Prof. Dr. Hüsnü Emrah Ünalan

Şubat 2022, 178 sayfa

Süperkapasitörler ya da elektrokimyasal kapasitörler 21. yüzyılın en çok umut vadeden enerji depolama sistemlerinden biri olarak bilinmektedir. Bataryaları tamamlama potansiyeline sahip süperkapasitörler yüksek özgül güç ve dikkate değer enerji yoğunlukları sayesinde çok fazla ilgi görmüşlerdir. Süperkapasitörlerin elektrikli araçlardan taşınabilir sistemlere ve cihazlara kadar çok çeşitli uygulama alanları bulunmaktadır. Bilhassa hızlı şarj-deşarj olma özelliği süperkapasitörlerin tüketici elektroniği, taşınabilir cihazlar ve yenilenebilir enerji sistemlerinde yer almasını mümkün kılmaktadır. Süperkapasitörlere esneklik, kumaşa uyum, çevre dostu bileşenler ve renk göstergesi gibi yeni işlevler kazandırılabilirse daha birçok elektronik sistemde yaygınlaşması söz konusu olabilecektir. Bu türden çoklu işlevsel özelliklere sahip süperkapasitörler hem sanayide hem de ticari uygulamalarda ilgi odağı olacaktır.

Süperkapasitörlerde nanokompozit elektrot malzemelerinin kullanımı oldukça ilgi çekicidir. Süperkapasitörlerin nanokompozitler kullanılarak performanslarının geliştirilmesi için çok sayıda çalışma yürütülmüştür ve bu alanda geniş bir bilgi birikimi oluşmuştur. Ancak, nanokompozit malzemelerin çok çeşitli

kombinasyonları sebebiyle bu alanda halen birçok bilinmeyen mevcuttur ve bundan dolayı çalışmaların devam etmesi gerekmektedir.

Bu tez çalışmasında, karbon nanotüp-polianilin, genişletilmiş grafit-polipirol, karbon nanopul-mangan dioksit, indirgenmiş grafen oksit-molibden disülfit ve hegzagonal bor nitrür-molibden disülfit nanokompozitleri süperkapasitör elektrotları için etkin malzeme olarak incelenmiştir. Bunlara ek olarak, hegzagonal bor nitrür-polivinil alkol nanokompoziti ise süperkapasitörler için ayıraç olarak incelenmiştir. Nanokompozit malzemelerin kullanılması saf bileşenlere kıyasla süperkapasitörlerin birçok performans karakteristiğini geliştirmiştir. Bu sebeple, önümüzdeki yıllarda nanokompozit temelli süperkapasitörlerin ticarileşmesinin yaygınlaşmaya devam edeceği sonucuna varılmıştır.

Anahtar Kelimeler: Süperkapasitörler, Nanokompozitler, Enerji Depolama, Elektrotlar, Ayıraçlar

Dedicated to my Family, Wife and Daughter…

ACKNOWLEDGMENTS

Firstly, I wish to express my gratitude to my supervisor, Prof. Dr. Hüsnü Emrah Ünalan for his guidance, caring, patience, and providing me with an atmosphere for doing research. I also appreciate my thesis advisory committee members, Prof. Dr. Tayfur Öztürk and Assoc. Prof. Dr. Burak Ülgüt for their valuable contributions to complete my thesis. I also would like to thank my thesis defense jury members Prof. Dr. Ali Çırpan and Prof. Dr. Zeki Aktaş for their complementary suggestions.

In addition, I would also like to thank Prof. Dr. Yury Gogotsi for giving an opportunity to work in his research laboratory, Nanomaterials Group at Drexel University, his guidance and support during the research. I also thank other group members of Nanomaterials Group and especially Dr. Xuehang Wang for her mentorship.

I owe my deepest gratitude to my current and former lab-mates colleagues, Dr. Recep Yüksel, Dr. Şahin Coşkun, Dr. Yaqoob Khan, Dr. Farzaneh Hekmat, Dr. Asude Çetin, Dr. Duygu Tan, Dr. Aryan Azad, Dr. Pantea Aurang, Dr. Ümran Ceren Başköse, Serkan Koylan, Yusuf Tutel, Mete Batuhan Durukan, Doğa Doğanay, Loay Madbouly, Ögeday Çiçek, Caner Görür, Tufan Bölükbaşı, Onuralp Çakır, Deniz Keskin, Onur Demircioğlu, Öykü Çetin, Ali Deniz Uçar, Gözde Öztürk, Alptuğ Calasın, Hazal Başköy, Şensu Tunca, Sevim Polat, Doğancan Tigan, Ece Alpugan, Onur Türel, İpek Bayraktar, Selin Özkul, Elif Özlem Güner, Şeyma Koç, Itır Bakış Doğru, Ekim Saraç and Kazım Sömek.

I also want to thank my other friends at METU, Fatih Uzgur, Abdülmahit Dönder, Cemre Metin Poyraz, Gökhan Polat and Bayram Yıldız for their support.

Finally, I would also like to thank my family, my wife and my best friends Emre Bal and Kemal Ün for their support and encouragement. They were always there cheering me up and stood by me throughout the good times and the bad.

This thesis was partially supported by The Scientific and Technological Research Council of Turkey (TÜBİTAK) under a project with grant no 113E596 and TÜBİTAK 2214-A International Doctoral Research Fellowship Program with grant no 1059B141801094. This thesis was conducted under YÖK-ÖYP program.

TABLE OF CONTENTS

LIST OF TABLES

TABLES

LIST OF FIGURES

FIGURES

LIST OF ABBREVIATIONS

ABBREVIATIONS	
2D	Two-dimensional
3D	Three-dimensional
AC	Alternating current
Ag/AgCl	Silver/silver chloride
BET	Brunauer-Emmett-Teller
C_2H_2	Acetylene
CE	Coulombic efficiency
CE	Counter electrode
CNF	Carbon nanoflake
CNT	Carbon nanotube
Co_3O_4	Cobalt oxide
CP	Conducting polymer
CV	Cyclic voltammetry
CVD	Chemical vapor deposition
DC	Direct current
DMF	Dimethylformamide
EDLC	Electrical double-layer capacitor
EDS	Energy-dispersive X-ray spectroscopy
EG	Expanded graphite

EIS	Electrochemical impedance spectroscopy
ESR	Equivalent series resistance
Fe_2O_3	Iron(III) oxide
Fe_3O_4	Iron(II,III) oxide
FTIR	Fourier transform infrared spectroscopy
GCD	Galvanostatic charge discharge
GO	Graphene oxide
H_2O_2	Hydrogen peroxide
H_2SO_4	Sulfuric acid
H_3PO_4	Phosphoric acid
HNO_3	Nitric acid
ICP	Induction coupled plasma
IL	Ionic liquid
KCl	Potassium chloride
$KMnO_4$	Potassium permanganate
KOH	Potassium hydroxide
Li_2SO_4	Lithium sulfate
MnO_2	Manganese dioxide
$MnSO_4$	Manganese sulfate
MoO_2	Molybdenum dioxide
MoS_2	Molybdenum disulfide
Na_2SO_4	Sodium sulfate

Nb_2O_5	Niobium pentoxide
$Ni(OH)_2$	Nickel(II) hydroxide
NiO	Nickel oxide
PA	Polyacetylene
PANI	Polyaniline
PEDOT	Poly(3,4-ethylenedioxythiophene)
PET	Polyethylene terephthalate
PG	Potentiostat/galvanostat
PPV	Poly(p-phenylenevinylene)
PPy	Polypyrrole
PTFE	Polytetrafluoroethylene
PTh	Polythiophene
PVA	Polyvinyl alcohol
PVD	Physical vapor deposition
RC	Resistor-capacitor
RE	Reference electrode
RF	Radio frequency
rGO	Reduced graphene oxide
RT	Room temperature
RuO_2	Ruthenium dioxide
SEM	Scanning electron microscopy
SWG	Signal waveform generator

$Ti_3C_2T_x$	Titanium carbide
TiO_2	Titanium dioxide
TiS_2	Titanium disulfide
TMD	Transition metal dichalcogenide
V_2O_5	Vanadium pentoxide
VACNT	Vertically aligned carbon nanotube
WE	Working electrode
WSe_2	Tungsten diselenide
XPS	X-ray photoelectron spectroscopy
XRD	X-Ray powder diffraction

LIST OF SYMBOLS

SYMBOLS

$C_{-/+}$	Capacitance for negative/positive electrodes
C_{sp}	Specific capacitance
E	Potential
P_{max}	Maximum power
$R_{f-/+}$	Faradic resistance for negative/positive electrodes
R_S	Equivalent series resistance
t	Time
$Z^{'}$	Real part of impedance
ω	Frequency

CHAPTER 1

INTRODUCTION

1.1 General Properties of Supercapacitors

1.1.1 Definition of a Supercapacitor as an Energy Storage System

A supercapacitor or an electrochemical capacitor is a special kind of capacitor for which the charging and discharging processes occur at the electrode-electrolyte interface [1]. The basic principles of conventional capacitors can also be applied to supercapacitors. Rapid storage and deliver of energy observed in supercapacitors are quite notable compared to conventional capacitors. Electrodes with high specific surface area and thin dielectric separators, which are widely used in supercapacitors, improve both the charge storage capacity and energy. Thus, while conventional capacitors are generally assessed in the millifarad and microfarad ranges, supercapacitors can provide as large as tens, hundreds, and even thousands of farads per device. They can still be charged and discharged highly reversibly, as in conventional capacitors. They retain a low equivalent series resistance (ESR) and are used at high specific powers, substantially higher compared to most batteries [2]. Figure 1.1 demonstrates the graph of power versus energy density, also named as Ragone plot [3], positions the most prominent energy storage devices and supercapacitors in literature. As can be seen, supercapacitors currently fill the gap between conventional capacitors and batteries [4].

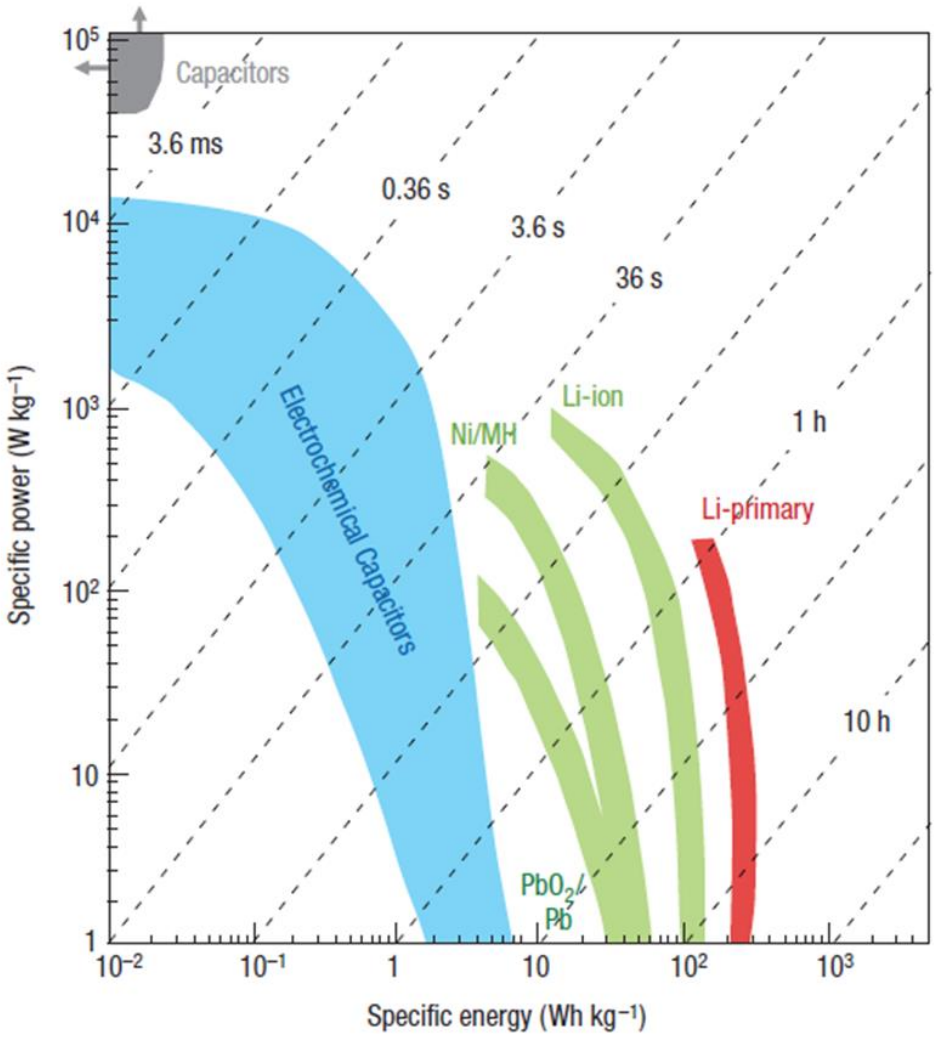

Figure 1.1. Ragone plot for different electrical energy storage systems. Times seen are the time constants of the devices, calculated through dividing the energy density by the power [4].

1.1.1.1 History of Supercapacitors

Invention of the Leyden jar and the determination of the charge storage principles and charge separation on the surfaces of the Leyden jar were remarkable advances for electricity physics and depending on this, for electrical, electronic and electrochemical applications. The Leyden jar was first referred to as a “condenser” in early studies to the middle of the previous century. The device was then referred to as a “capacitor” on different platforms and its property of charge storage per

potential was named as its “capacitance”. The term “capacity” preferred in battery applications to express the magnitude of Faradaic charge storage (watt-hours) is not the same as the term of “capacitance” (farads) which is preferred for capacitors [1].

The fact that electrical charge can be stored in an electrical double-layer contained in a capacitor has been known since the late 19th century. The use of this phenomenon in electrical energy storage was first suggested in 1957 by a patent granted to H. I. Becker of General Electric; but this device was never commercialized. Then, in 1978, prototypes owned by Standard Oil of Ohio (SOHIO) provided a commercial product proposed by the Nippon Electric Corporation (NEC), which was used to supply backup power for computer memories as battery complements [5].

A separate concept was used and improved in late 1970s and early 1980s by Conway. This concept was exampled with so-called “pseudocapacitance” related to solid oxide redox systems particularly observed over 1.4 V in aqueous sulfuric acid (H_2SO_4) at ruthenium dioxide (RuO_2) films. The high capacitance values (in the level of several or more F/g), which can be seen in the RuO_2 films and also capacitors with a carbon double-layer received names as “supercapacitor” or “ultracapacitor”. Moreover, in recent years as a more general term, “electrochemical capacitor” has been proposed for these devices. But this term should not be confused with “electrolytic capacitor”, which represents a well-known device containing a thin film oxide dielectric composed of gel electrolyte on metals such as aluminum, zirconium, titanium, and tantalum [1].

1.1.1.2 Capacitor and Supercapacitor Principles

A capacitor is a passive device that stores charges in an electrostatic field without any redox reactions. When applied a voltage between the electrodes, the capacitor is charged leading to negative and positive charges to move towards the surface of the electrodes under opposite polarization. If a capacitor is connected to a

circuit and charged, it generates a potential difference for a while. Capacitance (*C*) of a capacitor is defined as the ratio of electric charge (*Q*) found in each electrode to the potential difference (*V*) between them so that:

$$C = \frac{Q}{V} \quad (1.1)$$

,where if *Q* is in the unit of coulombs (C) and *V* is in the unit of volts (V), *C* is in the unit of farads (F) [2].

The easiest way to understand mechanism of charge storage in supercapacitors is to consult the electrical double-layer concept. Charge separation is observed on polarization at the electrode–electrolyte interface, leading to the double-layer capacitance, C, which is defined by Helmholtz in 1853:

$$C = \frac{\varepsilon_r \varepsilon_0 A}{d} \quad (1.2)$$

,where ε_r stands for dielectric constant of the electrolyte, ε_0 represents the dielectric constant of the vacuum, *A* stands for the surface area of the electrode and *d* represents the effective double-layer thickness or in other words, charge separation distance [4].

The main challenge in supercapacitors is to improve the amount of energy stored since they show low energy density. In order to determine the energy stored in supercapacitors equation below is used:

$$E = \left(\frac{1}{2}\right)\frac{CV^2}{3600} \quad (1.3)$$

,where *E* is the energy (watt-hours), *C* represents the capacitance (farads) and *V* stands for the cell voltage (volts) [6].

As well-known power (*P*) is the magnitude of energy per unit time. In calculating *P* for a standard capacitor, the resistance due to the internal parts of the capacitor such as current collectors, electrode materials, electrolytes and separators should be considered. The resistance of the aforementioned parts is generally determined in aggregate and collectively denoted as the equivalent series resistance

(ESR) (Ω). The ESR, which can be recognized by a voltage (*V*) drop, affects the maximum capacitor voltage in discharge and thus restricts the maximum power and energy of a capacitor. The calculation of capacitor power is usually determined at matched impedance meaning that the load resistance is assumed to be the same as the ESR of the capacitor. Therefore, the maximum power P_{max} is a function of ESR and it is given by:

$$P_{max} = \frac{V^2}{4ESR} \quad (1.4)$$

However, although the resistance of an efficient capacitor is usually much lower compared to the connected load, the actual generated peak power, is usually lower than P_{max} though it is still considered relatively high [2].

1.1.1.3 Differences Between Supercapacitors and Batteries

Properties of batteries and supercapacitors are described by electrochemical concepts, although different electrochemical mechanisms are dominant on their related energy and power densities. In the recent years, a significant expansion is observed in the energy storage area aiming research on materials that can combine the high energy density of batteries with the fast charging and long cyclic life of supercapacitors. However, the differences between these two electrochemical devices can lead to confusion and unfounded claims when basic performance criteria are not taken into account [7].

The different electrochemical concepts taking place in batteries and supercapacitors allow them to have separate charge storage characteristics. In batteries insertion of electrolyte ions causing redox reactions in bulk electrode materials is controlled by diffusion and therefore may be slow. In supercapacitors, there are two different mechanisms for charge storage that are electrical double-layer capacitance and pseudocapacitance. In the first one, briefly charges are stored by adsorption of electrolyte ions onto the electrode surface. There is no need for redox

reactions, thus in the absence of diffusion limitations the behavior to changes in potential is very fast and this provides a high power. Nevertheless, the charge is attached to the surfaces, hence the energy density of the supercapacitors in this storage mechanism is less than that of the batteries [8].

Different behaviors of supercapacitors from batteries can be diagnosed by using both galvanostatic and potentiostatic techniques as exemplified in Figure 1.2. Classic rectangular cyclic voltammograms as seen in Figure 1.2 (a) and linear time-dependent difference in potential at constant current shown in Figure 1.2 (b) are two main characteristics for electrical double-layer capacitance. As given in Figure 1.2 (c), in batteries cyclic voltammograms are recognized by faradic redox peaks, generally with quite large potential separation (larger than 0.1 to 0.2 V) between reduction and oxidation due to the phase transitions [9]. In galvanostatic experiments the presence of the phase transitions can be determined by the voltage plateau as demonstrated in Figure 1.2 (d).

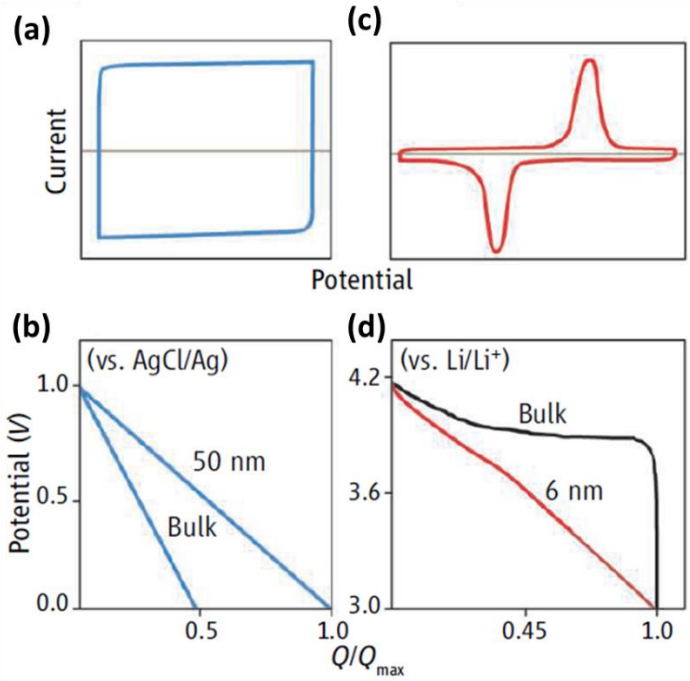

Figure 1.2. (a) Cyclic voltammogram and (b) galvanostatic discharge behavior of a typical supercapacitor. (c) Cyclic voltammogram and (d) galvanostatic discharge behavior of a typical battery [7].

In the 1970s, Conway et al. [1] discovered that reversible redox reactions occurring at or close to the surface of an appropriate electrode material result in electrochemical properties similar to electrical double-layer capacitors. But, these redox processes cause larger charge storage compared to double-layer [10]. This pseudocapacitance is defined as a second storage mechanism for capacitive energy. Pseudocapacitive materials have a great potential to combine battery-like energy density and cyclic life and power density of electrical double-layer capacitors.

Another difference between supercapacitors and batteries is their behavior when nanomaterials are employed. If a nanoscale material is used to fabricate a battery, the short transport paths of electrons and ions improve the battery's power density [11]. Nevertheless, this improvement is not an indication that a battery has converted directly to a pseudocapacitor as its galvanostatic profiles and faradaic redox peaks remain battery-like. At smaller scales (<10 nm) it is possible that traditional battery materials exhibit capacitor-like behaviors (Figure 1.2 (d)) [12]. On the contrary, galvanostatic discharge behavior of a true pseudocapacitor is linear for both nanoscale and bulk forms as seen in Figure 1.2 (c) [13].

1.1.2 Types of Supercapacitors

There are three main groups of supercapacitors as presented in Figure 1.3. One of them is the electrical double-layer capacitors (EDLCs), in which there is no redox reactions on the electrode in charging and discharging processes, and pure physical charge storage is observed at the electrode/electrolyte interface. Generally carbonaceous materials are used for this kind of supercapacitors. The other type is the pseudocapacitors, in which the electrode materials (e.g. conducting polymers) are redox active and charges are stored in this way [14]. Lastly, if a supercapacitor includes both of the aforementioned materials at the same time, it is named a hybrid supercapacitor. This type of supercapacitors have higher power density and better rate capability than the others. They are safer compared to batteries and need less maintenance. Also their cycle life is longer than their counterparts [15].

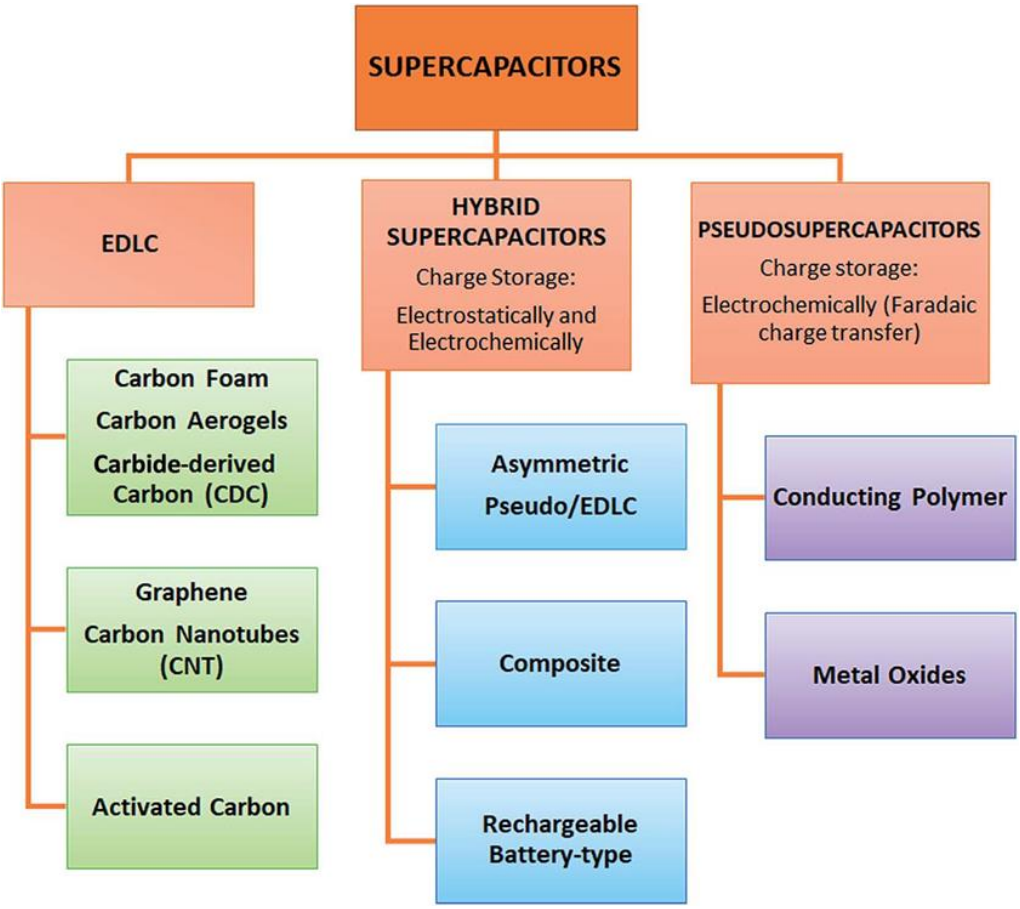

Figure 1.3. Classification of the supercapacitors [15].

1.1.2.1 Electrical Double-Layer Capacitors

EDLCs store energy electrostatically via reversible adsorption of ions of electrolyte onto high surface area and electrochemically stable carbon materials [6]. The concept of the double-layer which is the basis of EDLCs has been known to scientists since the 1800s when Helmholtz first proposed and modeled it in his study on colloidal suspensions. However, the practical utilization of double-layer capacitors for electrical energy storage became possible following the use of porous carbon electrodes and aqueous electrolytes in 1957. The fact that EDLCs actually store charge in the electrical double-layer with no redox reaction at the electrode-electrolyte interface was proved in 1966. The first commercial double-layer supercapacitors were made of carbon paste electrodes originated from an electrolyte

soaked porous carbon with an ion-permeable separator. Although license of these early devices was transferred to another company in 1971 due to the lack of sales, they were further improved and marketed especially for memory backup technologies. Today, a large number of high throughput EDLC devices are commercially available from a variety of manufacturers (Maxwell Technologies, Murata Manufacturing, Skeleton Technologies, etc.) and suppliers worldwide for an increasing number of applications [2].

As given in Figure 1.4, EDLC fabrication is similar to battery fabrication in which two electrodes are placed in an electrolyte. Between the electrodes, an ion-permeable separator is positioned to avoid short circuits in the devices. During charging, the cations and anions of the electrolyte migrate towards the negative and positive electrodes, respectively, forming two double-layers on each electrode–electrolyte interface. Since each interface contains a capacitor, it is possible to think of the complete device as two capacitors connected in series [2].

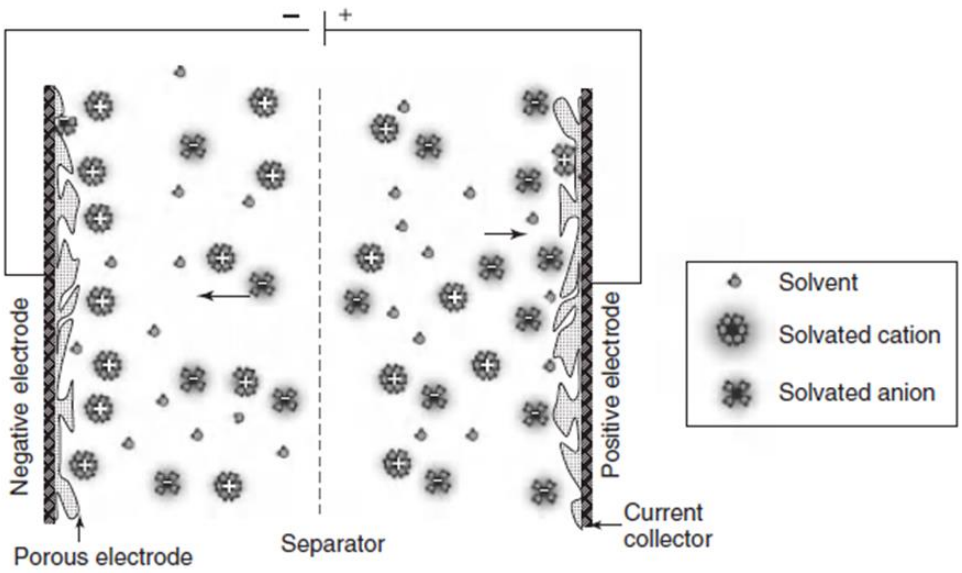

Figure 1.4. Schematic illustration of an EDLC in its charged state [2].

1.1.2.1.1 Models of Electrical Double-Layer

Charge separation is observed at the electrode–electrolyte interface with polarization, forming a double-layer capacitance as Helmholtz proposed in 1853. This capacitance model was then improved by Gouy, Chapman and Stern, who claimed the existence of a diffuse region in the electrolyte because of the ion population close to the surface of the electrode [4].

It is useful to briefly mention these models in the order that they were historically developed in the process. The phenomenon of double-layer is based on a model composed of two layers of opposite charges, facing each other and positioned within an atomically small distance. Hermann von Helmholtz used this model to explain his understanding of the distribution of negative and positive charges, quasi-2-dimensionally, first at the interface of colloidal particles. An illustration of this model with its compact structure is seen in Figure 1.5 (a). This was later named as Helmholtz double-layer model [1].

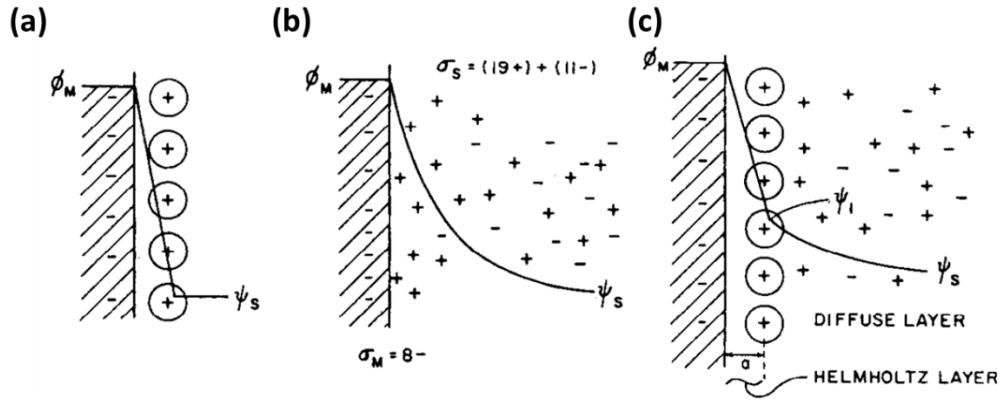

Figure 1.5. Double-layer models: (a) Helmholtz model, (b) Gouy point-charge model, and (c) Stern model which is a combination of Helmholtz and Gouy models [1].

After examination on Helmholtz's model, it was recognized that ions located in the solution part of the double-layer is not static in a restricted area as shown in Figure 1.5 (a). Instead, they are exposed to the thermal fluctuation effects with

respect to Boltzmann principle. Gouy described this thermal fluctuation in an alternative explanation of the double-layer. According to Gouy, the oppositely charged ions conjugate to the electrons found on the metal surface were considered as a 3-dimensional diffusely distributed population of anions and cations. These ions have a net charge opposite and equal to the virtually 2-dimensional electron deficit or excess charge on the surface of the metal. This description is known as Gouy point-charge model and is schematically illustrated in Figure 1.5 (b). This model was then mathematically refined by Chapman in 1913 by using combined application of Poisson's electrostatic equation and Boltzmann's energy distribution equation.

After the recognizing of overestimation problem of the double-layer capacitance in Gouy-Chapman model, the efforts were focused on this problem and finally Stern overcame it in 1924. As shown in Figure 1.5 (c), in Stern model there is an inner layer of the ion distribution compatible with an adsorption mechanism with respect to Langmuir's adsorption isotherm referred as Helmholtz layer. Beyond Helmholtz layer, into the solution, there is a region of distributed charged ions obeying Gouy-Chapman model named as diffuse layer. Aforementioned three models have been further improved by many researchers until today and became the base of the modern models [1].

1.1.2.1.2 Carbon Materials

In EDLCs, carbon and its wide variety of derivatives, are currently the most extensively investigated and used electrode materials thanks to their high conductivity and high surface area. Thus, many industry establishments specialized on carbon are now considering supercapacitors as an attractive market for their devices. Carbonaceous materials have long been utilized in the electrodes of energy storage systems as supports for active materials, conductive additives, intercalation components, current collectors and electron transfer agents [16]. Therefore, it is quite inherent to consider carbonaceous materials are also ideal materials for EDLC

electrodes. The interest in carbon as a supercapacitor electrode material stems from the mixture of chemical and physical properties of supercapacitors, such as:

- high surface area,
- high conductivity,
- controllable pore structure,
- good corrosion stability,
- high temperature stability,
- relatively low cost,
- and compatibility in nanocomposite materials [17].

The capacitance of carbonaceous materials is directly proportional to its available specific surface area. In order to measure the specific surface area of carbonaceous materials gas adsorption technique (generally nitrogen at 77 K) and following, Brunauer-Emmett-Teller (BET) theory are widely used. The areal capacitance values of some carbonaceous materials are provided in Table 1.1. It is obviously seen that the reported areal capacitances are strongly dependent on the morphology and change significantly with the type of the carbonaceous material.

Table 1.1 Typical areal capacitance values of some carbonaceous materials [17].

Material	*Electrolyte*	*Areal Capacitance ($\mu F/cm^2$)*	*Specific Surface Area (m^2/g)*
Activated carbon	10% NaCl	19	1200
Carbon black	1 M H_2SO_4	8	80-230
Graphite powder	10% NaCl	35	4
Carbon aerogel	4 M KOH	23	650
Carbon fiber cloth	0.51 M Et_4NBF_4 in PC	6.9	1630

Et_4NBF_4: Tetraethylammonium tetrafluoroborate, PC: Propylene carbonate.

A great number of studies are currently being conducted for the synthesis of carbonaceous materials with a controlled pore size distribution to obtain supercapacitor electrodes with high conductivity and specific capacitance. The integration of pseudocapacitive materials (for example, conducting polymers and metal oxides) into carbonaceous materials also attracts a growing interest in terms of enhancing the specific capacitances and widening the voltage window of the supercapacitors. The ultimate goal in this area is to increase the specific energy of carbon-based supercapacitor electrodes without compromising their high-level specific power [17].

1.1.2.2 Pseudocapacitive Supercapacitors

The performance of EDLCs depends on the electrostatic forces to which ions are exposed in the electrode/electrolyte interface. Carbonaceous materials are the most common active materials for EDLCs thanks to their high porosity and specific surface area compatible with the ion sizes. However, a carbon material has a constant surface capacitance more or less around 10 $\mu F/cm^2$ independent of its pore size, texture and origin. In other words, using only a pure carbonaceous material in supercapacitors provides limited gravimetric specific capacitance in the band of 100-200 F/g depending on the type of the electrolyte. However, in a supercapacitor device, if quick faradaic reactions exist in addition to electrostatic forces, measured capacitance values can increase significantly. Since the charge transferred within these faradaic reactions is proportional to potential, this concept is named as pseudocapacitance. In supercapacitor literature prominent materials that exhibit pseudocapacitance behavior are transition metal oxides, conducting polymers and functionalized carbons. Except for electrode materials, it was proved that pseudocapacitance can arise from redox reactions and/or chemisorption of electrolyte species [18].

In Figure 1.6, difference between the electrical double-layer and the pseudocapacitance is schematically illustrated. The double-layer seen in Figure 1.6

(a) is a result of adsorption of negative electrolyte ions on the positively charged surface of the electrode composed of carbon particles. Specific surface area of materials is directly proportional with the number the of the adsorption sites that the electrolyte ions can be attached. Porous carbon has higher specific surface area than carbon particles and thus it provides higher specific capacitance through storing higher number of charges. This is due to its intricate pore structure as shown in Figure 1.6 (b). But this two double-layer capacitance mechanism does not include redox reactions and therefore shows low specific capacitance. In Figure 1.6 (c) and (d) schematic illustrations of the mechanism of the pseudocapacitance giving higher specific capacitance values compared to double-layer capacitance are demonstrated. Redox pseudocapacitance is depicted in Figure 1.6 (c) with positively charged ions adhering to the surface or penetrating just under the surface of the electrode as observed in manganese dioxide (MnO_2) based pseudocapacitors [19]. In Figure 1.6 (d) intercalation pseudocapacitance is shown by exemplifying Li^+ ions inserted into the electrode material as observed in vanadium pentoxide (V_2O_5) based pseudocapacitors [20].

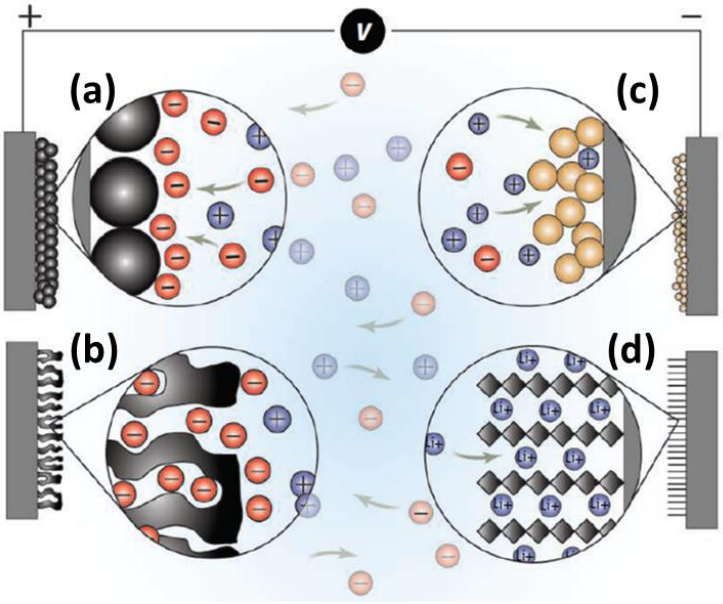

Figure 1.6. Schematic illustrations of capacitive energy storage mechanisms of (a) carbon particles, (b) porous carbon, (c) redox pseudocapacitance and (d) intercalation capacitance [7].

1.1.2.2.1 Differences of Pseudocapacitors from EDLCs and Batteries

As a concept of energy storage, pseudocapacitance is in a position between batteries and EDLCs which store charges completely in the double-layer on a material having high surface area. Pseudocapacitance is predominantly based on redox reactions triggered by the intercalation of charge compensating ions, such as Na^+ or Li^+. Cyclic voltammetry (CV) curves present valuable information for classification of the charge storage mode. Upon potential scanning, EDLCs generally exhibit a potential-independent capacitance and, thus potential-independent current as seen in Figure 1.7 (a). Conversely, batteries have evident and widely separated peaks, as seen in Figure 1.7 (g) and (h), arising from the oxidation and reduction of the electrode materials. In EDLC devices, constant current discharge causes a linear potential (*E*) versus time (*t*) graph as seen in Figure 1.7 (c), while in batteries, as demonstrated in Figure 1.7 (i), upon discharge a nonlinear *E* versus *t* profile is observed. This type of discharge profile is recognized through plateaus of almost constant potential associated with the potentials at which the Faradaic oxidation or reduction reactions take place. When properties which might be placed between these two extremes are observed, one can claim the presence of the pseudocapacitance. A pseudocapacitor usually shows the electrochemical characteristics of one, or a combination, of the following mechanism: surface redox mechanism (e.g., MnO_2 in neutral, aqueous electrolytes, Figure 1.7 (b)), intercalation-type mechanism (e.g., lithium insertion in niobium pentoxide (Nb_2O_5) in organic electrolytes, Figure 1.7 (d)), or intercalation-type mechanism having broad and electrochemically reversible redox peaks (e.g., titanium carbide (Ti_3C_2) in acidic, aqueous media, Figure 1.7 (e)) [21].

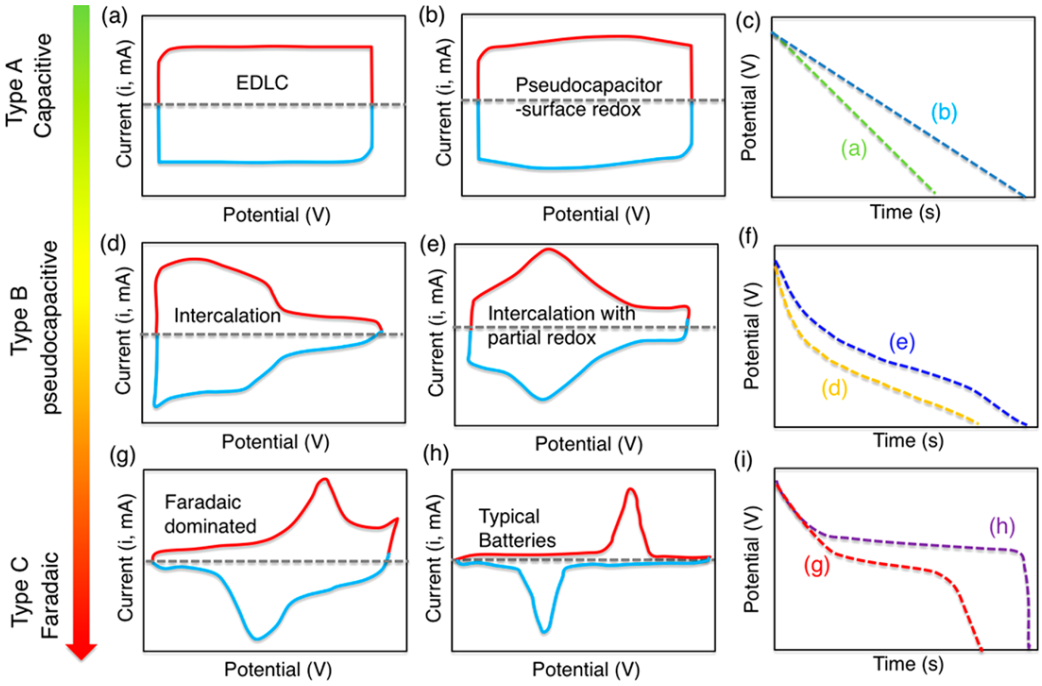

Figure 1.7. (a, b, d, e, g, h) CV and (c, f, i) related galvanostatic discharge curves for different types of energy storage materials [21].

1.1.2.2.2 Transition Metal Oxides

Metal oxides can be used as nanocomposite reinforcements to enhance mechanical and electrochemical properties of the supercapacitors [22]. Highly pseudocapacitive RuO_2 is the most commonly known metal oxide; but its widespread use in commercial products is limited [14]. This is because it has two major drawbacks, which are the high cost and toxicity. Hence, numerous research groups were focused on the development of alternative, cost-effective metal oxides such as molybdenum dioxide (MoO_2), MnO_2, cobalt oxide (Co_3O_4), nickel oxide (NiO) and V_2O_5 for pseudocapacitive electrodes [4,14,23,24].

RuO_2 shows quite high specific capacitance of up to 750 F/g [25]. As a conducting metal oxide, RuO_2 was quite popular electrode material in early supercapacitors used for military and space applications [26]. In addition to the high specific capacitance, low resistance leads to very high specific powers in RuO_2-based supercapacitors. It can be determined by a rough calculation that in a typical RuO_2-

based device, 90% of the cost is due to the electrode material. Moreover, RuO_2 exhibits better performance in aqueous electrolytes and this is a limiting factor for the nominal cell voltage [27].

In Table 1.2 properties of some metal oxides except for RuO_2 are provided. V_2O_5 has the highest specific capacitance but at the same time it shows poor cycle life. Its capacitance notably decreases only after a few hundred cycles. On the other hand, MnO_2 exhibits longer cycle life and high capacitance. It has also the potential to be a positive electrode material for asymmetric supercapacitors. These make MnO_2 the leading alternative to RuO_2 [28].

Table 1.2 Properties of some metal oxides [28].

Compound	*Crystal Structure*	*Voltage Window (V)*	*Specific Capacitance (F/g)*
MnO_2	Amorphous	0-1	150
Fe_3O_4	Magnetite	-0.7-0.2	75
V_2O_5	Amorphous	-0.2-1	170

1.1.2.2.3 Conducting Polymers

Conducting polymers (CPs) show pseudocapacitive properties and are desirable for high performance supercapacitor applications. Their conductivities are quite high in charged state and they are capable of fast charge-discharge. Various CPs have been intensively investigated as active supercapacitor electrode materials. The most commonly used CPs include polythiophene (PTh) [29], polypyrrole (PPy) [30], polyaniline (PANI) [31] and their derivatives [32]. Chemical structures of common CPs are provided in Figure 1.8.

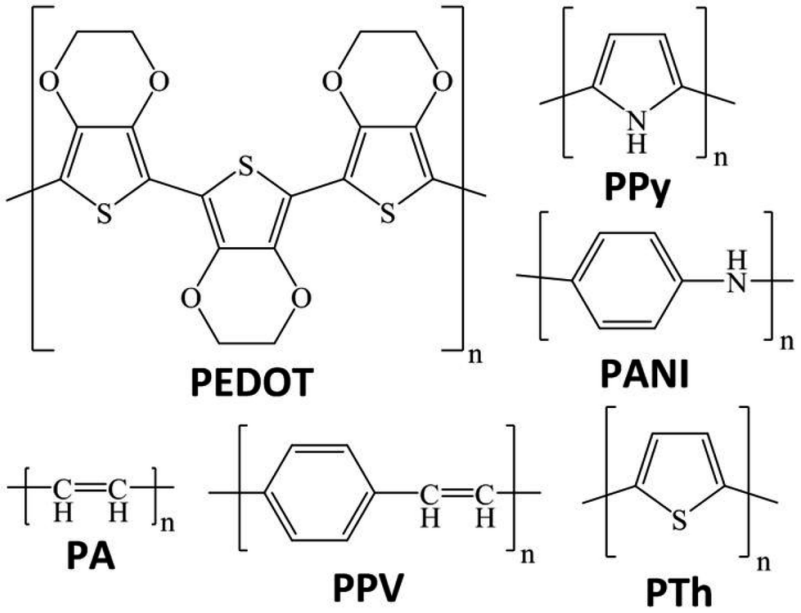

Figure 1.8. Chemical structures of some common CPs, such as poly(3,4-ethylenedioxythiophene) (PEDOT), polyacetylene (PA), poly(p-phenylenevinylene) (PPV), PTh, PPy and PANI [33].

The use of polymeric materials in supercapacitors has sparked a debate over whether such devices should still be classified as supercapacitors or better described as batteries. According to their CV behavior and voltage transient during charge and discharge, they can be assumed as batteries. However, it is easily understood that they are closer to supercapacitors compared to metal oxides. While the metal oxides show a series of redox reactions, the CPs typically exhibit only one redox peak. The most prominent disadvantage of CPs is the poor stability during cycling. Shrinking and swelling is observed upon charging and this might cause degradation in the electrodes [27]. Performance data of some common CPs used in supercapacitors are given in Table 1.3.

Table 1.3 Performance data of symmetric supercapacitor devices with some common CPs [2].

CP	*Electrolyte*	*VW (V)*	C_{sp} *(F/g)*	*E (Wh/kg)*	*P(W/kg)*	*Cycles*	C_{sp} *Fade*
PANI	Aqueous	0.5-1.2	120-1530	9.6-239	59-16000	1500	1-13%
PANI	Nonaqueous	1	100-670	70-185	250-7500	9000	9-60%
PPy	Aqueous	0.7-2	40-588	12-250	-	10000	9-40%
PPy	Nonaqueous	1-2.4	20-355	10-25	2-1000	10000	11-45%
PTh	Nonaqueous	3	1.6-6	-	-	5000	
PEDOT	Nonaqueous	0.8-2.7	121	1-4	35-2500	-	-

VW: Voltage window, C_{sp}: Specific capacitance, E: Energy density, P: Power density.

1.1.3 Favored Electrolytes for Supercapacitors

The electrolyte types that are utilized in supercapacitors can be divided into three main classes as aqueous, non-aqueous organic solvents, and ionic liquids (ILs). Some properties of these electrolytes are given in Table 1.4. Electrochemical voltage is a substantial parameter for both specific power and energy densities of supercapacitors since the ultimate working voltage is directly related to stability of the electrolyte. Aqueous electrolytes were the primary choice for early supercapacitors but in recent years there has been an increased demand for organic electrolytes and ILs. This is due to search for higher specific energy, which is a result of their wider electrochemical windows compared to the counterparts [2].

Table 1.4. Some properties of different electrolyte types [2].

Electrolyte	*Electrochemical Window (V)*	*Ionic conductivity*	*Viscosity*	*Cost*	*Toxicity*	*Assembly environment*
Aqueous	≤1	B	D	D	D	Air
Organic	2.5-2.7	D	B/C	B/C	B/C	Inert atmosphere
Ionic liquids	3-6	E	B	A	D	Inert atmosphere

A: Very high, B: High, C: Moderate, D: Low, E: Very low.

1.1.3.1 Aqueous Electrolytes

Aqueous electrolytes show one order of magnitude higher conductivity values (e.g. for 1 M H_2SO_4 at room temperature (RT), 0.8 S/cm^2), compared to that of IL and organic electrolytes. This property is useful for decreasing the ESR that is crucial for efficient power delivery of supercapacitors. The sizes of hydrated and bare ions, and accordingly their mobility values are influential not only on the ionic conductivity but also on the specific capacitance. The sizes and ionic conductivities of some ions are provided in Table 1.5. In addition to these values, electrochemical window and corrosion behavior should be considered in the selection of the electrolyte [34].

Essentially, aqueous electrolytes can be classified into three main groups as acidic, neutral and alkaline, (H_2SO_4, sodium sulfate (Na_2SO_4) and potassium hydroxide (KOH), respectively, are widely used examples of these three groups). The narrow electrochemical window arising from the decomposition of water is the most prominent drawback of aqueous electrolytes. Around 1.23 V, water decomposes and oxygen evolution reaction at the positive electrode takes place, which may cause deformation of the electrodes. This is a factor adversely affecting the performance and the safety of a device. In order to prevent this reaction,

supercapacitor devices containing aqueous electrolytes are generally operated up to a voltage of 1 V. In addition, working temperature range of supercapacitors containing aqueous electrolytes has to be between boiling and freezing points of water [34].

Table 1.5. The sizes of bare and hydrated forms, and ionic conductivities of some ions [34].

Ion	*Bare ion size (Å)*	*Hydrated ion size (Å)*	*Ionic conductivity (S cm^2/mol)*
H^+	1.15	2.8	350.1
Li^+	0.6	3.82	38.69
NH_4^+	1.48	3.31	73.5
Cl^-	1.81	3.32	76.31
OH^-	1.76	3	198
SO_4^{-2}	2.9	3.79	160

1.1.3.2 Organic Electrolytes

The utilization of organic electrolytes in supercapacitors basically results from higher operating voltages or in other words wider decomposition limits of such electrolyte solutions. This is a significant advantage over aqueous electrolytes because the amount of energy increases with the square of voltage (Equation 1.3). Decomposition limits of some common organic electrolytes are provided in Table 1.6 [1].

Numerous organic electrolyte-solvent systems are available and have been widely studied up to now. For example, tetraalkylammonium salts have come to the fore due to their relatively high conductivity and good solubility in organic solvents. Utilization of such salts significantly decrease the possibility of alkali-metal coating on a supercapacitor cathode in case of unexpected overcharge. Despite these advantages, such electrolytes must be quite pure and thus are very costly. In addition,

they should be dry, otherwise hydrogen and oxygen formation triggered by charging can be seen. Following this, recombination shuttle reactions causing self-discharge can also be observed. In addition to these, they may decompose upon intense overcharge, which typically begin from the negative electrode [1].

Table 1.6. Electrochemical window of some organic electrolyte solutions [1].

Solvent	*Electrolyte*	*Anodic limit (V)*	*Cathodic limit (V)*	*Working electrode*	*Reference*
AN	$LiClO_4$	2.6	-3.5	Pt	$Ag\text{-}AgClO_4$
PC	$LiClO_4$	2.3	-2.2	Pt	$Ag\text{-}Ag^+$
PN	Bu_4NPF_6	3.7	-3	Pt	Ag-AgCl

AN: Acetonitrile, PC: Propylene carbonate, PN: Propionitrile, Bu: n-butyl.

1.1.3.3 Ionic Liquids

Ionic liquids (ILs, also called as room temperature or low temperature molten salts) are described as salts consisting of only ions (anions and cations) and having melting points lower than 100 °C. As seen in Figure 1.9, ILs can be grouped as aprotic, protic and zwitterionic according to their composition [34]. The stability voltage window of ILs is solely affected by the electrochemical stability of the ions. If cations and anions are selected properly, it becomes possible to design high voltage supercapacitors. Currently, commercial products having 3 V voltage window and 1,000 F capacitance can be found in the market [35]. Nevertheless, at RT the ionic conductivity of ILs is quite low and thus they are generally used at higher temperatures. In the typical supercapacitor operation temperatures (-30 °C to +60 °C), ILs cannot fulfill the needs of the supercapacitor devices due to their insufficient ionic conductivity. Yet the presence of a great many combinations of cations and anions make it possible to obtain an IL electrolyte showing an ionic conductivity of 40 mS/cm at RT and a voltage window of >4 V [4].

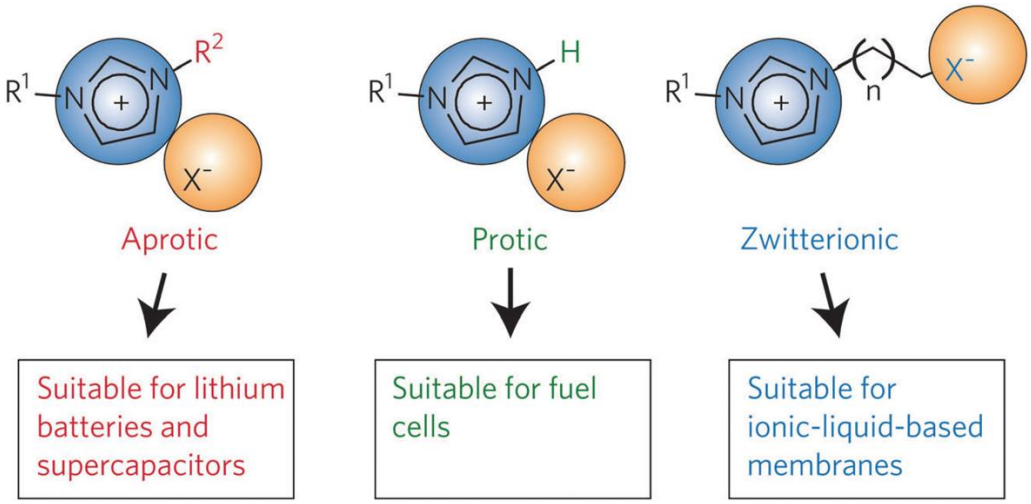

Figure 1.9. Schematics of aprotic, protic and zwitterionic types of ionic liquids [34].

1.1.4 Electrochemical Apparatus and Test Configurations

Electrochemical workstations generally consist of three main units: a computer, a signal waveform generator (SWG) and a potentiostat/galvanostat (PG). The computer sends different commands to the SWG/PG block and receives all measurement parameters from the users. SWG/PG block applies the necessary potentials or currents to the electrochemical cell and thus the electrochemical test starts. There are two groups of electrochemical techniques which are transient methods (chronoamperometry, chronopotentiometry, CV, etc.) and stationary techniques (electrochemical impedance spectroscopy (EIS), rotating disk electrode, etc.) [36].

The characterization of an electrochemical cell can be carried out by using both two-electrode and three-electrode measurements. Essentially, while the current passes through a counter electrode (CE) and a working electrode (WE), the voltage is controlled (or recorded) between a reference electrode (RE) and the WE. Since RE and the CE are shorted in a two-electrode configuration (Figure 1.10 (a)), the controlled (or recorded) voltage is the cell voltage. In a three-electrode cell (Figure

1.10 (b)), another electrode is placed between the WE and CE, serving as the RE. Here the important point is that RE selected for this configuration should have an ideal nonpolarizable behavior, in other words, voltage of RE should be constant at different current densities. Thus, the WE voltage can be determined or controlled properly [36].

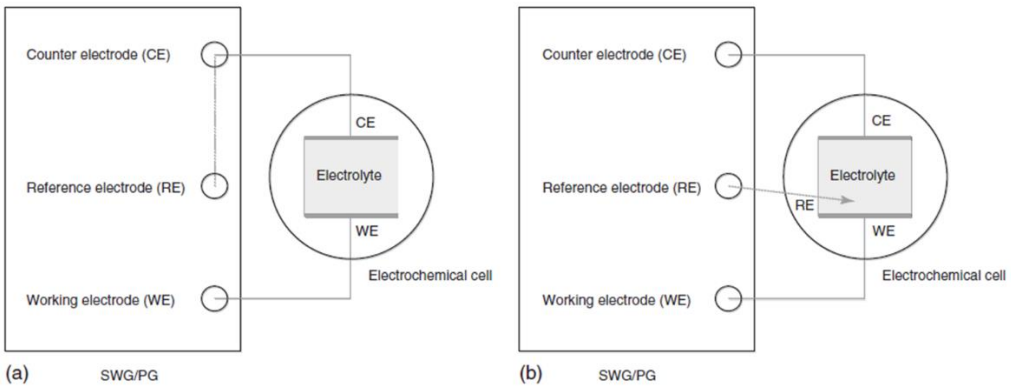

Figure 1.10. Schematic illustration of (a) two-electrode and (b) three-electrode electrochemical test configurations [36].

1.1.5 Frequently Used Electrochemical Techniques

1.1.5.1 Cyclic Voltammetry

Cyclic voltammetry (CV) is an extensively employed potential-dynamic electrochemical test. It is used to collect quantitative and qualitative data about solution and surface electrochemical reactions, such as electrochemical kinetics, reaction reversibility, reaction mechanisms, electrocatalytic processes, and influence of electrode properties on these parameters. The CV test is normally conducted in a three-electrode configuration or electrochemical cell consisting of a WE, CE, and RE but it can also be conducted in a two-electrode cell applying necessary procedure. The potential of the working or target electrode in a sample is tested against the reference electrode by back and forth linear scanning between the preset lower and upper potential limits during a CV measurement [28].

In a cyclic voltammogram, an ideal double-layer capacitance of a supercapacitor is recognized through a rectangular shape of the voltammetry curves as seen in Figure 1.11. Upon applying an opposite potential, the sign of the current is reversed immediately. In this kind of charge storage, current is independent of potential and purely electrostatic mechanism is valid. On the other hand, pseudocapacitive materials show deviation from such a rectangular shape and reversible redox peaks arising from pseudofaradaic processes are observed. In such materials, the effect of the electrode potential on the charge stored in the supercapacitor is quite dominant. Due to kinetically slow pseudocapacitive processes during charging, a potential delay is observed upon reversal of the applied potential [37].

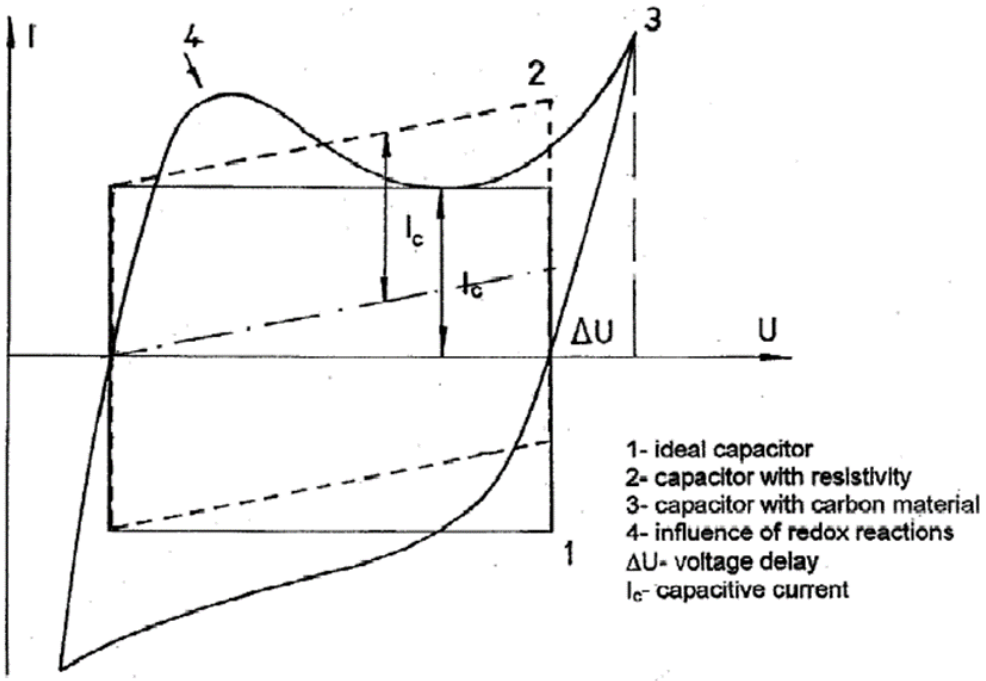

Figure 1.11. Typical cyclic voltammetry characteristics of a supercapacitor [37].

1.1.5.2 Galvanostatic Charge-Discharge

Galvanostatic charge-discharge (GCD) or chronopotentiometry is one the most commonly used techniques to evaluate ESR, cycle life, power and energy

densities of a supercapacitor. The conventional two-electrode or three-electrode cells can be used for GCD tests similar to CV measurements. However, in cycle life determination, two-electrode configuration is generally preferred since it can realistically simulate the practical operating conditions. In a standard GCD test, voltage change is monitored according to charge-discharge time under constant applied current. Unlike GCD, potentiostatic charge-discharge (chronoamperometry) in which cell current is measured with respect to charge-discharge time is rarely preferred for testing of supercapacitors [28].

The best way to calculate cell capacitance is to use GCD curves with the following equation:

$$C = \frac{I}{\frac{dV}{dt}} \quad (1.5)$$

,where C (F) stands for the capacitance, I (A) represents the discharge current and dV/dt (V/s) represents the slope of the GCD curve. For packaged products in supercapacitor industry, GCD is widely used to determine capacitance and it helps to find device limits in many applications. There is an IR ($V = IR$) drop on the upper part of the discharge curve arising from internal resistance and for typical EDLC materials the rest of the curve is linear. The curves of pseudocapacitive and hybrid electrodes can deviate from linearity with changing voltage and accordingly capacitance. For example, GCD curve of an asymmetric MnO_2/activated carbon supercapacitor is shown in Figure 1.12. When the maximum voltage of 2.2 V is reached, the GCD profile is no longer symmetrical demonstrating non-capacitive behavior [38].

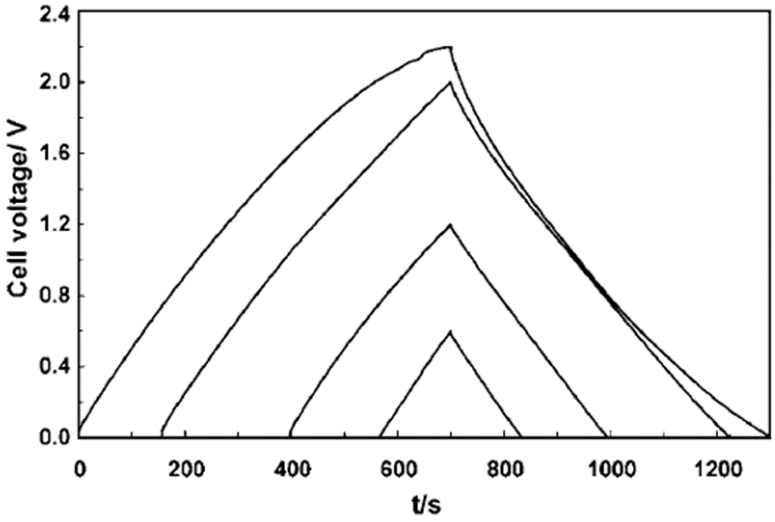

Figure 1.12. GCD curves of an asymmetric MnO_2/activated carbon supercapacitor measured within different voltage windows [38].

1.1.5.3 Electrochemical Impedance Spectroscopy

Electrochemical impedance spectroscopy (EIS) or alternating current (AC) impedance spectroscopy is a comprehensive test for the characterization of energy storage systems including supercapacitors. ESR, charge transfer resistance and ionic resistance can be determined using EIS. With this technique ex-situ measurements, which are useful for design and improvement of supercapacitors can be conducted. In addition, in-situ measurements which are generally used for the analysis of a single supercapacitor device under practical operating conditions are possible with EIS. Collected EIS data are usually demonstrated as Nyquist plots that provide information about the relationship between components of the resistance [28].

EIS is a very helpful measurement for the determination of capacitance since it can present complementary information such as frequency dependence. As an illustration, a Nyquist plot showing impedance spectrum (between 2 kHz and 8 mHz) of a supercapacitor device formed using 20 activated carbon electrodes is shown in Figure 1.13. At 100 mHz, there is a knee frequency, which separates two different behaviors of the supercapacitor. Below this knee frequency, the supercapacitor

behaves closely to an ideal capacitor since the resistance is affected weakly by the frequency. On the other hand, above this point the resistance is significantly affected by the changing frequency. In addition, the EIS data for this particular example also varies significantly with the number and the thickness of the electrodes [37].

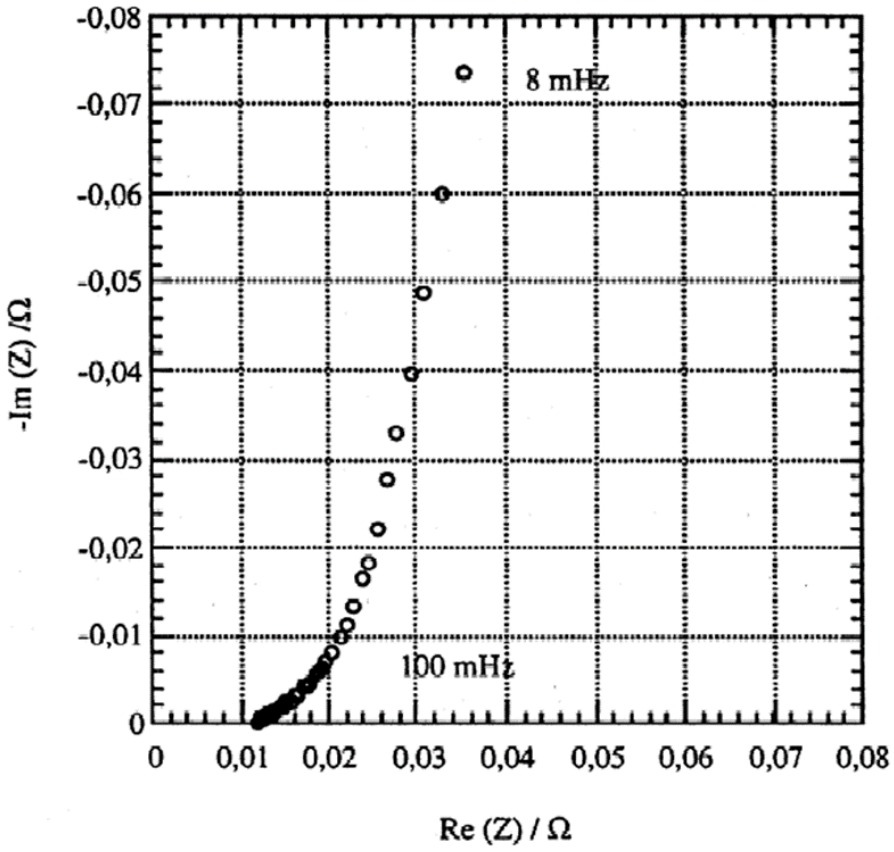

Figure 1.13. Nyquist plot of a supercapacitor device formed by 20 activated carbon electrodes [37].

1.1.5.4 Performance Metrics of Supercapacitors

In order to evaluate the performance of a supercapacitor device accurately, the use of a Ragone plot considering only gravimetric energy and power densities may not be enough. This is because the weights of the other device components are ignored in such an approach. Similar to Li-ion batteries, supercapacitors consist of electrolyte, separator, binder, current collectors, packaging parts and connectors

along with the electrodes. Carbonaceous materials, for example, occupy around 30% of the total weight of the finished commercial products. Thus, a coefficient of 3 to 4 is usually used to estimate more realistic power and energy densities of the systems. For instance, the energy density of a carbon-based electrode decreases to 5 Wh/kg from 20 Wh/kg [39].

This uncertainty stems from the preference of gravimetric energy and power densities over volumetric values. Most nanomaterials, such as graphene and carbon nanotubes, have a low packing density which results in empty space within the electrode. This space is filled with electrolyte, thus increasing the total mass of the device without increasing the capacitance. An extreme example of such materials would be carbon aerogels with 90% porosity. The volumetric energy density of such a material would be 20% of another electrode with only 50% porosity. Gravimetric and volumetric Ragone plots of the supercapacitors fabricated using same carbon material are provided, in Figure 1.14 (a) and (b), respectively. Here, one can easily see the performance drop of the materials in the transition from gravimetric to volumetric values. Moreover, it is understood that materials cannot carry their extremely high performance to medium- and large-scale systems if low-density and/or thin-film electrodes are preferred [39].

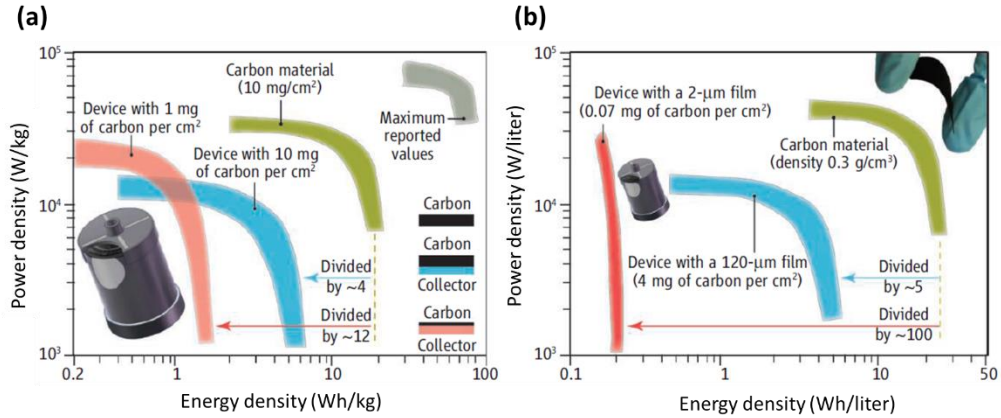

Figure 1.14. (a) Gravimetric and (b) volumetric Ragone plots of the supercapacitors fabricated using the same carbon material [39].

For microdevices and thin-film supercapacitors, the gravimetric energy density may be considered nonsense when compared with areal and volumetric values. This is because the weights of the active materials deposited in the form of a microscale-thin film on a nanotube layer or a chip attached to a smart fabric are negligible. These devices might have quite high discharge rates and gravimetric power densities; however, those properties cannot be scaled up linearly with the electrode thickness. In other words, the devices are not able to be scaled up to power an electric vehicle [39].

1.2 Nanomaterials for Energy Storage Applications

Nanomaterials enhance electronic conductivity and ionic transport to a great extent compared to conventional supercapacitor and battery materials. They provide high specific capacitance and rapid ion diffusion as they allow to occupy of all possible intercalation sites in the structure of the material. Thanks to these properties of nanomaterial-based devices, they can be operated at high currents. Thus they are preferred in energy storage applications that require high-power and high-energy. Nevertheless, there are still several problems about their utilization in energy storage applications. Except for carbon coatings on silicon particles and multiwall CNT additives in lithium-ion battery electrodes, the utilization of nanomaterials in commercial products is quite limited. After years of research, an extensive nanomaterials literature with various chemical compositions and morphologies emerged, including oxides, carbides, chalcogenides, carbon and elements found in lithium alloys. This literature contains different types of particles, such as zero-dimensional nanoparticles and quantum dots; one-dimensional nanowires, nanotubes, and nanobelts; two-dimensional (2D) nanosheets and nanoflakes; and three-dimensional (3D) porous nanonetworks. These chemically diverse nanoscale building blocks combined with lithium ions and beyond lithium ions are capable of proposing new approaches for energy storage, which are not possible with

conventional materials. Figure 1.15 illustrates some manufacturing techniques and energy storage applications of different types of nanomaterials [40].

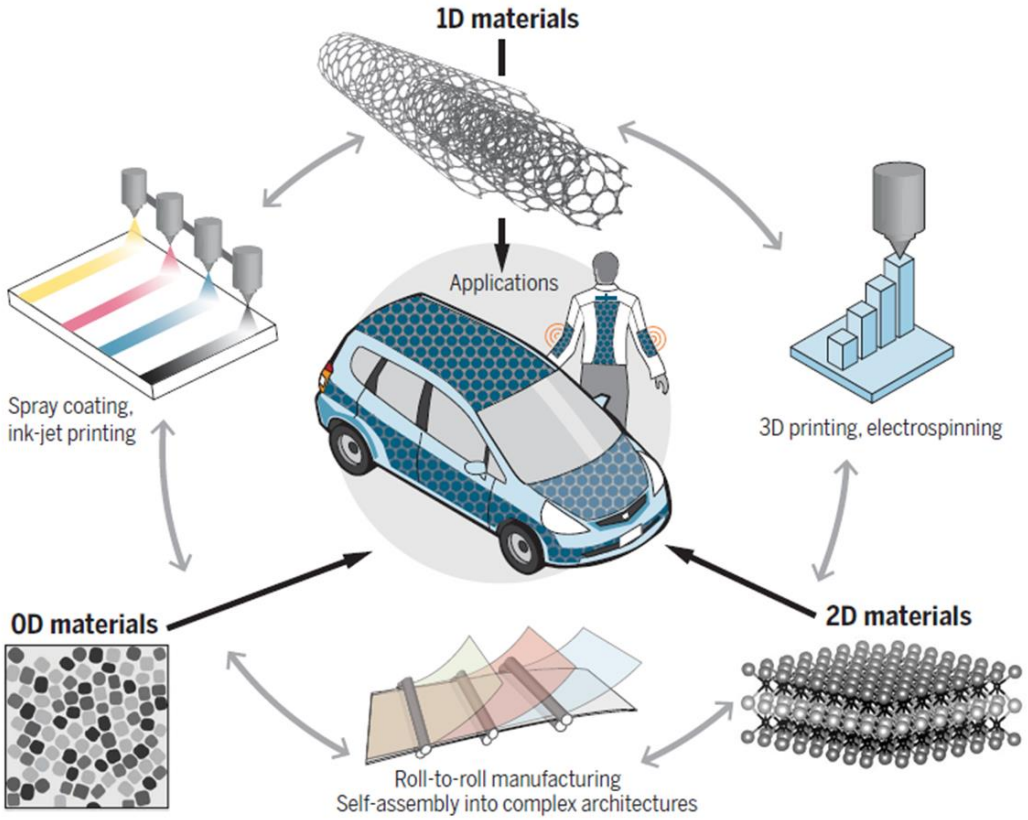

Figure 1.15. Examples of manufacturing techniques and energy storage applications of nanomaterials [40].

In summary, nanomaterials are advantageous for the energy storage applications because of the following reasons:

1. Short diffusion distances in nanomaterials provide faster charging for the devices and obtaining high current in a short time, i.e., increasing the power.
2. Large expansion due to microparticles causing short cycle lives and failures can be avoided using nanomaterials.
3. Nanomaterials improve the transport of multivalent ions, which is slow in bulk materials [41].

1.2.1 Nanocomposite Materials for Supercapacitors

Composites, which are one of the most prominent materials of today's technology, are composed of at least two components comprising a continuous matrix phase and a discontinuous support material to take the advantage of the best properties from each component. Composites are usually divided into three main groups named as macrocomposites, microcomposites, and nanocomposites with respect to the dimensions of the support in the structures. Nanocomposites leading to remarkable properties can be fabricated by the use of support materials below 100 nm in size. Due to their superior properties, nanocomposites have been widely utilized in various applications such as electronics and energy storage in recent years (Figure 1.16) [42].

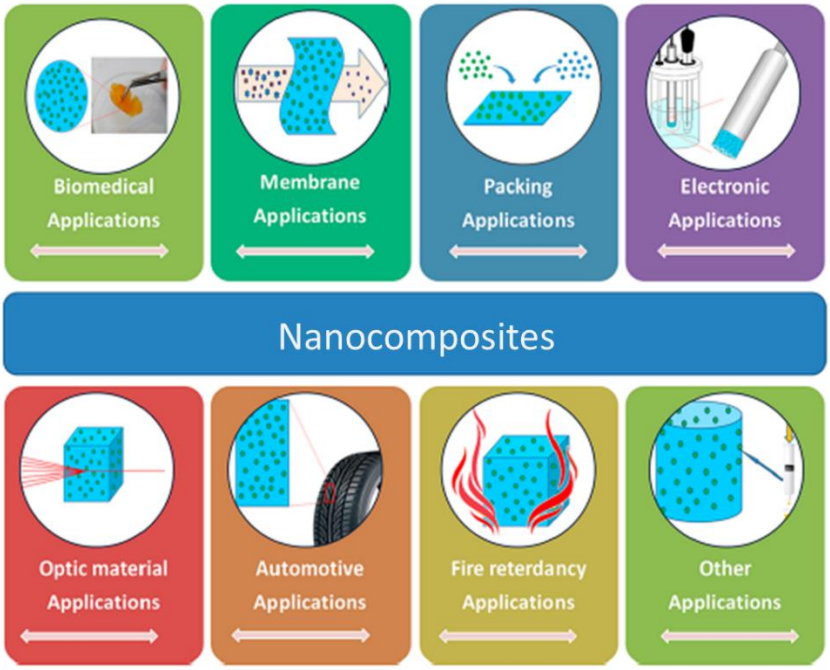

Figure 1.16. Application examples of nanocomposite materials [42].

Combining the unique superiorities of different nanoscale materials for the fabrication of nanocomposite supercapacitors needs special attention. This is because the obtainment of high-performance supercapacitors is possible through controlling, improving and optimizing the properties and structures of the electrode

materials. Substantially the individual components determine the properties of nanocomposite electrodes but the contribution of the morphology and interfacial characteristics cannot be ignored. In the recent years, notable studies have been conducted to improve all types of nanocomposite supercapacitor materials, such as mixed metal oxides, graphene mixed with metal oxides, conducting polymers mixed with metal oxides, and carbon nanotubes mixed with conducting polymers. In supercapacitor applications, parameters such as material selection, synthesis techniques, surface area, nanocrystallite size, and electrical conductivity should be taken into account for fabrication and design of electroactive nanocomposite materials. Although the field of nanocomposite supercapacitor electrodes has witnessed challenging extraordinary developments, many challenges still remain to be overcome [43].

1.3 Dissertation Objectives

Supercapacitors are the most promising energy storage devices to replace batteries. The behaviors of individual materials in the supercapacitor applications have been studied for many years and the level of the knowledge in this area is quite high. As in other fields of the materials science, nanocomposites find wide application areas in the supercapacitor world as well. There are numerous studies to develop nanocomposite supercapacitor electrodes in the literature, but there are still missing parts and fundamental and practical questions to be answered.

This dissertation focuses on the following questions to find enlightening and guiding answers:

1. To what extent it is possible to develop nanocomposite supercapacitors without compromising the superior properties of the individual materials?
2. What are the contributions of nanocomposites to low energy density, which is the biggest problem for supercapacitors to approach batteries?

3. What can nanocomposites bring in supercapacitors within today's hot topics such as long cycle life, flexibility, and environmentally friendly devices?

In the light of these questions, the next six chapters aim to achieve the following objectives:

Chapter 2: to find the effects of deposition of polyaniline on vertically aligned carbon nanotubes,

Chapter 3: to examine the accordance of expanded graphite-polypyrrole couple in a nanocomposite electrode,

Chapter 4: to investigate the contribution of carbon nanoflakes to manganese dioxide as an active material in an electrode,

Chapter 5: to reveal the positive aspects of combination of reduced graphene oxide aerogel and molybdenum disulfide in a nanocomposite electrode,

Chapter 6: to determine the advantages of hexagonal boron nitride-molybdenum disulfide nanocomposite electrode over bare molybdenum disulfide electrode,

Chapter 7: to observe the performance of a hexagonal boron nitride-polyvinyl alcohol nanocomposite separator in a symmetric titanium carbide supercapacitor.

CHAPTER 2

VERTICALLY ALIGNED CARBON NANOTUBE – POLYANILINE NANOCOMPOSITE SUPERCAPACITOR ELECTRODES

2.1 Introduction

Recently, supercapacitors are started to be considered to complement the fuel cells to improve their power density. The fuel cell vehicle is accepted as the vehicle of the future in response to environmental, economic and political considerations. Most recent technology on fuel cell vehicles includes hybrid fuel cells [44]. The next generation of hybrid vehicles and all-electrical automobiles based on fuel cells that consume alcohol or hydrogen as the clean energy sources need supercapacitors for high fuel efficiency [45]. The fuel cell largely compensates power demand, while a small battery can be used to meet peak power requirements. Similar benefits can be observed through hybridization of fuel cells with supercapacitors [46]. Disadvantages of designing a system with a single fuel cell are the slow dynamic response and long start-up time. On the other hand, a supercapacitor is a useful energy storage system to combine with the fuel cell to design a hybrid system capable of providing both the peak and steady-state power demand [47]. Supercapacitors have some advantages compared to batteries in hybrid fuel cell applications. They can be charged/discharged at high rates and have very low ESR. One of the most visible advantages of supercapacitors is the simplicity of connection to the fuel cell system. Different from a battery device, a supercapacitor can be directly combined with the fuel cell without costly components [46]. In order to determine the accuracy of the supercapacitors, Shin et al. [46] designed a supercapacitor/proton-exchange membrane fuel cell hybrid device. The device consumed 6.8% less fuel with respect to a standard fuel cell on average, and 17.5% at best, with a 50% improvement in peak power capacity. Harfman-Todorovic et al. [47] explained the fuel consumption

decrease as a function of the ripple current frequency in a fuel cell-supercapacitor hybrid. This is because the high frequency ripple current does not present a large output voltage change in the hybrid system, which directly means lower demand on hydrogen flow. As an alternative application field for fuel cells and supercapacitors Unda et al. [48] investigated the limits and potential of a novel hydrogen storage mechanism. This mechanism involved electrochemical division of protons and electrons on a polymer electrolyte membrane of a fuel cell-like electrode and following their storage in the electrical double-layer on a supercapacitor-like electrode. The highest storage capacities of hydrogen were determined as 0.17 and 0.13 wt.% in charging and discharging, respectively. Although the H_2 storage capacities were low, the combustion energy of the stored hydrogen within the cell was still 2.6 times higher compared to the stored electrical charge in a symmetric supercapacitor of similar quality. A capacitance of 11 mF/cm^2, which is comparable to that of a commercial EDLC was obtained with H_2SO_4 electrolyte.

Carbon can be found in a variety of crystal structures because of the various bonding configurations resulting from hybridization [49]. Conductivity and stability of almost all carbonaceous materials are very high. Moreover, they have controllable pore size and pore size distribution, which are important for supercapacitor applications [17]. Carbonaceous materials have already been utilized or have potential to be utilized as supercapacitor electrodes in the form of activated carbons, carbon nanotubes (CNTs), graphene, carbon fibers, and carbon aerogels [50–54]. Among these, CNTs have low electrical resistivity due their nanoscale tubular morphology [55]. They can be visualized as graphene sheets rolled in the form of a tube along their long axes [56]. Mobility of the charges in the CNTs is quite high through porous structure and central channels of the tubes. However, entangled CNTs exhibit slower electron and ion transfer because of their complex structure, which obstructs the diffusion of the ions to each CNT. On the contrary, vertically aligned carbon nanotube (VACNT) based electrodes present higher conductivity across the CNT length and their specific surface area is larger than that of entangled CNTs [57].

In electrochemical devices, deposition of CNTs on metallic foils, especially on aluminum foils is very common. Huang et al. [58] used household aluminum foil as the substrate for the formation of VACNT and polyaniline deposition. In a very similar study, Doğru et al. [59] fabricated flexible supercapacitor electrodes with VACNTs synthesized on aluminum foils. Despite the fact that the melting point of aluminum is quite low compared to most of the other substrate materials, direct deposition of CNTs on aluminum substrates can be carried out via controlled chemical vapor deposition (CVD) conditions. Availability, low cost and flexibility of aluminum foils make them very attractive as current collectors for supercapacitor electrodes. Thus, supercapacitor electrodes with VACNT decorated aluminum foils were investigated and found to exhibit significant cyclic stability and low resistance [60]. In fact, the use of CNTs synthesized on aluminum foils is not only limited to supercapacitors but also demonstrated for battery electrodes [61].

CNT growth by CVD method includes self-assembly of carbon atoms near the catalytic metal nanoparticles. In other words, metal nanoparticles can be thought as templates, where carbon compounds decompose and CNT growth starts [62]. While the CNT growth progresses, metal nanoparticles saturate the dangling bonds of CNTs at the edges and stabilize them [63]. As a catalyst, transition metals such as nickel, iron, and cobalt are used for CNT growth on a substrate. Methods used for the deposition of metal catalyst onto substrates involve either solution-based or vacuum based deposition routes [64]. Solution-based methods are cost-effective yet more complicated since the thickness of the metal thin film cannot be monitored simultaneously. In contrast to this, vacuum based deposition techniques are more controllable. On the other hand, if the surface energy of the substrate is high, catalyst diffusion towards inner sections of the substrate can be seen. In order to overcome this problem, diffusion barrier layers having low surface energies can be coated between the substrate and catalyst [62]. At elevated temperatures, catalyst diffusion in aluminum substrates can also be valid; but, at the same time aluminum has its natural oxide on its surface. This oxide layer protects aluminum substrate from catalyst diffusion [65].

Up to now CNT-PANI composite materials has been utilized in electrodes for both microbial fuel cells and supercapacitors [66,67]. Very recently De et al. [68] investigated combinatorial approach for the production of a hybrid structure composed of Pt nanoparticles decorated CNT-PANI composites (CNT-PANI/Pt) for the energy efficient fuel cells. It has been observed that the CNT-PANI/Pt composites are very strong against rapid poisoning and triggers the electron movement during the electrochemical reaction. Variety of materials were used as substrates for the formation of CNT/PANI nanocomposites. Hui et al. [69] produced PANI nanowire arrays aligned on CNT networks synthesized on the surface of glassy carbon electrodes for sensor applications. Zhang et al. [70] prepared PANI/CNT array composite electrode on a tantalum foil. Faraji [71] produced PANI/CNT nanocomposite on titanium oxide (TiO_2) nanotubes/Ti electrodes. Zhang et al. [72] fabricated multi-walled CNT/PANI composite films on a stainless-steel sheet. Besides these substrates, aluminum can be also used for the fabrication of CNT/PANI nanocomposites, because of its abundance and relatively low cost compared to the substrates mentioned above. The use of aluminum foils and CNTs for energy storage devices with organic electrolytes are quite common in the literature [58,60,61]. However, it is known that aqueous electrolytes are cost effective and can be simply prepared. On the contrary, organic electrolytes usually need complex purification processes and should be processed under a protective atmosphere to avoid oxidation. In addition, utilizing neutral aqueous electrolytes in supercapacitors presents an environmentally friendly way to improve the energy density [34]. In this study [73], VACNT/PANI nanocomposite supercapacitor electrodes were prepared and electrochemically tested using Na_2SO_4 electrolyte. VACNTs were synthesized on aluminum foils and PANI was coated on top of the VACNT layer. Since VACNTs and PANI have different charge storage mechanisms as EDLC and pseudocapacitive type respectively, their nanocomposite form becomes highly promising to investigate their synergistic effect in terms of electrochemical response.

2.2 Experimental

Pure aluminum foils were purchased from Alfa Aesar (thickness: 0.025 mm, 99.45% metal basis). First, foils were cleaned with acetone (99.8%), isopropanol (99.8%) and deionized water (18.3 MΩ) by simply immersing them into these solvents for 10 minutes each. Second, they were dried in a furnace at 80 °C. After the cleaning procedure, catalyst deposition was carried out on top of the foils using a physical vapor deposition (PVD) system.

Since aluminum can be oxidized easily and this oxide layer prevents the catalyst diffusion towards the substrate, firstly a 13.3 nm thick layer of aluminum was coated by PVD on the cleaned aluminum foils. These foils were kept under open atmosphere overnight to obtain fresh oxide layer. Following this, a 1.7 nm thick layer of Fe catalyst layer was deposited via PVD on top of the aluminum oxide layer. Finally, the foil was annealed in a furnace in open atmosphere at 500°C for 1 hour to oxidize the Fe catalyst.

Following the coating of catalyst, small pieces of the foils with an area of 2 cm^2 were loaded into the CVD system for CNT growth. For this purpose, Aixtron-Nanoinstruments Black Magic II PECVD system was utilized. Growth parameters such as pressure, gas flow rates, and temperature can be controlled easily within the system, which is very important for the reproducibility of the CNT synthesis.

CNT growth began with the evacuation of the chamber down to a base pressure of 0.1 mbar. After that the pressure was increased to 8 mbar and remained constant throughout the whole process. 200 sccm H_2 was sent to the chamber and then the stage temperature reached to 600 °C at a rate of 200 °C/min. At this point foils were annealed for 2 min. After the annealing procedure, carbon source gas, acetylene (C_2H_2), was sent into the chamber at a flow rate of 20 sccm and thus the CNT formation started. In this part of the process, temperature was increased to 620 °C with a rate of 25 °C/min. The synthesis proceeded for 5 minutes and then, H_2 and C_2H_2 flows were terminated and the chamber was cooled to RT using N_2 gas (1,000

sccm). Finally, the samples were taken out of the growth chamber following venting. All steps of CNT growth is summarized in Figure 2.1.

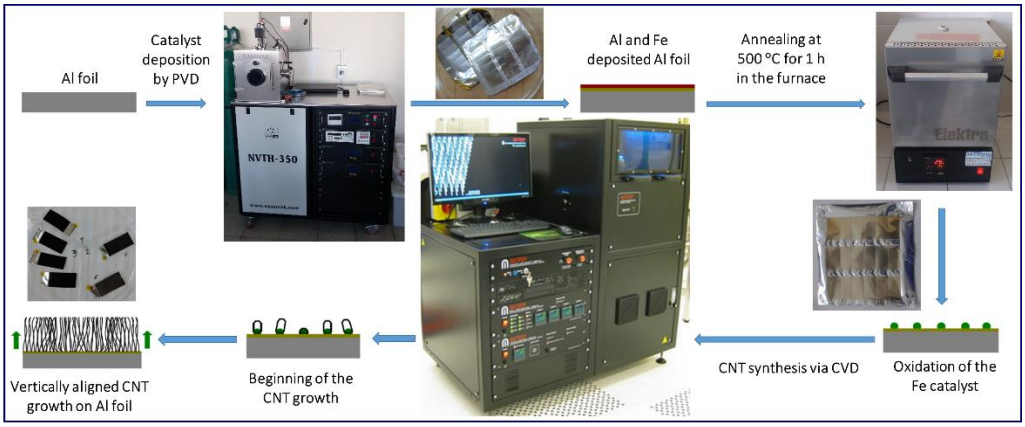

Figure 2.1. Steps of CNT growth.

PANI was electrodeposited onto VACNT grown aluminum foils via cyclic voltammetry at RT. The potential range was 0 - 0.9 V and the scan rate was 50 mV/s during the electrodeposition. Three different numbers of charge-discharge cycles were applied as 5 (5c), 10 (10c) and 15 (15c) cycles. Following the electrodeposition process, the samples were dried. The electrolyte used for the deposition of the samples consisted of 46.5 µl aniline monomer (Sigma-Aldrich, ≥99.5%) and 0.25 M H_2SO_4 (Sigma-Aldrich, 95-97%). A fresh electrolyte solution was prepared for each electrodeposition cycle. Both in the electrodeposition procedure and in the electrochemical tests the counter and the reference electrodes were Pt plate and silver/silver chloride (Ag/AgCl), respectively.

The morphological analysis of the prepared nanocomposite electrodes was conducted by scanning electron microscopy (SEM, FEI Nova Nano SEM 430, used at 10 kV). SEM samples did not necessitate deposition of an extra conductive layer. Dispersive Raman spectroscopy examination was conducted using Renishaw inVia system (excitation wavelength: 532 nm) with the purpose of structural characterization of the VACNTs. X-ray photoelectron spectroscopy (XPS) examination was conducted to diagnose the chemical state of the constituent elements. A PHI 5000 VersaProbe system was utilized for XPS analysis. The C (1s)

peak at 283 eV was used for the charge correction reference. A Perkin Elmer 400 system was utilized for Fourier transform infrared spectroscopy (FTIR) test. ATR mode was used during the FTIR measurements. For the electrochemical tests of the supercapacitor electrodes a three-electrode configuration was set and a Gamry Reference 3000 model potentiostat/galvanostat was employed. 1 M Na_2SO_4 was chosen as the electrolyte for the electrochemical tests. Electrochemical characterization of the electrodes was conducted through CV, GCD, and potentiostatic EIS.

2.3 Results and Discussion

The coating of PANI on top of the VACNT layer was practiced in a potential window of 0 and 0.9 V at a scan rate of 50 mV/s. A typical CV plot for the electrodeposition of 15c sample is provided in Figure 2.2. Humps within the CV curves resemble the polymeric oxidation reactions and dips resemble the reduction reactions of the aniline monomer. Moreover, the expanding curves of the voltammogram stands for the increasing thickness of the PANI layer with increasing number of cycles.

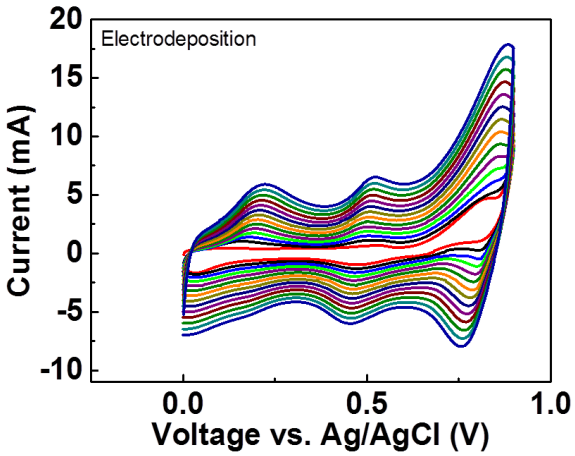

Figure 2.2. Cyclic voltammogram of the 15c electrodeposited sample.

Top-view and cross-sectional SEM images of the VACNTs formed on aluminum foils are shown in Figure 2.3 (a) and (b), respectively. As seen in the cross-sectional image, length of the VACNTs is 5 μm and there is a significant uniformity in terms of vertically alignment. Surface morphologies of the fabricated VACNT/PANI nanocomposite electrodes were also examined by SEM. Top-view SEM image of PANI deposited electrode and cross-sectional SEM images of 5, 10 and 15c PANI deposited electrodes are provided in Figure 2.4 (a) - (d), respectively. One can see from Figure 2.4 (a) that the fabricated VACNT/PANI sample has a non-uniform structure with voids. It is considered these voids enable ions of the electrolytes to reach the underlying VACNT layer easily and allow VACNTs to contribute the charge storage. Cross-sectional images in Figure 2.4 (b) - (d) reveal that the thickness of the PANI layer increases from approximately 1.5 to 3 μm with the increasing number of PANI electrodeposition cycles. Although the thickness increase is obvious in the SEM images, the average thickness of the PANI layers on the surfaces of the electrodes change. This variation in thickness was attributed to the non-uniform coating of PANI on the samples, as seen in Figure 2.4 (a).

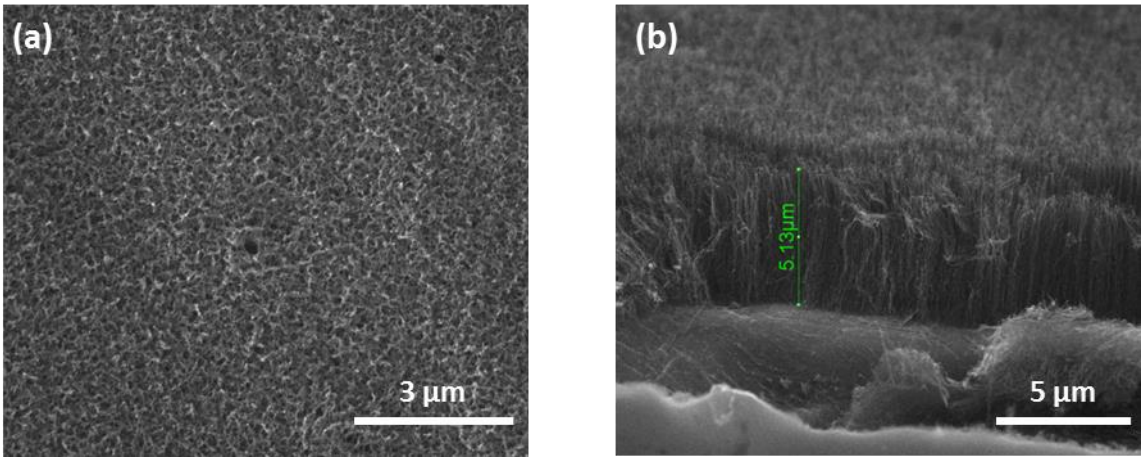

Figure 2.3. (a) Top-view and (b) cross-sectional SEM images of the VACNTs grown on aluminum foil.

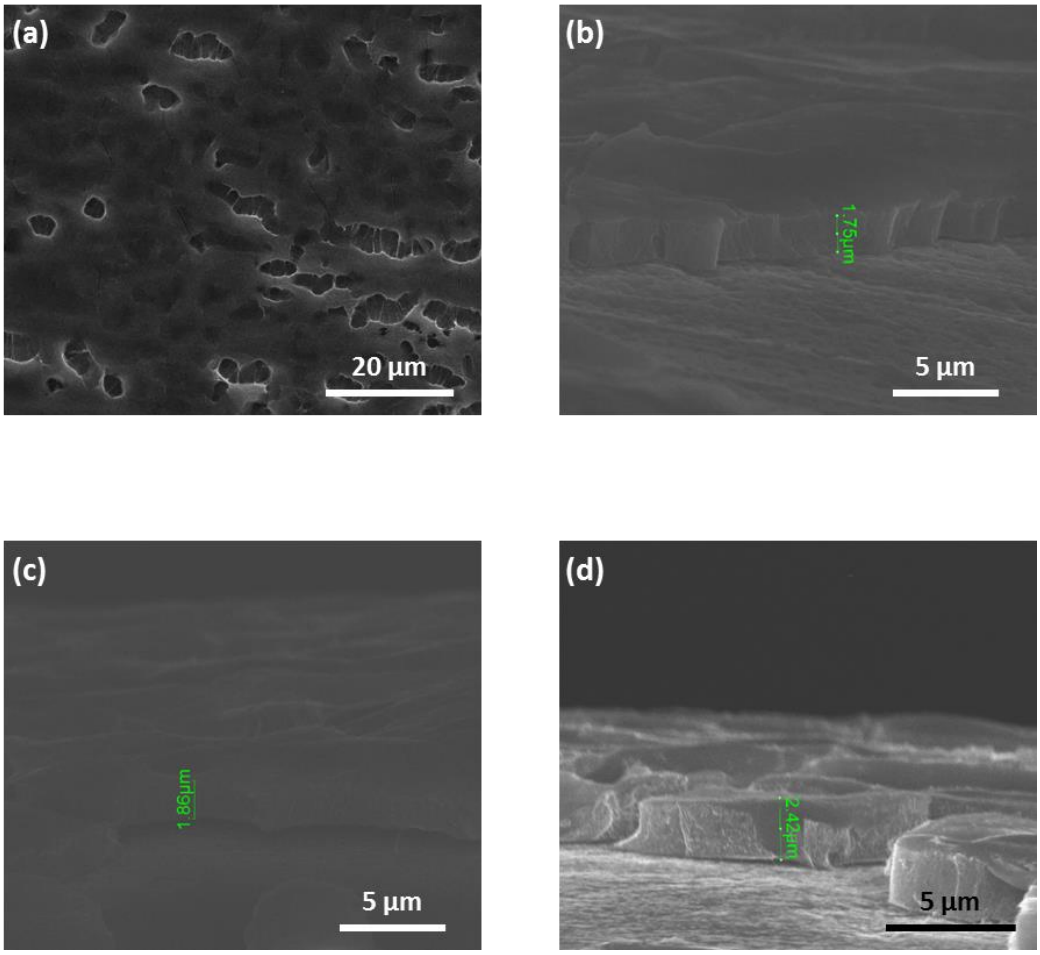

Figure 2.4. (a) Top-view SEM image of PANI deposited VACNT/PANI nanocomposite electrode and cross-sectional SEM images of (b) 5c, (c) 10c, and (d) 15c PANI deposited VACNT/PANI nanocomposite electrodes.

XPS measurements were conducted for elemental characterization and determination of the oxidation level of the catalyst layer on aluminum foils after annealing process. XPS survey spectrum is provided in Figure 2.5. Inset shows the spectrum for Fe. From the survey spectra, signals from Al, O and Fe were evident for catalyst deposited aluminum foils. It is clear that the annealing process did not contaminate the aluminum foil. Two peaks located at 711.2 and 724.7 eV are recognized in the Fe spectrum. These two peaks belong to iron(III) oxide (Fe_2O_3) compound [74] and the presence of these peaks clarify that the Fe layer transforms

into Fe_2O_3, upon annealing the Fe coated aluminum foil. This will be reduced back to Fe during heating under H_2 prior to CNT growth in CVD.

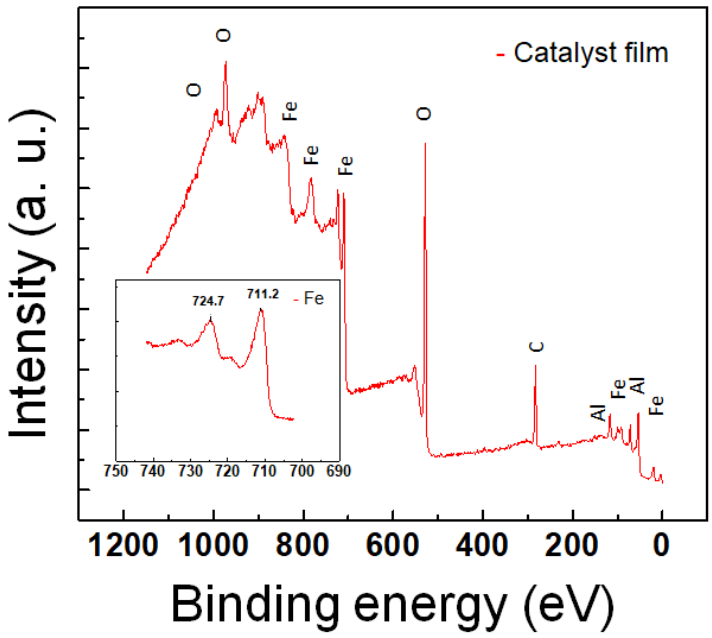

Figure 2.5. XPS survey spectra of the annealed Fe deposited aluminum foil. Inset shows the Fe spectrum.

VACNT/PANI nanocomposite electrodes were also characterized by FTIR to determine the chemical structure of the coatings. Figure 2.6 represents the FTIR spectra of the nanocomposite electrodes in the range of 500 – 2,000 cm^{-1}. The peaks in the spectrum found at 1542 cm^{-1} (C=C quinoid ring stretching vibration), 1498 cm^{-1} (C=C benzenoid ring stretching vibration), 1311 cm^{-1} (C-N stretching vibration), 1155 cm^{-1} (C-H plane bending vibration), 748 cm^{-1} (out of plane bending vibration), 876 cm^{-1} (para-distributed aromatic rings) and 1210 cm^{-1} (emeraldine form) are the characteristic peaks of the PANI [75]. The presence of these peaks is the proof of the success of the PANI deposition on the VACNT layer.

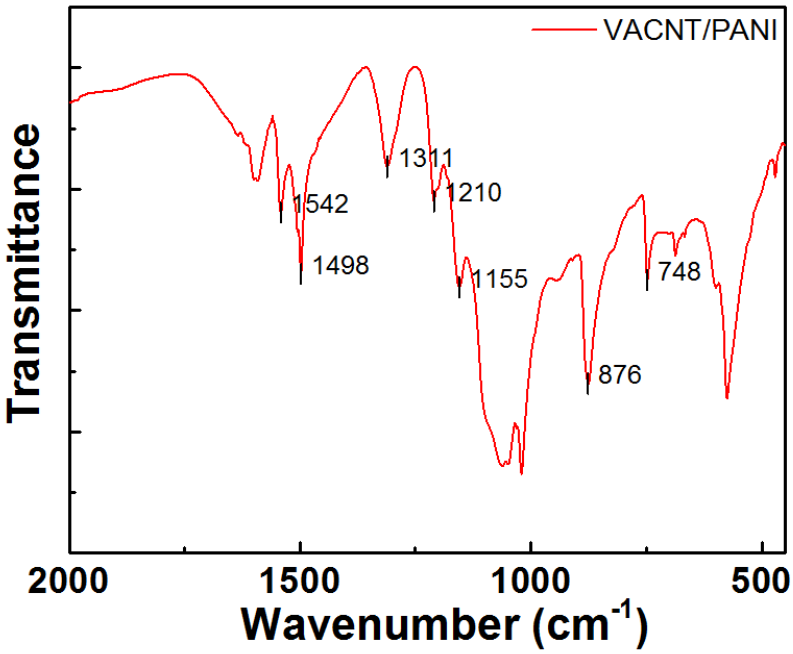

Figure 2.6. FTIR spectra of the VACNT/PANI nanocomposite electrode.

In order to determine the interaction between the PANI and VACNT layers, dispersive Raman analysis was carried out on both the VACNT/PANI nanocomposite and the pristine VACNT electrode, results of which are provided in Figure 2.7. Peaks positions seem to be similar for both samples apart from the newly appearing peaks for PANI. VACNT/PANI spectrum has peaks that belong to D band (1372 cm^{-1}) and G band (1602 cm^{-1}). While D band represents the amorphous disorder carbon structures, G band represents stretching vibration of C-C bond. Peaks observed at wavenumbers of 1190 cm^{-1} and 1512 cm^{-1} stand for C-H bending vibration of the benzenoid structure and C=N stretching vibration of the quinoid structure, respectively. Peak at 1351 cm^{-1} belongs to stretching vibration of C-N*+ delocalized polaronic structure and it is a property of protonated imine structure of PANI. Peak at 1617 cm^{-1} is ascribed to C-C stretching vibration of benzenoid structure [75].

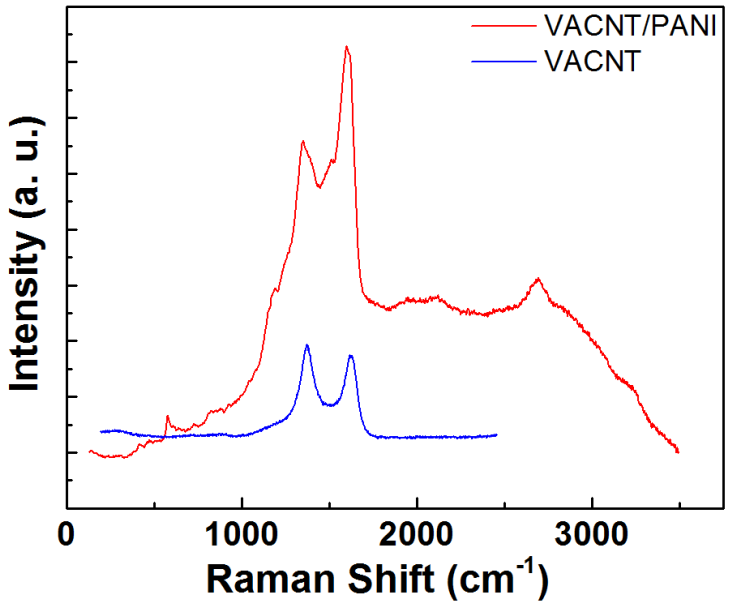

Figure 2.7. Raman spectra of the VACNT/PANI nanocomposite electrode in comparison to pristine VACNTs.

CV measurements of both pristine VACNT grown aluminum foil electrodes and VACNT/PANI nanocomposite electrodes were carried out in a potential window of 0 and 0.8 V. CV results of pristine VACNT coated aluminum foil electrode and 5c, 10c and 15c PANI coated nanocomposite electrodes at a scan rate of 100 mV/s are shown in Figure 2.8 (a). At first sight, the different shapes of the curves are noticed in Figure 2.8 (a). While the pristine VACNT electrode has a smooth curve, VACNT/PANI electrodes have curves with characteristic peaks. These peaks belong to oxidation and reduction reactions of PANI having a pseudocapacitive behavior. Thus, it is evident that fabricated nanocomposite electrodes show both EDLC and pseudocapacitive behavior, which would improve the overall performance of the electrodes. This improvement can also be recognized through the examination of the areas under pristine VACNT and 5c and 10c nanocomposite curves. The actual and notable capacitance improvement is observed for 15c nanocomposite electrode. The area under the CV curve of 15c electrode is notably larger than that of not only the pristine VACNT electrode; but also, 5c and 10c nanocomposite electrodes. The curve of 15c electrode covers approximately 6 times larger area than the other

nanocomposite electrodes. Further electrochemical characterization of 15c nanocomposite electrode can be seen in Figure 2.8 (b) at different scan rates. As expected, upon increasing the scan rate from 20 to 400 mV/s, the area under the rectangular-like curve increases as well and redox peaks start to be flatter on the curve. Further examination of Figure 2.8 (b) reveals the resistance effects are not pronounced for the 15c nanocomposite electrode, which would otherwise change the shape of the CV curve from horizontal to diagonal.

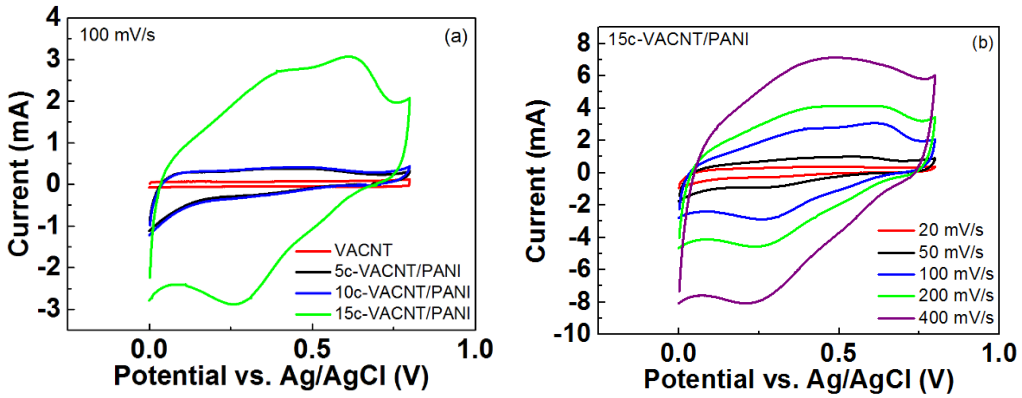

Figure 2.8. CV results of (a) pristine VACNT deposited aluminum foil electrode and 5c, 10c and 15c PANI deposited VACNT/PANI nanocomposite electrodes at a scan rate of 100 mV/s and (b) 15c PANI deposited VACNT/PANI nanocomposite electrode at different scan rates.

GCD characteristics of the fabricated electrodes were also measured within a potential window of 0 - 0.8 V and at a current density of 0.25 mA/cm^2. Figure 2.9 (a) shows the obtained GCD curves of pristine VACNT and VACNT/PANI nanocomposite electrodes. At first sight the difference between the areas under the triangles are realized. In parallel with CV tests 5c and 10c electrodes exhibit higher performance than pristine VACNT electrodes but their individual performances are not quite different each other. However, 15c nanocomposite electrode has significantly higher capacitance rather than both 5c and 10c electrodes since its GCD curve covers larger area which means it stores more charge. This situation is attributed to the more effective PANI coating on 15c electrode in comparison with other nanocomposite electrodes. Quasi-symmetric properties with quite low internal

resistance drop were obtained from these samples. In order to further investigate the electrochemical characteristics of 15c PANI coated VACNT/PANI nanocomposite electrode GCD tests were taken at different current densities. Obtained GCD results are provided in Figure 2.9 (b). GCD characteristics were determined depending on the applied current density. Charge-discharge times were found to increase with decreasing current density. The typical triangle curve shapes were evident; however, with excessive asymmetry. The discharging times were shorter than the charging times indicating low Coulombic efficiencies for the fabricated electrodes. This behavior can be attributed to the special surface structure of the fabricated nanocomposite electrodes. As shown in Figure 2.4 (a), the fabricated nanocomposite electrodes have a complex surface structure. There are many holes on the surface. It is claimed that some electrolyte ions enter through the holes and reach the VACNT layer in the charging procedure. During the charging procedure ions propagate within the VACNT layer under the PANI layer. But in the discharging procedure ions far away from the holes cannot leave easily the electrode and thus the discharging procedure terminates early. Chu et al. [76] observed a similar behavior in PEDOT/graphene/carbon cloth composite electrode. The capacitance of the electrode gradually diminished with longer electrodeposition times. According to Chu et al. [76], different time-dependent deposition properties of PEDOT on the graphene/carbon cloth substrates could be arisen from the different growth mechanisms and morphological evolution of PEDOT on the substrates. As a result, the PEDOT on the graphene/carbon cloth formed a dense structure after long electrodeposition times and electrolyte ions could not access easily to the graphene/carbon cloth layer under the PEDOT layer.

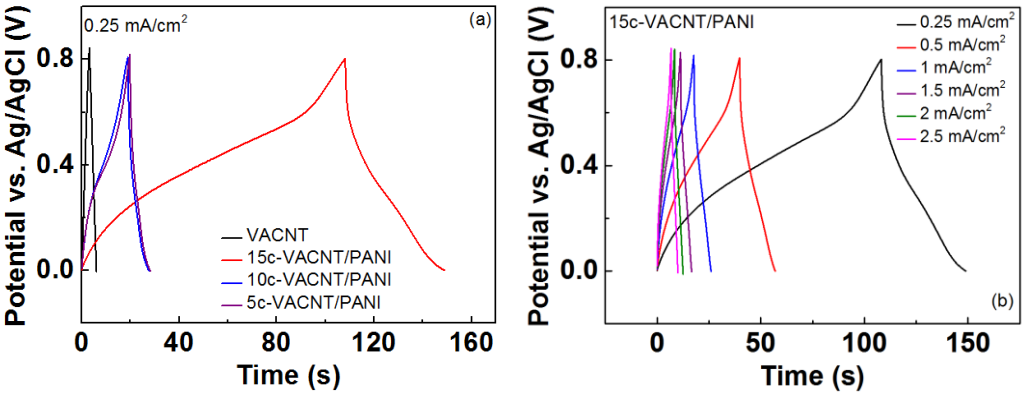

Figure 2.9. GCD curves of (a) pristine VACNT deposited aluminum foil electrode and 5c, 10c and 15c PANI deposited VACNT/PANI nanocomposite electrodes at a current density of 0.25 mA/cm^2 and (b) 15c PANI deposited VACNT/PANI nanocomposite electrode tested at different current densities.

The specific capacitance (C_{sp}) values of the fabricated nanocomposite electrodes were determined using the formula:

$$C_{sp} = \frac{I}{A\left(\frac{dV}{dt}\right)} \quad (2.1)$$

,where I is the discharge current, A is the electrode surface area, V is the discharge voltage and t is the discharge time. Discharge times were determined on the basis of Figure 2.9 (a) and capacitance values were calculated as 3.63, 3.46 and 16.17 mF/cm^2 for 5c, 10c and 15c PANI deposited VACNT/PANI nanocomposite electrodes, respectively. While 5c and 10c PANI deposited VACNT/PANI nanocomposite electrodes had similar capacitance values, 15c electrode had a 4 times higher capacitance. This difference is attributed to the effective deposition of PANI on top of the VACNT layer. Until 5 and 10 cycles of electrodeposition, the thickness of the PANI layer is not at the level where it could make a significant difference. In addition, electrodeposition cycles more than 15 were also examined within this study. After 15 cycles, the PANI coated VACNT layer started to leave the aluminum foil during the electrochemical tests. In the light of these observations and

experimental results, 15c PANI coated VACNT/PANI nanocomposite was considered as the most promising electrode.

In order to monitor the cyclic stability of the 5c, 10c and 15c PANI deposited VACNT/PANI nanocomposite electrodes, they were subjected to 3,000 GCD cycles. These tests were carried out under an applied current density of 2.5 mA/cm^2. Cycling performance of the fabricated electrodes is given in Figure 2.10. According to the obtained results, C_{sp} of 5c, 10c and 15c PANI deposited VACNT/PANI nanocomposite electrodes degrade to 73, 62 and 52% of their initial capacitance values, respectively. In contrast to CV and GCD results, 15c electrode exhibit lower performance with respect to 5c and 10c PANI deposited VACNT/PANI nanocomposite electrodes in terms of cycling. This case is ascribed to the high amount of PANI layer on 15c PANI deposited VACNT/PANI nanocomposite electrode. The PANI layer on 15c electrode deteriorates faster than the other nanocomposite electrodes and thus the capacitance diminished very rapidly. Another approach was proposed by Wang et al. [45], where graphene film was used to obtain good adhesion between the current collector and the active materials. Following 500 cycles, 63% of the initial specific capacitance of nickel(II) hydroxide ($Ni(OH)_2$)/graphene/nickel foam composites was maintained. On the contrary $Ni(OH)_2$/nickel foam composite showed an 84.5% decrease in the specific capacitance under the same test conditions. These results obviously showed that the presence of graphene film is useful for the improvement of the cycling stability of the electrodes. It was claimed that the good adhesion between graphene and $Ni(OH)_2$ is possibly arisen from the oxygen-containing functional groups found on the graphene surface. In the light of these explanations, for the current study, one can say that the content of the VACNT in the nanocomposite decreased with the increasing number of electrodeposition cycles of PANI and therefore the adhesion between the VACNT and PANI might be weakened simultaneously.

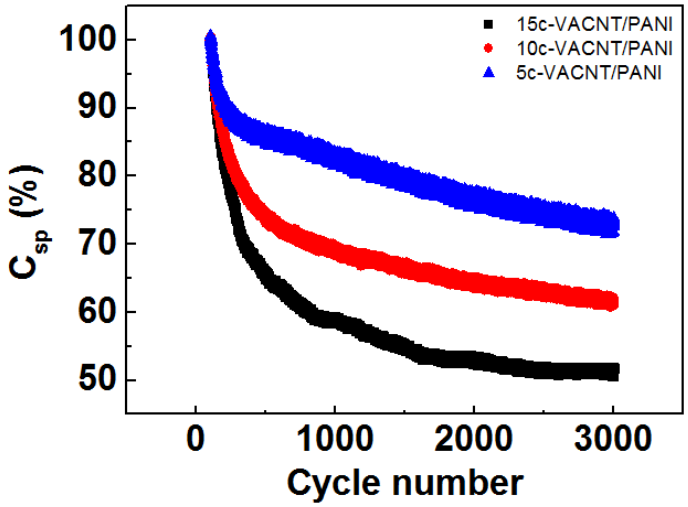

Figure 2.10. Capacitance retention of fabricated nanocomposite electrodes.

EIS is used for the further electrochemical characterization of fabricated electrodes. EIS tests were conducted with an AC perturbation of 5 mV and in a frequency range of 100 kHz to 10 mHz. Nyquist plot obtained from EIS measurements of both the nanocomposite and VACNT electrodes is provided in Figure 2.11. Supercapacitor electrodes behave like a resistance and like a capacitor in the high and low frequency region, respectively. The straight line in the low frequency region is a result of the pseudocapacitive character of the electrodes. The semicircle within the high frequency region shows the interfacial interactions between the electrolyte and the electrode. These interactions include the double-layer capacitance and charge transfer resistance. As shown in the inset of Figure 2.11, while the pristine VACNT electrode has the smallest semicircle, the semicircles of the nanocomposite electrodes are very wide and almost indistinct. This means that VACNT electrode has the lowest charge transfer resistance. 15c PANI deposited VACNT/PANI nanocomposite electrode has the low series resistance compared to other nanocomposite electrodes and the VACNT electrode. In this case one can say that the resistance of the nanocomposite electrodes decreases with increasing number of PANI coating cycles.

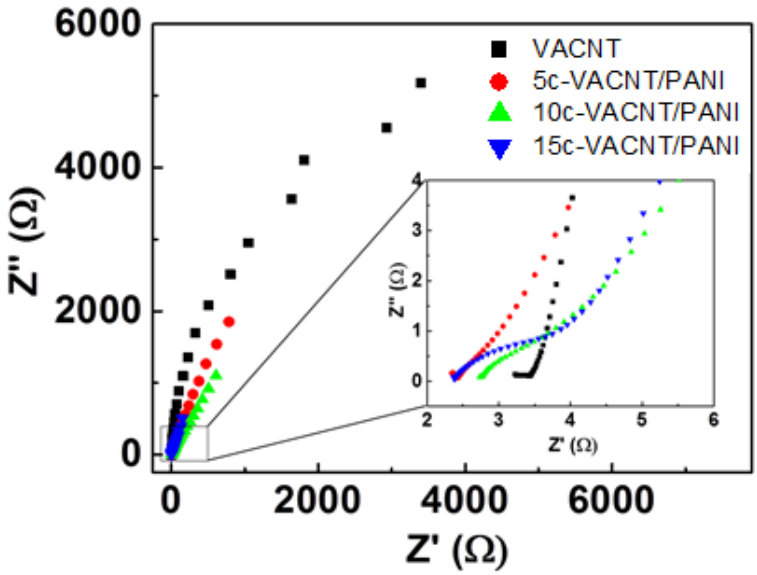

Figure 2.11. Nyquist plot for the fabricated nanocomposite electrodes. Inset shows the high frequency region.

2.4 Conclusions

In this study, a practical and cost-effective method to produce PANI/VACNT nanocomposite supercapacitor electrodes were developed. The properties of VACNTs and PANI to fabricate nanocomposite electrodes were combined. PANI layers were electrodeposited onto VACNTs grown on aluminum foils. Among the fabricated electrodes, nanocomposite with the largest PANI layer (15c) showed significant performance during CV, GCD and EIS tests. The specific capacitance of 15c electrode was calculated as 16.17 mF/cm^2 at a current density of 0.25 mA/cm^2. On the other hand, the cyclic performance of this electrode was determined to be lowest, probably because of the degradation of the PANI in open atmosphere. In addition, the increased number of PANI coating cycles decreased the VACNT amount of the nanocomposites and led to the reduction in the adhesion between the layers of the nanocomposites. In short 15c VACNT/PANI nanocomposite supercapacitor electrode is a promising energy storage device for supercapacitor applications with its notable properties. Cyclic performance of the fabricated

electrodes can be improved by properly sealing the devices under protective atmospheres.

CHAPTER 3

PAPER BASED, EXPANDED GRAPHITE/POLYPYRROLE NANOCOMPOSITE SUPERCAPACITORS FREE FROM BINDERS AND CURRENT COLLECTORS

3.1 Introduction

Multifunctional electronic devices or smart electronics gained extreme popularity in recent years mostly because of excessive consumer demand. Wearable, flexible, and paper-based electronics are the most prominent ones and soon their prototypes will leave the stage to real products in the market. Multifunctional electronics necessitate all their components to be compatible with each other as well as with the substrate [77–79]. Use of paper, a part of everyday life, as the substrate for a flexible electronic device is quite attractive thanks to its low cost, high flexibility and environmentally friendly structure [80]. For paper electronics, one of the most important components is the power unit. Right now, cable connected external power supplies, incompatible watch batteries, and wireless energy transfer are used to power up paper electronics [81–83]. For the realization of truly paper-based electronics, it is an important practice to fabricate a compatible power unit directly on paper [77,84–86]. Supercapacitors are alternative power sources and complementing batteries particularly in high power demanding applications. Therefore, fabrication of supercapacitors on paper is strategically important and highly promising for the realization of truly paper-based electronics. Schematic illustrations of paper-based supercapacitors with a common sandwiched architecture and an alternative in-plane architecture are shown in Figure 3.1.

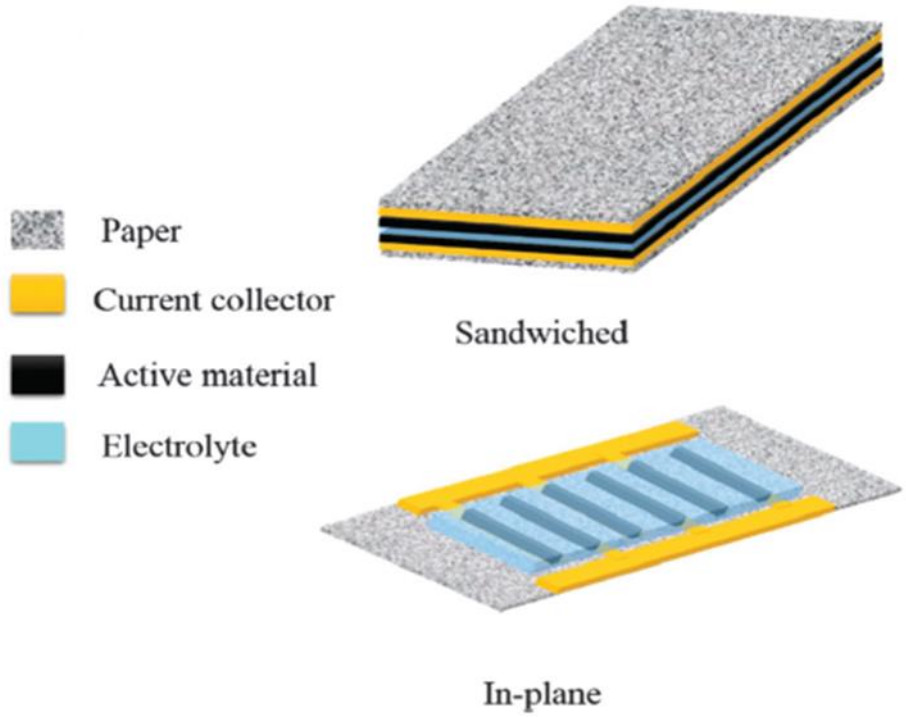

Figure 3.1. Schematic illustrations of paper-based supercapacitors with sandwiched and in-plane architectures [80].

Supercapacitors are currently utilized in many systems ranging from electric vehicles to mobile electronics thanks to their high-power density and rapid charge-discharge characteristics. Supercapacitors can be fabricated with a broad variety of form factors from traditional device structure to flexible [87,88], bendable [89], or stretchable structures [90,91]. These new form factors allow the realization of truly flexible electronics. In literature, most of the investigated supercapacitor electrodes were fabricated using slurry coating methods. These electrodes contain insulating binders that increase the overall series resistance, which results in low electrochemical performance of the supercapacitor. In addition, to decrease the resistivity of the fabricated electrodes, conductive additives are added to the prepared slurry, which increases the mass of fabricated electrodes with no capacitive contribution. Moreover, metallic current collectors are also used in current commercial supercapacitor devices to improve the charge collection. Thus,

fabrication of supercapacitor electrodes that are free from binders, conductive additives and heavy metallic current collectors has utmost importance to enhance the electrochemical energy storage performance of novel systems [92,93].

Carbonaceous materials are extensively utilized in electrochemical energy storage systems [94]. Two-dimensional carbonaceous materials such as graphene and graphitic structures possess high conductivity and specific surface area, which were already reported as advantageous for energy storage devices [94,95]. Graphene on paper has already been demonstrated also as supercapacitor electrodes [96]. The specific capacitances of the carbonaceous materials are relatively less compared to pseudocapacitive materials. On the other hand, cycle life of carbon-based materials is much longer than the pseudocapacitive counterparts [93]. Long service life in conjunction with high durability against capacitance loss are crucial properties for the supercapacitor devices. Development of novel electrode active materials with improved charge accumulation and transfer through the formation of nanocomposites [97] and hierarchical structures [98,99] are highly critical for the enhancement of the electrochemical performance of the supercapacitors [4,22,23]. During the in-situ polymerization of conducting polymers on 2D carbon materials, interactions such as hydrogen and π- π stacking bonding between polymer and graphitic layers affect the polymer's structure and morphology. These interactions enhance the stability of conducting polymers and cycle life of the fabricated nanocomposites [100,101]. Active surfaces of graphitic 2D materials allow the electrodeposition of pseudocapacitive materials [97]. Multi-layered graphene or expanded graphite (EG) is derived from the deoxygenation of the graphite oxide via different routes [102]. Among these, the microwave-assisted route is highly promising for the mass production and thus the utilization of EG material in many fields.

Metal oxides and CPs are two main pseudocapacitor type material groups, and they store charges on the surface of electrode material via fast and reversible redox reactions. Among pseudocapacitors, CPs are important materials; because they have intrinsically electronic conductivity changing with their level of doping. In

addition to this, their low cost and easy processability make them promising materials for electrochemical energy storage devices [84,103,104]. For supercapacitor studies, most frequently utilized CPs are PEDOT, PANI, PPy, and their derivatives. CPs commonly suffer from changes in volume during ion intercalation and deintercalation, causing mechanical deformation [84,104]. PPy, differs from other CPs with its distinctive mechanical properties, biocompatibility, high conductivity and rapid redox activity [99,103]. These features result in the utilization of PPy for various electronic systems such as supercapacitors, batteries, and fuel cells [105], photoelectrochromics, sensors [106], corrosion protection [107], and solar cells [108]. The prominent disadvantage of PPy, similar to other CPs, is the limited cycle life and the main reason for this drawback is the instabilities within the polymer backbone. To improve the electrochemical properties and structural stability of the polymer, nanocomposite formation with PPy is the most commonly practiced method for its utilization in supercapacitors. Multi-walled carbon nanotubes [109–111], single-walled carbon nanotube [112], carbon fibers [113], activated carbon [114], carbon foam [115], molybdenum sulfide [104], silver [115], titanium carbide [116], reduced graphene oxide [117], and graphene [118] were used to fabricate PPy nanocomposites and these nanocomposites resulted in both the improvement of the structural stability of polymer and the enhancement of electrochemical properties of PPy nanocomposites.

Paper-based supercapacitor electrodes are formed by combining electrochemically active materials with cellulose fibers in composite form. These composites consist of repeating cellobiose structures with high aspect ratio. They contain strong inter- and intra-molecular hydrogen bonds resulting in fibers with hydroxyl-functionalized surfaces [80]. These characteristics make cellulose fibers very efficient structural components and they are typically combined with popular active materials such as graphene [96], CNTs [119], PANI [120], and PPy [121]. Moreover, cellulose fiber networks form pathways in a paper substrate and improve the ion transport [122].

In this study [123], paper-based EG/PPy nanocomposite electrodes were fabricated via simple brush-painting of highly conductive EG sheets onto paper followed by the electrodeposition of PPy. This hierarchical structure of EG/PPy was then used as supercapacitor electrodes without the requirement for heavy current collectors, conductive additives and binders. Electrochemical behaviors of the prepared paper-based nanocomposite electrodes were examined both in three-electrode cell and also in a symmetric supercapacitor device.

3.2 Experimental

Sample preparation: Natural graphite, pyrrole monomer (%98), polyvinyl alcohol (PVA, Mowiol 10–98), potassium chloride (KCl, ≥99%), concentrated nitric acid (HNO_3), H_2SO_4, and all other reagents had analytical grade and obtained from Sigma-Aldrich. A4 type matte, glossy, greaseproof and conventional printing papers were purchased from the local office store. All of the chemicals and reagents were used as received without purification.

Natural graphite flakes were kept in a concentrated acid solution (3:1, H_2SO_4: HNO_3) for five days. After that they were filtered, rinsed with plenty of water until the pH was 7. Then the acid exposed graphite flakes were dried in a vacuum furnace for 24 hours at 80°C. After that dried graphite oxide flakes were put in a commercial microwave oven and irradiated at 800 W for 10 s. The microwave irradiation caused the rapid expansion of graphite layers and led to the formation of EG flakes [124–126]. Prepared EG flakes were placed in a tip sonicator and dispersed in dimethylformamide (DMF). After that they simply brush-painted onto paper pieces (10×10 cm). The sheet resistances of the EG deposited paper substrates were determined with the EG loading. Prior to further utilization, the EG paper electrodes were cut into small pieces with dimensions of 2 cm × 2.5 cm.

PPy was potentiostatically deposited onto the EG paper electrodes. Each time, a fresh 0.1 M Py monomer was mixed with 1 M KCl as the electrolyte solution,

and this mixture was used for the conformal deposition of PPy onto EG paper working electrodes. EG paper working electrode was immobilized onto a glass substrate using Kapton tape, and the active electrode size was set to 1.5 cm × 2.0 cm for electrodeposition. The counter and reference electrodes were platinum foil and Ag/AgCl (saturated KCl), respectively. Coating of PPy was carried out with a constant potential of 0.9 V and it is applied for 200, 400, 600 and 800s. Prepared electrodes were washed with DI water, dried under nitrogen flow and kept in an oven at 80°C overnight.

Characterization: The morphology of the produced electrodes was examined using SEM (FEI Nova Nano FEG-SEM 430, used at 10 kV). XRD analysis was conducted on a Rigaku D/Max-2000 diffractometer using Bragg-Brentanno geometry with Cu Kα radiation at 40 kV. Raman spectroscopy was conducted on a Renishaw inVia Raman microscope (wavelength: 532 nm). FTIR tests were conducted by an Agilent 600 Series FTIR spectrometer in ATR mode. XPS measurements were conducted for the analysis of the chemical state and determination of the constituent elements. All XPS spectra were shifted +1.5 eV due to over-charge compensation with respect to C1s spectrum. For electrochemical tests, Gamry Reference 3000 potentiostat/galvanostat system was employed both in three and two-electrode cells. For two-electrode measurements, PVA/H_2SO_4 polymer electrolyte was employed without a separator and the electrolyte was prepared by using 2 g of concentrated H_2SO_4 and 2 g PVA in 20 ml of deionized water at 95°C with constant mixing until a clear solution was observed. For three-electrode measurements, 1 M H_2SO_4 electrolyte solution was used and all potentials were monitored with respect to Ag/AgCl (saturated KCl) reference electrode. A Sartorius Research R200D microbalance was employed to determine the weight of electrodes. Masses of electrode active materials were calculated from the mass difference between bare paper substrates, EG electrodes and EG/PPy coated electrodes.

The C_{sp} of the produced electrodes in three-electrode configuration was determined from GCD curves using the formula:

$$C_{sp} = \frac{I}{m\frac{\Delta V}{\Delta t}} \quad (3.1)$$

,where I (A) is the applied discharge current, Δt (s) is the total time of discharge, m (g) is the mass of electrode active materials, and ΔV (V) is the discharge potential window after IR drop.

3.3 Results and Discussion

Microwave-assisted exfoliation of graphite resulted in the production of high-quality EG (or multi-layered graphene sheets) and these sheets were highly promising for paper-based electronics due to their high conductivity and natural flexibility. EG were dispersed via probe-sonication to form a homogeneous slurry in DMF and then simply brush-painted onto matte paper. In this work, matte paper is referred as just paper. Fabrication process of the EG coated conductive papers and EG/PPy nanocomposite electrodes are schematically demonstrated in Figure 3.2 (a). After each brush painting cycle, papers were dried on a hotplate at 120°C and unattached tiny EG layers were then removed using a dry brush. This coating cycle was repeated until the desired sheet resistance values were obtained. The necessary parameters for the fabrication of conductive EG coated paper electrodes were the EG ink solution concentration and the drying temperature of the electrodes; both of which were tuned for the reproducible fabrication of the electrodes. Following the fabrication of EG paper electrodes, pyrrole monomer was electrochemically polymerized to PPy at different deposition times. KCl electrolyte was used as the supporting electrolyte to keep the ionic conductivity constant during the PPy deposition. PPy deposition was practiced for 200, 400, 600 and 800 seconds.

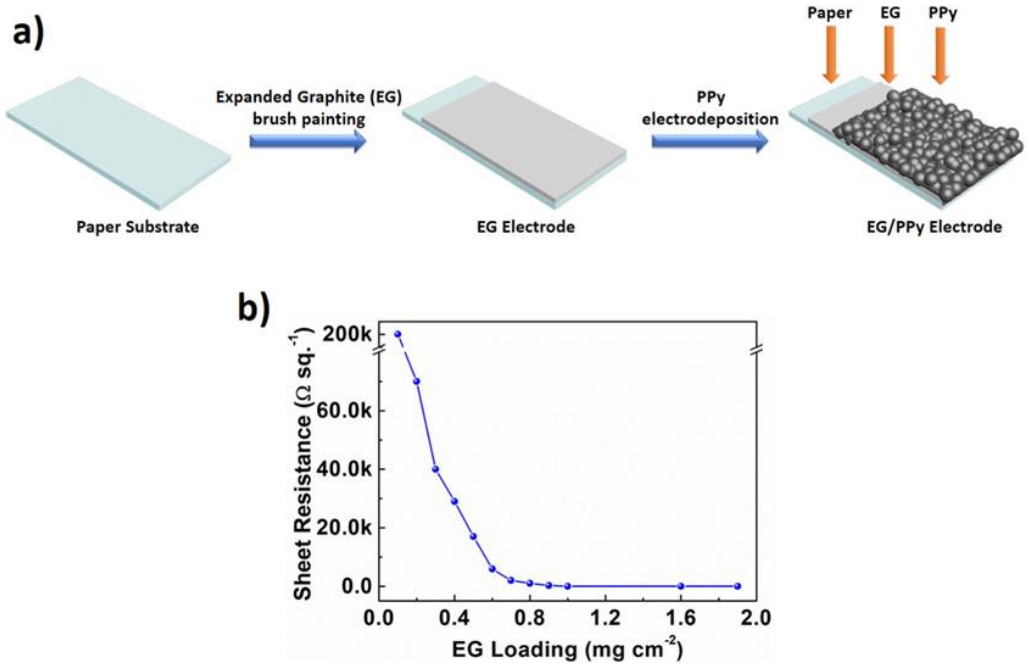

Figure 3.2. (a) Schematic illustration of EG/PPy nanocomposite fabrication and (b) sheet resistance change with respect to EG loading on paper substrate.

In Figure 3.2 (b), the effect of EG areal density on the sheet resistance of the fabricated EG paper electrodes is demonstrated. As shown in the figure, sheet resistance decreased sharply with the first few depositions (approximately 0.7 mg/cm^2) because EG sheets on the paper start to form conducting pathways between graphene flakes. Sheet resistance change was very limited following the obtainment of an areal EG density of 1.0 mg/cm^2 (corresponding to 30 Ω/sqr.). The highest EG loading for fabricated EG electrodes was 1.9 mg/cm^2 (corresponding to 15 Ω/sqr.). For the PPy deposition, an EG density of 1 mg/cm^2 was chosen as the standard value since this density provided a reasonable conductivity value and the film was very durable during both the PPy deposition and electrochemical measurements in electrolytic media. The electrodes investigated here are inexpensive and disposable, and can be easily fabricated over large areas.

SEM was employed to investigate the surface morphologies of the fabricated EG and EG/PPy nanocomposite electrodes. SEM images of microwave EG sheets, EG coated paper, and EG/PPy nanocomposite electrodes are shown in Figure 3.3 (a),

(b), and (c) respectively. Oxidized graphite flakes were expanded and reduced to thin graphite layers during microwave irradiation where instant heating of graphite oxide flakes created local heating spots and sparks formed. Instant increase in temperature resulted in the volume expansion and formation of worm-like reduced graphite structures with expanded layers. High magnification SEM images of EG/PPy samples on paper showed the formation of polymer nanoparticles on the EG electrode. It is obvious from SEM analysis that the globular PPy particles were homogeneously deposited onto EG sheets. Direct deposition of the PPy onto the EG resulted in the improved charge transfer, enhanced electrochemical properties and mechanical integrity.

In-situ electrochemical polymerization of pyrrole monomer occurred on the surface of EG electrodes and a hierarchical formation of the EG/PPy nanocomposites was produced as illustrated schematically in Figure 3.2 (a). Fabricated EG electrodes were used as conductive substrates for PPy electrodeposition without any conductive additive or external contact points. PPy was homogeneously deposited onto EG coated paper substrates as shown in the inset of Figure 3.3 (d). Continuous and conformal coating of a PPy layer on graphene papers was a time and concentration-dependent process. In this work, Py monomer concentration was kept constant during the PPy electrodeposition.

In order to examine the effect of paper type on EG coating; apart from the matte paper, EG was also coated on conventional printing paper, glossy paper, and greaseproof paper. Conventional printing paper was too soft for brush painting and was not durable in electrolyte solutions during electrochemical measurements. In Figure 3.4 (a) and (b), SEM images of EG coating on glossy paper and greaseproof paper are shown, respectively. As seen in these images and the SEM image of EG coating on matte paper shown in Figure 3.3 (b), there are no morphological differences in the particles. EG flakes are quite visible on all three types of papers. However, problems related to the absorption of EG/DMF slurry in glossy and greaseproof papers were encountered during brush painting. Thus homogeneities of the coatings on these papers were low. On the other hand, the matte paper was

observed to be quite stable in aqueous media, because the matte paper surface is textured and less lustered. Thus, matte paper with improved mechanical properties was utilized for the further experiments in this study.

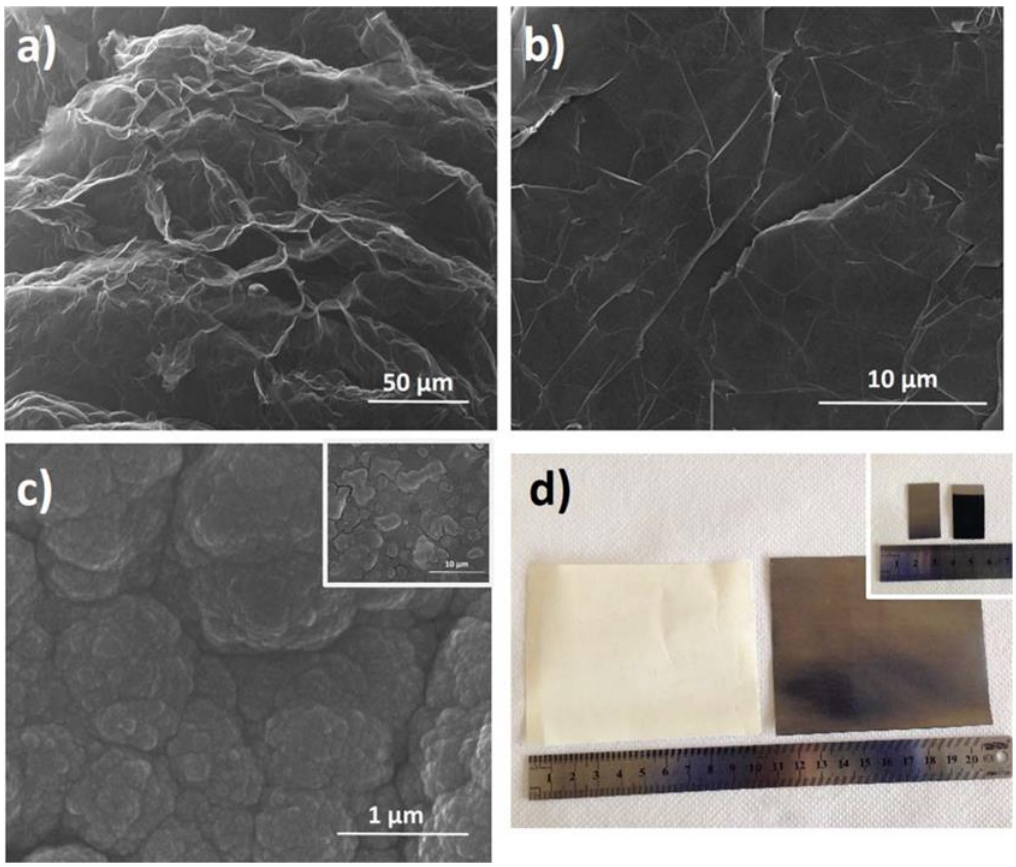

Figure 3.3. SEM images of (a) EG layers, (b) EG deposited paper electrodes, and (c) 800 sec. PPy electrodeposited on EG paper electrode. The inset shows low magnification SEM image. (d) Photographs of blank paper and EG deposited paper electrodes. The inset shows the bare EG and PPy electrodeposited EG electrodes.

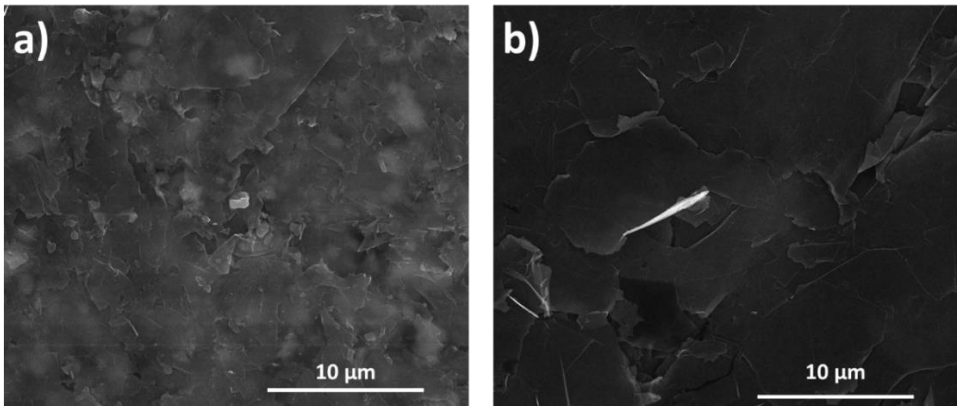

Figure 3.4. SEM images of EG coatings on (a) glossy paper and (b) greaseproof paper.

The crystal structure of the bare EG and EG/PPy nanocomposite electrodes were examined by XRD. XRD patterns of the EG and EG/PPy nanocomposites on paper substrates are shown in Figure 3.5 (a). EG showed diffraction peaks at 26.6° and 54.7°, which correspond to (002) and (004) crystal planes of graphitic carbon (JCPDS card no. 75-1621), respectively. XRD pattern for EG/PPy nanocomposites had peaks associated with EG corresponding to the graphitic carbon and a broad region due to the amorphous nature of PPy.

Chemical structure of the fabricated electrodes was investigated through Raman analysis. The results of Raman analysis of the bare EG sheets and produced EG/PPy nanocomposites on paper substrates in the spectral range of 500–3500 cm^{-1} are shown in Figure 3.5 (b). The observed peaks in the Raman spectrum of EG deposited paper were due to the graphitic carbon. EG/PPy nanocomposite electrodes had broad Raman signals. The Py ring stretching showed bands at 1365 cm^{-1} and the peak at 1603 cm^{-1} was attributed to stretching of the C=C bonds. To further characterize the chemical structure of the bare EG and EG/PPy nanocomposite electrodes, FTIR analysis was performed, results of which are provided in Figure 3.5 (c). For EG, any significant signal could not be observed in the FTIR spectrum. On the other hand, the characteristic PPy peaks were determined for EG/PPy nanocomposites. The band at 3450 cm^{-1} was because of the OH stretching and the bands at 1550 and 1477 cm^{-1} were related to the pyrrole ring and C-N stretching,

respectively. The bands located at 1383 and 924 cm^{-1} were assigned to C-H stretching mode. C-N stretching modes showed bands at 1303 and 1188 cm^{-1} and in-plane N-H vibration mode had a band at 1041 cm^{-1}. The peak at 783 cm^{-1} was assigned to the out-of-plane ring vibration mode of C-C and C-H bonds [127].

XPS analysis were carried out to further analyze the chemical structure of the fabricated EG/PPy nanocomposite electrodes. XPS results of bare EG and EG/PPy nanocomposites on paper substrates are provided in Figure 3.5 (d–f). XPS general spectrum of the bare EG and nanocomposite EG/PPy had signals from C, O, N species (Figure 3.5 (d)), which came from the components of PPy and EG. According to XPS survey scan results, C/O ratios were found as 11.6 and 6.16 for the bare EG and EG/PPy nanocomposites, respectively. For EG, the high-resolution C1s core level XPS spectrum (Figure 3.5 (e)) exhibited only one peak. EG/PPy spectrum, on the other hand, had a broader C 1s peak than the bare EG spectrum. Deconvoluted high resolution C1s spectra showed that EG electrode had C-C and C-O peaks, while EG/PPy nanocomposite had C-C and C-N peaks and C-N peak was attributed to PPy. No N 1s peak was observed for bare EG electrodes (Figure 3.5 (f) inset) since EG electrodes had no nitrogen moiety. On the other hand, a highly intense N 1s peak was obtained from the EG/PPy nanocomposite due to the PPy moiety. High-resolution O1s signal was found to shift toward lower binding energies due to different oxidation values upon nanocomposite formation (Figure 3.5 (g)).

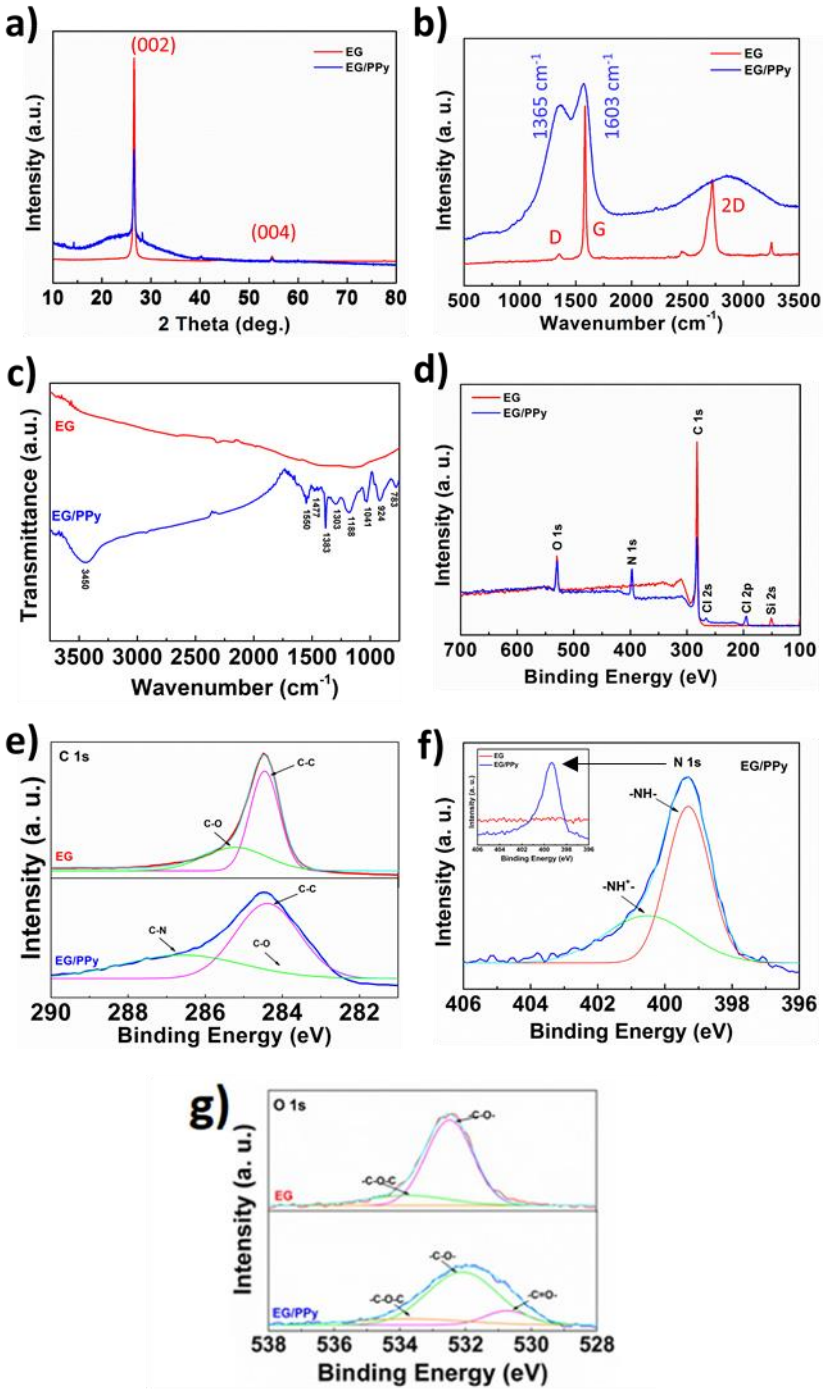

Figure 3.5. (a) XRD patterns, (b) Raman spectra, (c) FTIR spectra and, (d) XPS survey spectra of the fabricated paper-based bare EG and 800 sec. electrodeposited EG/PPy nanocomposite electrodes. High-resolution core-level (e) C1s, (f) N1s, and (g) O1s spectra of bare EG and 800 sec. electrodeposited EG/PPy nanocomposite.

Electrochemical characteristics of the prepared bare EG electrodes were examined in the two-electrode cell using a solid PVA/H_2SO_4 electrolyte. Bare EG paper electrodes were not examined in the three-electrode cell due to the electrochemical exfoliation of EG sheets during the measurements, which severely damaged the electrodes. Paper-based EG supercapacitor devices were fabricated without any external current collectors, binder, separator and conductive additives. Fabricated supercapacitor devices without these components were very advantageous to decrease the total mass of the full device. It is well known that most of the device mass comes from the metallic current collectors and packaging.

CV results of brush painted paper-based EG supercapacitor devices at various scan rates are provided in Figure 3.6 (a). Rectangular curve shapes within the CV cycles of the EG supercapacitors were retained at high scan rates. GCD measurement results for fabricated EG devices are provided in Figure 3.6 (b). Almost isosceles triangular GCD curve shapes were obtained for all current densities and fabricated samples showed low internal resistance drop. In fabricated supercapacitor devices, EG coated electrodes were used both as a current collector and capacitive active material. It is believed that high active material loading improves the capacitance of the fabricated supercapacitor devices. On the other hand, the intention was to use EG as a current collector for the EG/PPy nanocomposite supercapacitors. EIS spectrum was recorded within a range of 100 kHz to 10 mHz with 5 mV AC perturbation. EIS results of the EG supercapacitor device revealed an ESR value of less than 20 ohms, as clearly seen in the high frequency region (Figure 3.6 (c) inset). A sharp and linear slope was obtained for the EG supercapacitor devices within the low frequency region. Capacitance retention and stability of fabricated EG supercapacitor devices were also evaluated. After 5,000 GCD cycles, almost the same capacitance value was obtained as shown in Figure 3.6 (d).

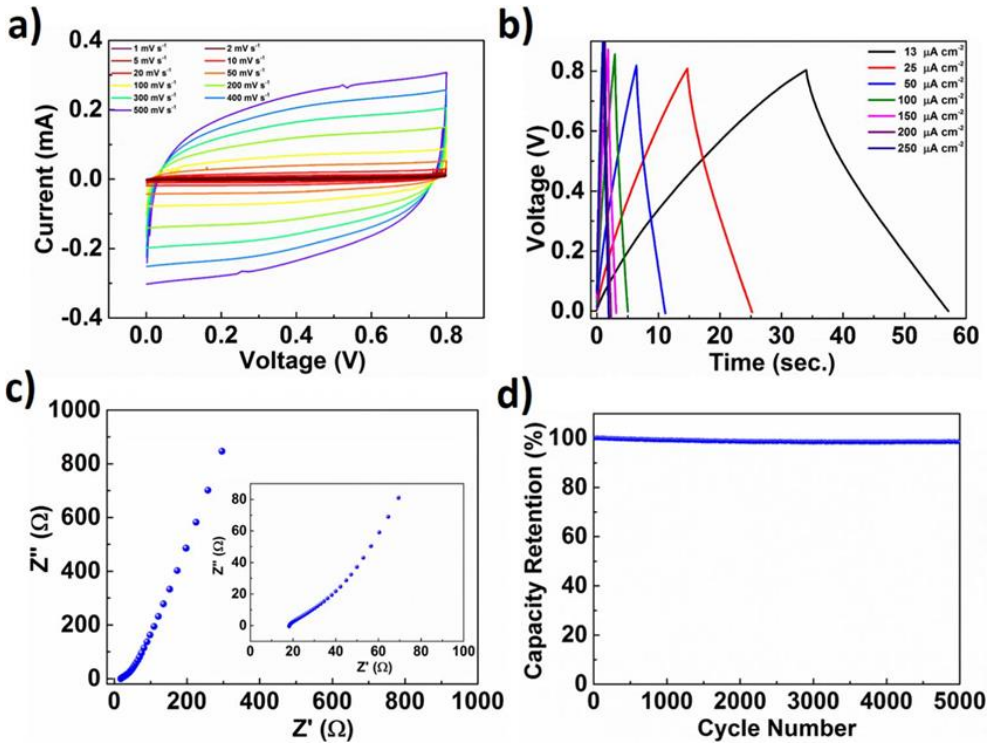

Figure 3.6. (a) CV results of EG supercapacitor at various scan rates from 1 to 500 mV/s, (b) GCD curves at different current densities from 13 to 250 μA/cm^2, and (c) impedance spectra within a range of 100 kHz to 10 mHz. The inset shows the high-frequency region of the EIS spectra. (d) Capacitance retention of EG supercapacitor for 5,000 GCD cycles.

The electrochemical performance of EG/PPy nanocomposite electrodes were evaluated in three-electrode configuration, and CV measurements (Figure 3.7 (a)) were conducted within a potential window of 0 to 0.8 V (vs. Ag/AgCl) in 1 M H_2SO_4 electrolyte solution. Capacitance contribution of the electrodeposited PPy was monitored using different PPy deposition times. Following PPy deposition, physical integrity of the electrodes was improved and their electrochemical performance was remarkably increased. Increased deposition times enlarged the CV curves and 800 seconds PPy deposited electrode showed the highest charge collection. All samples had a similar CV curve shape and very broad redox peaks were observed. GCD results of the prepared EG/PPy nanocomposites electrodes were provided in Figure 3.7 (b). Produced nanocomposite electrodes exhibited limited IR drop and had nearly

triangular GCD curve shapes. Similar to CV results, increased PPy deposition also led to longer GCD times and capacitance was increased with the deposition time. Increased PPy deposition time not only improved the capacitance; but also decreased the serial resistance, as evidenced in Nyquist plot in Figure 3.7 (c). Comparison of the cycle life properties of the fabricated nanocomposite supercapacitor electrodes (Figure 3.7 (d)), revealed the fact that PPy enhanced structural stability of the electrodes. 800 seconds deposited electrode showed the best capacitance retention value. 200 seconds PPy deposited EG/PPy nanocomposite showed the worst performance and after 5,000 GCD cycles, it lost 59% of its initial capacitance.

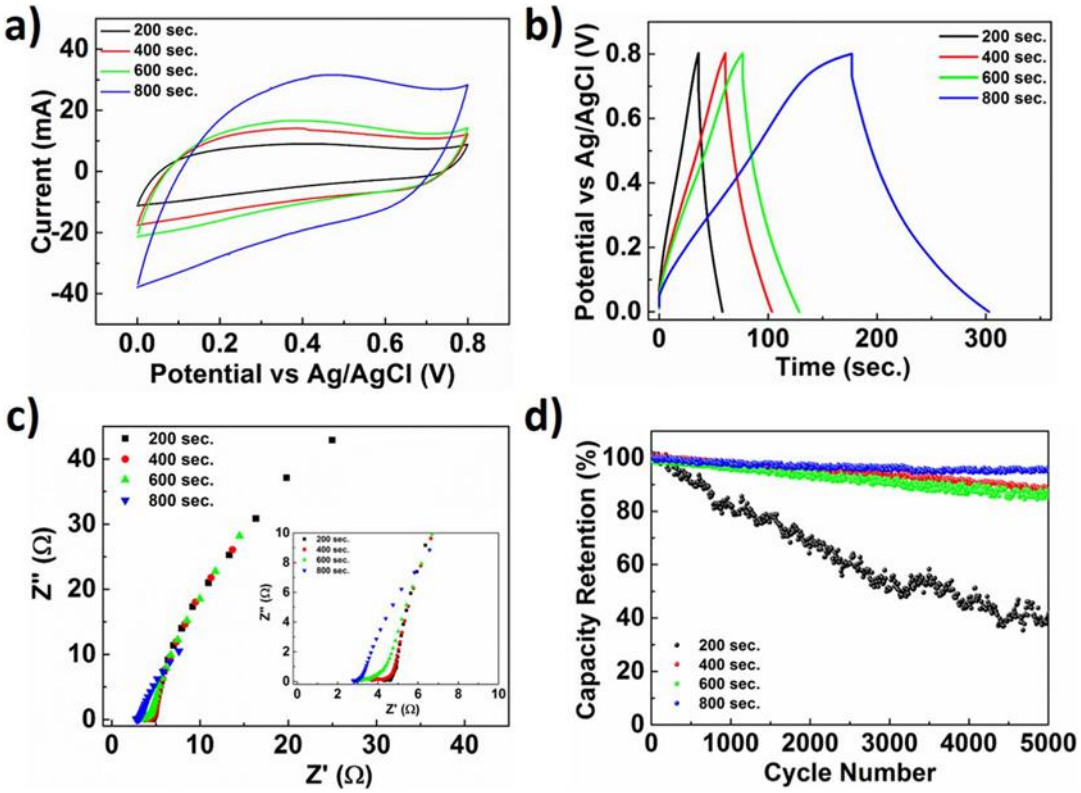

Figure 3.7. Electrochemical characteristics of EG/PPy nanocomposites with various PPy deposition times from 200 to 800 seconds. (a) CV results at 20 mV/s, (b) GCD curves at a current density of 2.5 mA/cm^2, (c) impedance spectra within a range of 100 kHz to 10 mHz. The inset shows high-frequency regions of the EIS spectra. (d) Capacitance retention of fabricated nanocomposite electrodes at a current density of 5 mA/cm^2.

To further determine the electrochemical behavior of the EG/PPy nanocomposite electrodes, 800 seconds PPy deposited nanocomposite electrode was tested at different CV scan rates ranging from 1 to 100 mV/s in a 1 M H_2SO_4 electrolyte solution. CV results are provided in Figure 3.8 (a). The quasi-rectangular CV shapes were obtained for slow scan rates and there was a small deviation from the shape at high scan rates. GCD measurements were also recorded to observe electrochemical energy storage properties of the 800 sec. PPy deposited sample at various current densities. As provided in Figure 3.8 (b), GCD curves have almost linear shapes. An insignificant IR drop was seen at low current densities. This IR drop was mainly because of the ESR, which occurs at the electrode and electrolyte interface. The areal specific capacitance values of the produced EG/PPy nanocomposites at various current densities are given in Figure 3.8 (c). As the PPy coating time was increased from 200 to 800 seconds, the C_{sp} was found to get enhanced remarkably at all current densities. For 800 second deposited sample, capacitance value just decreased to 329.7 from 510.3 mF/cm^2 although current density was increased for eight times. Samples retained the high capacitance values at all current densities, which showed strong potential for the production of high-power supercapacitors. Specific capacitance values of fabricated nanocomposite electrodes and their masses are tabulated and provided in Table 3.1. In supercapacitors, the ratio between the discharge and the charge time is called Coulombic efficiency. In Figure 3.8 (d) Coulombic efficiency values, calculated from the GCD curves given in Figure 3.8 (b), are provided with respect to changing current densities. It is observed that Coulombic efficiencies were in the 60-70% band and decreased with current density. While the highest value was 70.1% at 2.5 mA/cm^2, the lowest value was 60.7% at 10 mA/cm^2. It is seen that when the current density increased to 10 from 2.5 mA/cm^2, the Coulombic efficiency decreased by 13.4%.

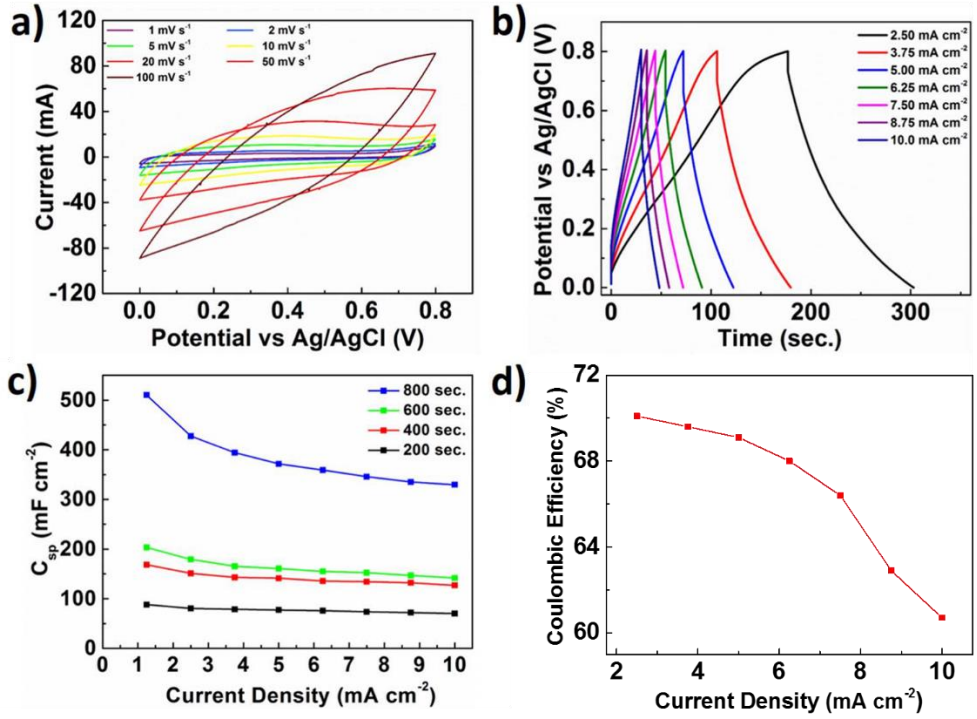

Figure 3.8. (a) CV curves at various scan rates from 1 to 100 mV/s and (b) GCD curves at different current densities from 2.5 to 10 mA/cm^2 of 800 seconds PPy deposited EG/PPy nanocomposite electrode. (c) *Csp* of the fabricated nanocomposite electrodes as a function of GCD current density and (d) Coulombic efficiency values at different current densities derived from Figure 3.8 (b). Lines are for visual aid.

Table 3.1 Change in the PPy mass and specific capacitance with respect to PPy deposition time.

Deposition time (sec)	*PPy mass (mg)*	*Specific capacitance (F/g)*
800	2.87	177.8
600	2.34	86.9
400	1.94	86.7
200	1.14	77.2

In order to investigate device performance of the paper based EG/PPy nanocomposite electrodes, 800 second PPy deposited nanocomposite electrodes were analyzed in two-electrode cell (full device) using PVA/H_2SO_4 solid electrolyte. In Figure 3.9 (a), the CV curves of bare EG and EG/PPy supercapacitor devices were provided in a voltage window of 0 – 0.8 V. Charge storage properties of bare EG device was remarkably enhanced with the nanocomposite formation. The pseudocapacitive contribution of PPy in nanocomposite was dominant when compared to bare EG and quasi-rectangular CV curve form was obtained for the EG/PPy device. This quasi-rectangular CV curve shape was also preserved at high scan rates, as shown in Figure 3.9 (b). Charge storage characteristics of the nanocomposite supercapacitor devices were also examined through GCD measurements. Almost symmetric GCD curves with limited IR drop was obtained for the EG/PPy device at various current densities (Figure 3.9 (c)). IR drop was mainly due to the low conductivity of PVA/H_2SO_4 solid electrolyte compared to its the aqueous counterparts. On the other hand, PVA/H_2SO_4 solid electrolyte provided better mechanical integrity and stability than the aqueous electrolytes. In PVA/H_2SO_4 solid electrolyte, fabricated nanocomposite supercapacitor devices showed promising capacitance retention of 90.6% following 5,000 GCD cycles, as shown in Figure 3.9 (d).

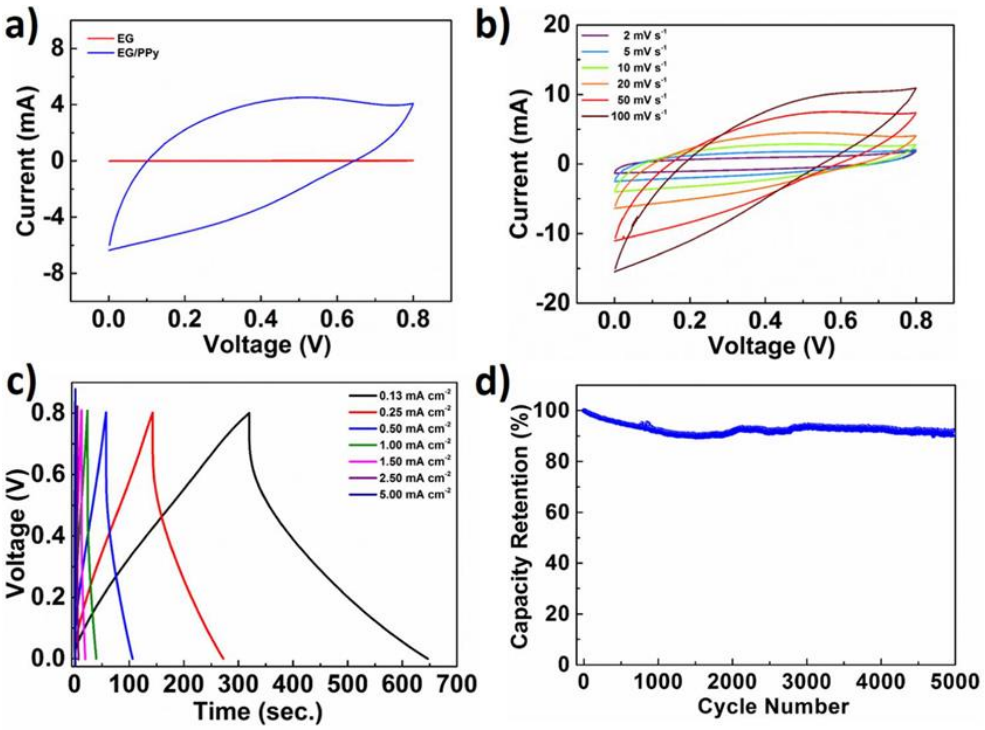

Figure 3.9. (a) CV results of fabricated bare EG and EG/PPy nanocomposite supercapacitor devices at a scan rate of 20 mV/s, (b) CV curves of EG/PPy device at various scan rates from 2 to 100 mV/s, (c) GCD curves of EG/PPy device at different current densities from 0.13 to 5 mA/cm^2, and (d) Capacitance retention for the nanocomposite device at a current density of 0.5 mA/cm^2.

3.4 Conclusions

In summary, paper based EG/PPy nanocomposite supercapacitor electrodes with tunable PPy content were fabricated. EG was utilized as the conductive layer for PPy coating and also for charge accumulation within the nanocomposites with a limited capacitance contribution. Fabricated supercapacitor devices were highly flexible and showed promising mechanical integrity among components and the paper. Electrodes delivered high specific capacitance and had remarkable capacitance retention. It is believed that the rapid fabrication process reported herein and elimination of separator, binder, conductive additives, and heavy metal current

collectors are clear advantages for the large-scale production of flexible and lightweight supercapacitors to power up paper-based electronics.

CHAPTER 4

NANOCOMPOSITE SUPERCAPACITOR ELECTRODES BASED ON CARBON NANOFLAKES PRODUCED BY INDUCTION COUPLED PLASMA AND MANGANESE DIOXIDE

4.1 Introduction

Research towards exploration of novel and hybrid supercapacitor electrode materials necessitate reproducible and large scale synthesis of nanomaterials [39]. Induction coupled plasma (ICP) synthesis method is one of those methods, where highly crystallized nanomaterials with high purity can be synthesized in large quantities. In ICP technique, precursors are sent into direct current (DC) or radio frequency (RF) thermal plasma in which the temperature is high enough (e.g. 10,000 K) to vaporize the all kinds of materials. The vapor then accumulates into nanoparticles within the quenching component of the system. The utilization of ICP is significantly attractive because it allows formation of large volume, contamination free, and high enthalpy plasma. In addition, it allows long exposure time of precursors in the high temperature zone. ICP has been utilized for the nanoparticle production of various materials [128]. Zhang et al. [129] produced nanoparticles with near spherical shapes with diameters of 100 nm and revealed that not only nanospheres but also nanosheets can be synthesized using ICP system. Pristavita et al. [130] synthesized carbon nanopowders with crystalline structure via plasma decomposition of methane using an ICP system. The synthesized powders collected from the system showed a uniform flake-like morphology. These powders, called carbon nanoflakes (CNFs), had typical lengths and widths of 100 and 50 nm, respectively with a thickness of 5 nm. High resolution TEM images revealed stacks of 6 to 16 graphene layers in these powders.

Among all the oxide-based electrode materials, MnO_2 is known for its low-cost, high specific capacitance, abundance and environmentally friendly structure. It is also one of the few true pseudocapacitive materials that has no redox peaks on cyclic voltammograms and no voltage plateau during discharge [131]. The pioneering study on the pseudocapacitive character of MnO_2 in an aqueous electrolyte was presented in 1999 by Lee and Goodenough [132]. Typically, hydrated MnO_2 shows specific capacitances within the 100–200 F/g band in alkali electrolytes. Having a wide variety of crystal forms, defect structure, morphology, texture, and porosity, MnO_2 shows various distinct electrochemical properties. The capacitance of bulk MnO_2 electrodes is unfortunately restricted by the insufficient electrical conductivity of MnO_2. Similarly, supercapacitive performance of a planar ultrathin design is limited due to the low mass loading. Thus, compounding different conducting materials and MnO_2 has been extensively proposed to enhance the electrical conductivity and charge-storage ability of such electrodes [133].

In this study, CNF-MnO_2 nanocomposite supercapacitor electrodes were fabricated. CNFs with promising supercapacitive properties were synthesized via ICP system. In order to investigate the electrochemical properties of CNFs, they were used as bare CNF electrodes and in nanocomposite form with MnO_2. MnO_2, synthesized through solution means, was chosen to complement CNFs in the nanocomposites since its electrochemical properties are well-known in literature. Comparison of the properties of bare CNF and MnO_2 electrodes with the fabricated nanocomposite electrodes, allowed to determine the underlying synergistic effects.

4.2 Experimental

All chemicals were obtained from Sigma Aldrich unless otherwise noted and consumed without further purification.

CNFs were synthesized using the ICP system. The schematic illustration and photograph of the ICP system are demonstrated in Figure 4.1 (a) and (b),

respectively. In a standard batch of production, a 30 kW ICP system (Tekna) was used and the reactor was operated at 22 kW. Central gas was argon (99.995%) at 15 slpm flow rate. Sheath gas was sent as a mixture of hydrogen (99.995%) and argon with flow rates of 6 and 60 slpm, respectively. Nitrogen (99.99%) was chosen as the quenching gas and it was send through channels of the system at a flow rate of 150 slpm. Feeding liquid was ethanol with a flow rate of 10 ml/min. The operation time was 35 minutes and at the end of the process 500 mg powder was obtained.

On the other hand, MnO_2 nanoparticles were produced by a redox reaction between stoichiometric amounts of manganese sulfate ($MnSO_4$) and potassium permanganate ($KMnO_4$) in DI water. In a standard synthesis, 10 ml of 0.15 M $MnSO_4.H_2O$ solution was mixed with 10 ml of 0.1 M $KMnO_4$ solution and stirred continuously for 6 h. Then a dark-brown powder was obtained. This powder was washed several times with DI water and centrifuged. Finally, it was dried at 70 °C in open atmosphere for 12 hours. This method allowed the synthesis of approximately 300 mg of MnO_2 powder in each experiment [134].

After obtaining the powder components, 3 different recipes were used to fabricate the supercapacitor electrodes. For the bare CNF electrode, 90 wt.% CNF and 10 wt.% polytetrafluoroethylene (PTFE, 60 wt.% dispersion in H_2O); for the bare MnO_2 electrodes, 70 wt.% MnO_2, 20 wt.% carbon black (C-Nergy Super C65), and 10 wt.% PTFE; and for the nanocomposite CNF-MnO_2 electrode, 50 wt.% MnO_2, 20 wt.% CNF, 20 wt.% carbon black, and 10 wt.% PTFE were mixed mechanically. These mixtures were used as the pastes, thinned, and punched to obtain circular supercapacitor electrodes with diameters between 5 and 7 mm. Finally, prepared electrodes were assembled into supercapacitor devices within a Swagelok type cell and tested in 2-electrode configuration using glass microfiber filters (Whatman) as separators. The two electrodes used for the fabrication of supercapacitors were identical in terms of surface area and weight. Weight of each electrode was around 15 mg.

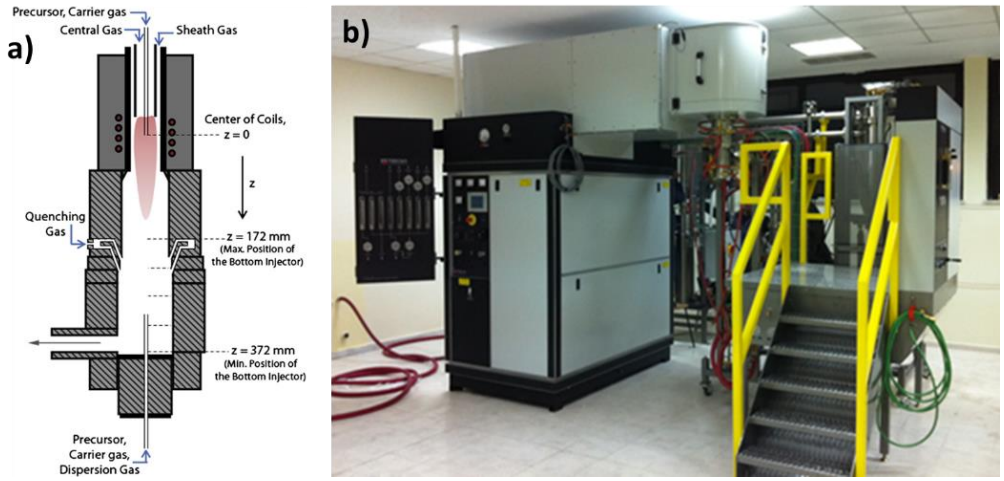

Figure 4.1. (a) The schematic illustration [128] and (b) the photograph of the ICP system used in the experiments.

The morphological and energy-dispersive X-ray spectroscopy (EDS) examination of the fabricated electrodes was conducted by SEM (FEI Nova Nano SEM 430, operated at 20 kV). Dispersive Raman analysis was carried out using a Renishaw inVia system (excitation wavelength: 532 nm) for the structural characterization of the CNFs. A Perkin Elmer 400 system was utilized for FTIR analysis. ATR mode was used during the measurements. BET surface area was determined by an Autosorb-1C/MS instrument. For the electrochemical tests of the supercapacitor electrodes a Biologic VMP3 potentiostat/galvanostat device was employed. During electrochemical tests, a 1 M KOH electrolyte was used. Electrochemical characterization of the electrodes included CV, GCD, EIS, and cyclic charge discharge measurements.

4.3 Results and Discussion

Low- and high-magnification SEM images of the synthesized CNFs are provided in Figure 4.2 (a) and (b), respectively. SEM images revealed dominant flake-like morphology of the synthesized nanoparticles and therefore the material was named as CNFs. The sizes of the flakes range from 100 to 200 nm and it is understood that they were stacked on top of each other.

Low- and high-magnification SEM images of synthesized MnO_2 nanoparticles are provided in Figure 4.2 (c) and (d), respectively. Figure 4.2 (d) points out that the diameters of the MnO_2 nanospheres are around 100 nm. This nanosphere morphology signifies the presence of α-MnO_2 structure [134].

EDS spectrum of the CNFs is given in Figure 4.2 (e). Only C and O peaks appear on the spectrum signifying the contamination-free nature of CNFs. EDS analysis of MnO_2 powders is given in Figure 4.2 (f). High intensity Mn and O peaks dominate the EDS spectra in addition to K. Following synthesis, MnO_2 was centrifuged with copious amount of water for several times; but it is evident that some K due to the use of $KMnO_4$ precursor remained within the synthesized MnO_2 powder.

XRD pattern for CNFs is given in Figure 4.3 (a). The diffractogram points out the crystalline nature of the CNFs. The peaks positioned at around 26°, 43° and 44° are the characteristic peaks of the graphitic structure. In particular, the peak around 26° is related to (002) plane, which signifies existence of graphitic layers within the nanoflakes. The peak around 43° corresponds to the (100) plane and is attributed to the hexagonal symmetry of the graphene layers [130]. XRD pattern of MnO_2 is provided in Figure 4.3 (b). Broad but evident peaks at positions of 12°, 37°, 42° and 66° signify poorly crystalline state having a short-range ordered α-crystallographic structure for synthesized MnO_2 powders (JCPDS no. 44-0141) [134].

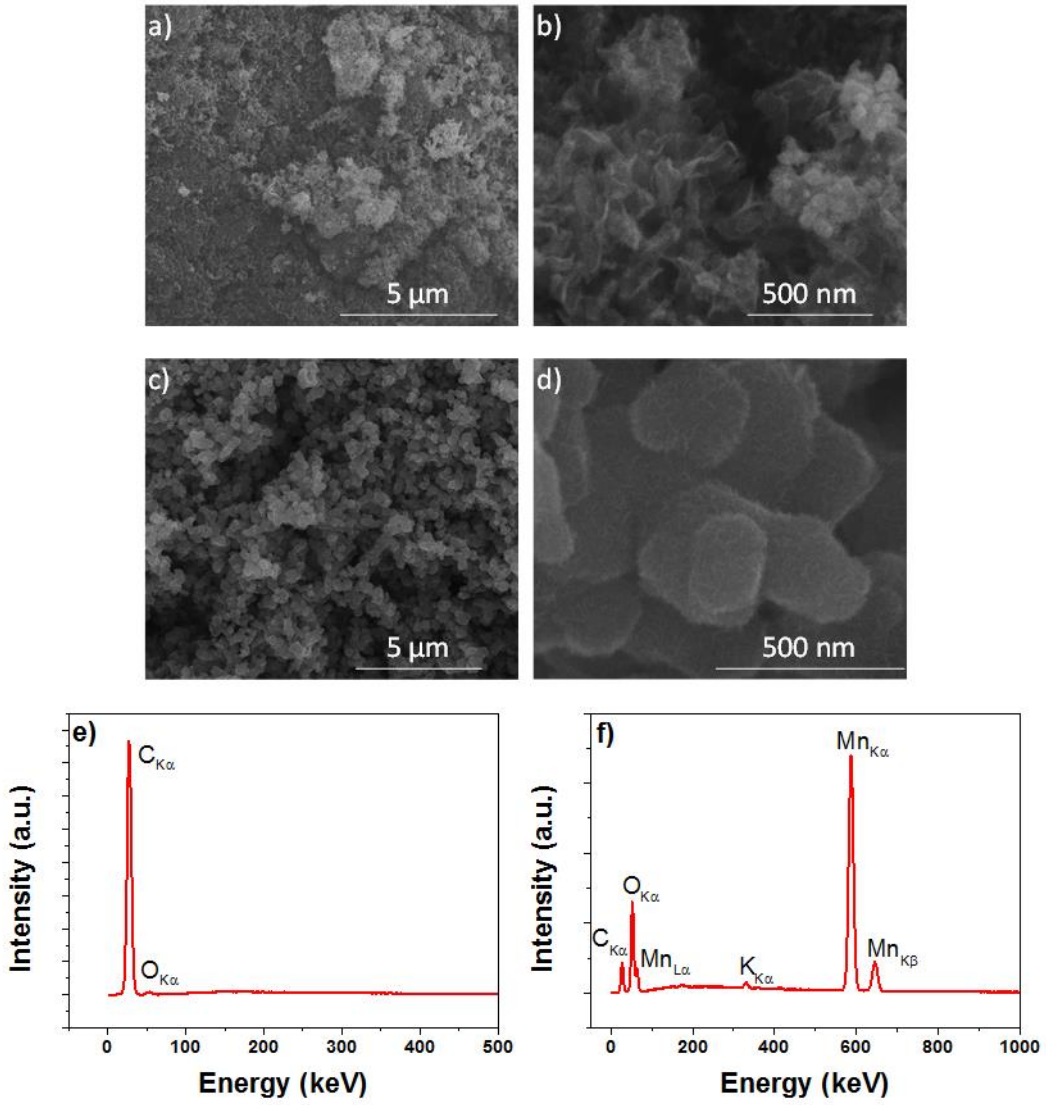

Figure 4.2. (a), (c) Low- and (b), (d) high-magnification SEM images of synthesized CNFs and MnO_2, respectively. EDS spectra of synthesized (e) CNFs and (f) MnO_2.

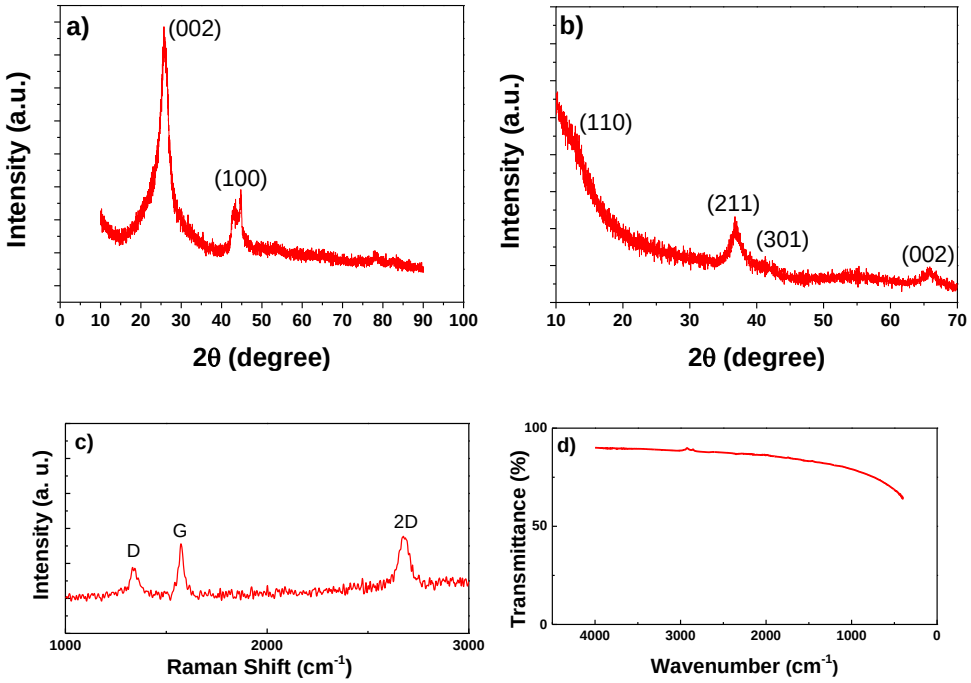

Figure 4.3. XRD patterns of synthesized (a) CNFs and (b) MnO_2. (c) Raman and (d) FTIR spectra of the synthesized CNFs.

In Figure 4.3 (c) Raman spectrum of CNFs is shown. G band at 1577 cm^{-1}, D band at 1345 cm^{-1} and 2D band at 2697 cm^{-1} are all characteristic peaks of graphitic materials in Raman analysis. The degree of graphitization for the carbonaceous materials can be monitored through determining the intensity ratio of D peak to G peak (I_D/I_G). While D band stands for the amorphous disorder in carbonaceous materials, G band represents stretching vibration of the graphitic C-C bond. Materials with an I_D/I_G ratio lower than 1 are generally accepted to have relatively high degree of graphitization. The calculated I_D/I_G ratio for the current spectrum was less than 1. FTIR spectrum of CNF is provided in Figure 4.3 (d). According to Donnet [135], the FTIR profile of pristine carbon black is relatively featureless because the graphene sheets forming carbon black, disposed in a turbostratic way, are not infrared active [136]. From this perspective, one can state that the synthesized CNFs were similar to pristine carbon black under infrared radiation. In addition to structural analysis, specific surface area of the CNFs was also measured through

BET analysis. A specific surface area of 320 m^2/g was obtained for the synthesized CNFs, which is highly competitive compared to similar materials in literature [130].

CV results for the CNF-MnO_2 nanocomposite electrode at different scan rates ranging from 2 to 400 mV/s are provided in Figure 4.4 (a). Nearly rectangular shapes of the curves at low scan rates point out the capacitive behavior of the fabricated nanocomposite electrodes. Since the tests were carried out in 2-electrode configuration, redox peaks of pseudocapacitive MnO_2 were not evident on the CV curves. The curves are nearly horizontal especially at low scan rates signifying sufficient conductivity of the nanocomposite electrodes. With increased scan rates, inherently horizontal curves shifted towards diagonal and area within the curves increased. Comparison of CV curves of the nanocomposite electrode, bare CNF electrode and bare MnO_2 electrode at a scan rate of 2 mV/s is provided in Figure 4.4 (b). As expected, CV curve for bare CNF electrode had the smallest area among others; but at the same time, had the most distinct rectangular shape compared to the other electrodes. Since MnO_2 has pseudocapacitive behavior its specific capacity is always higher than that of carbon-based materials. Thus, as expected, bare MnO_2 electrode showed high charge accumulation evidenced by its larger CV curve compared to the bare CNF electrode. Similar case was observed when bare MnO_2 and nanocomposite electrodes are compared. CV curve for bare MnO_2 electrode had a larger area because it contained higher amount of MnO_2 per gram with respect to the nanocomposite electrode.

GCD curves of nanocomposite electrodes at different current densities are provided in Figure 4.5 (a). Triangle shapes of these curves are characteristic of the supercapacitors. Instant current decrease at the top of the triangles represents the IR drop and is significant in electrodes with low conductivity. For the fabricated nanocomposite electrodes, IR drop was found to be relatively small indicating that the conductivity of the fabricated electrodes was enough for the charge transfer. Comparison of GCD curves of all prepared electrodes is given at a current density of 0.1 A/g in Figure 4.5 (b). Charge and discharge times for the bare MnO_2 electrode are quite longer than that of bare CNF electrode due to the pseudocapacitive

mechanism of MnO_2. Nanocomposite electrodes, on the other hand, had a moderate charge-discharge time between that of bare MnO_2 and CNF electrodes.

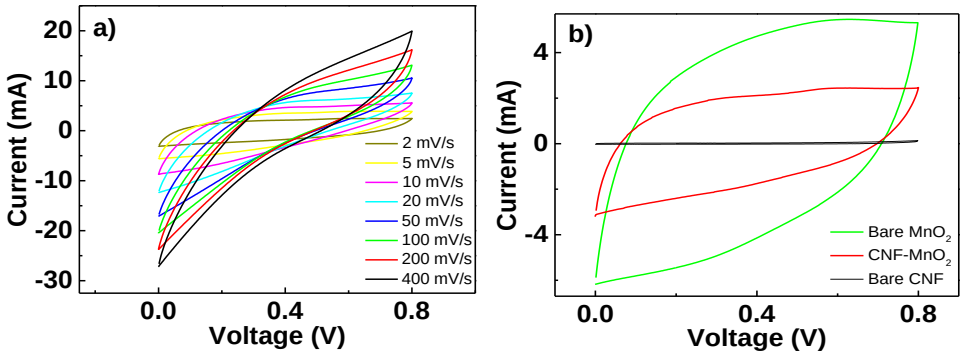

Figure 4.4. (a) CV curves of CNF-MnO_2 nanocomposite electrode at different scan rates and (b) comparison of CV curves of bare CNF, bare MnO_2 and CNF-MnO_2 nanocomposite electrodes at a scan rate of 2 mV/s.

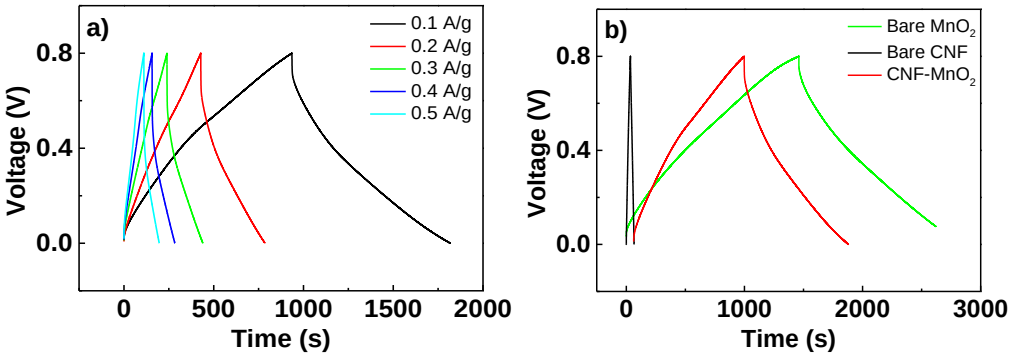

Figure 4.5. (a) GCD curves of CNF-MnO_2 nanocomposite electrode at different current densities and (b) comparison of GCD curves of bare CNF, bare MnO_2 and CNF-MnO_2 nanocomposite electrodes at a current density of 0.1 A/g.

In supercapacitors, the ratio between the discharge and the charge time is named as the Coulombic efficiency (CE). This concept is very critical for the determination of supercapacitor performance, especially in terms of cyclic life. In Figure 4.6 (a) CEs of 3 different electrodes are shown with respect to the current density. At all current densities, bare CNF electrode had higher CE values compared to bare MnO_2 electrode. This case is accepted as normal because carbonaceous

materials have higher CEs due to their EDLC mechanism. The fabricated nanocomposite electrode had the lowest CE especially at high current densities in contrast to what is expected. But interestingly at a current density of 0.1 A/g nanocomposite electrode had the highest CE of 94.2%. This case was ascribed to the synergistic effect through the combination of EDLC and pseudocapacitive behaviors at that current density.

Since 2-electrode configuration was employed for the electrochemical tests, C_{sp} values of the electrodes were determined using the following equation.

$$C_{sp} = 4\frac{I}{m_t \frac{\Delta V}{\Delta t}} \quad (4.1)$$

,where I (A) is the discharge current, m_t (g) is the total mass of the active material in both electrodes, V (V) is the discharge potential and t (s) is the time of discharge step. In Figure 4.6 (b) C_{sp} values of the electrodes are provided with respect to the current densities. For all fabricated electrodes, C_{sp} values were observed to diminish with the increasing current density. On the other hand, bare CNF electrodes had very low C_{sp} values compared to the other electrodes. This case is again an inherent result due to the difference between EDLC and pseudocapacitive mechanisms. In addition, since the mass of MnO_2 in bare MnO_2 electrode was more than that within the nanocomposite electrode, C_{sp} value for the bare MnO_2 electrode was also higher than the fabricated nanocomposite electrode. Obtained C_{sp} values were 7.72, 289.75 and 220.38 F/g for bare CNF, bare MnO_2 and CNF-MnO_2 nanocomposite electrodes, respectively, at a current density of 0.1 A/g.

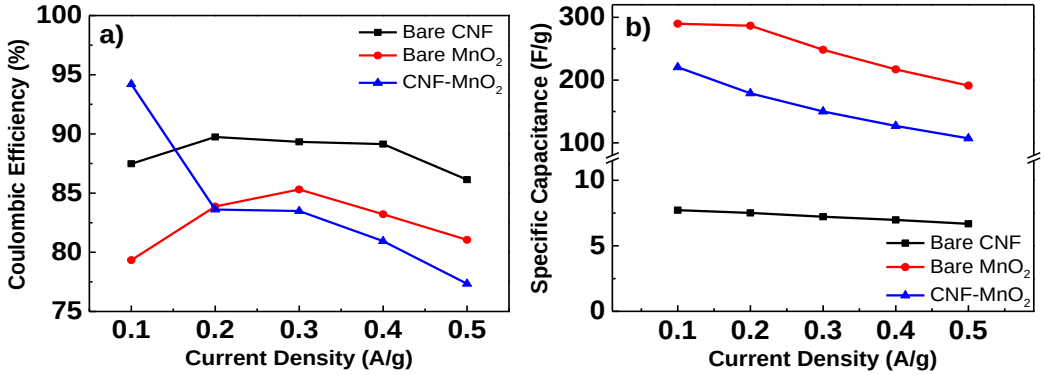

Figure 4.6. Change in (a) Coulombic efficiency and (b) specific capacitance with respect to current density for the fabricated electrodes. Lines are for visual aid.

EIS results of all fabricated electrodes are provided in Figure 4.7 (a). Low frequency region of the EIS curves is provided as the inset in the figure. EIS tests were conducted with an AC perturbation of 5 mV and within a frequency range of 100 kHz to 10 mHz. In high frequency region, the minimum intercept point of a curve with X-axis corresponds to the series resistance, while the diameter of the semi-circle represents the charge transfer resistance. In the light of this information, as expected, bare CNF electrode showed minimum series and charge transfer resistances of 0.8 Ω and 1.92 Ω, respectively. On the contrary, bare MnO_2 electrode had the highest series and charge transfer resistances as 2.4 Ω and 6.55 Ω, respectively. This case arises from the nature of carbonaceous and oxide-based materials. CNF-MnO_2 nanocomposite electrode had a similar series resistance to that of bare CNF electrode as 0.92 Ω. In addition, it was obvious that the addition of CNFs improved the charge transfer mechanism of MnO_2 and the resistance of the electrode decreased to 4.16 Ω.

Fabricated electrodes were subjected to 1,000 charge-discharge cycles at a current density of 0.5 A/g. The results of these capacitance retention tests are provided in Figure 4.7 (b). As expected, bare CNF electrode showed the highest cyclic performance among the other electrodes because its capacitance mechanism is based purely on EDLC. Bare CNF electrode conserved 87.3% of its initial capacitance. This value decreased to 54.6% when it comes to bare MnO_2 electrode.

The reason of this decrease is the pseudocapacitive nature of the MnO_2. Fast redox reactions harm the bare MnO_2 electrode notably during 1,000 cycles of charge and discharge. But following the addition CNFs and formation of the nanocomposite electrode, cyclic performance of the electrodes improved significantly. CNF-MnO_2 nanocomposite electrode conserved 67.2% of its initial capacitance.

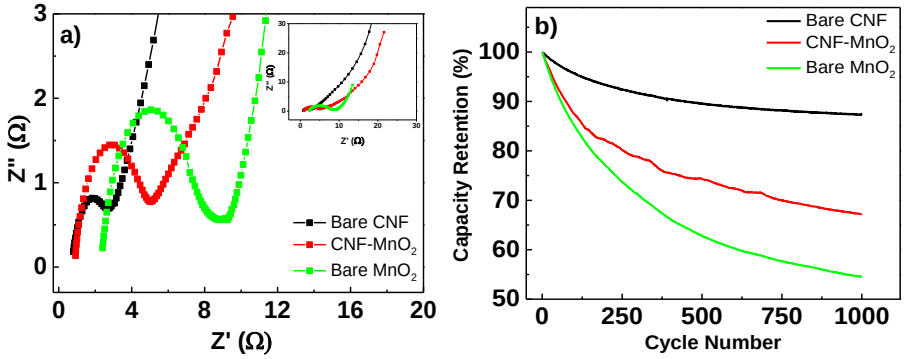

Figure 4.7. (a) Nyquist plot and (b) capacitance retention plot for the fabricated electrodes. Inset shows the high frequency region of the Nyquist plot.

CNFs produced through ICP method is highly promising for electrochemical energy storage primarily because of the significant synthesis yield and remarkably low cost. Although some slight improvements are demonstrated via fabricated nanocomposites in this work, there exists a lot of room to improve the electrochemical characteristics of CNFs, through functionalization, pore formation and in-situ decoration with pseudocapacitive materials.

4.4 Conclusions

In this work, CNF-MnO_2 nanocomposite supercapacitor electrodes were fabricated. CNFs were synthesized using ethanol as the precursor in the ICP system. CE and capacitance retention values of the nanocomposite electrodes were found to improve compared to the bare MnO_2 electrode. The improvements were 23% and 18% for CE and capacitance retention, respectively, upon the formation of nanocomposite electrodes. As shown in this work, synthesis of CNFs by ICP system

is very practical and has a potential for mass production. This point shows that the CNFs synthesized by ICP system is highly promising for supercapacitor electrodes and can be used directly or as an additive to other active materials not only in supercapacitor but also in battery electrodes.

CHAPTER 5

REDUCED GRAPHENE OXIDE AEROGEL - MOLYBDENUM DISULFIDE SUPERCAPACITOR ELECTRODES ON NICKEL FOAMS

5.1 Introduction

Chemical oxidation-exfoliation-reduction of graphite powder is an effective technique for the synthesis of graphene materials, along with its derivatives such as graphene oxide (GO) and reduced GO (rGO). This inexpensive wet chemical method has some advantages, such as high yield using cheap graphite powders, adaptability and scalability for industrial production, simplicity in adjusting the specifications of graphene materials, and suitability of producing graphene composites. The most commonly used technique for synthesizing GO is chemical oxidation of graphite powder into graphite oxide using strong oxidants and concentrated acids, followed by mechanical exfoliation. Graphite oxide can be simply exfoliated into GO flakes by dilution or sonication to obtain a stable dispersion in water. rGO aerogels are types of popular monolithic carbonaceous materials with 3D micro and nanoarchitectures. Aerogels of rGO and their composites are usually obtained from their hydrogel precursors using freeze drying, which is a wet shaping method for porous materials, in order to substitute water stuck in the network with air. GO and rGO hydrogels can be synthesized via the routes shown in Figure 5.1 [137].

rGO based gels have been used extensively to fabricate the supercapacitor electrodes, showing notable performances. Xu et al. [138] developed a supercapacitor based on rGO gel and it delivered a high specific gravimetric capacitance of 152 F/g which is approximately 50% higher than that based on agglomerates of rGO (100 F/g) [137].

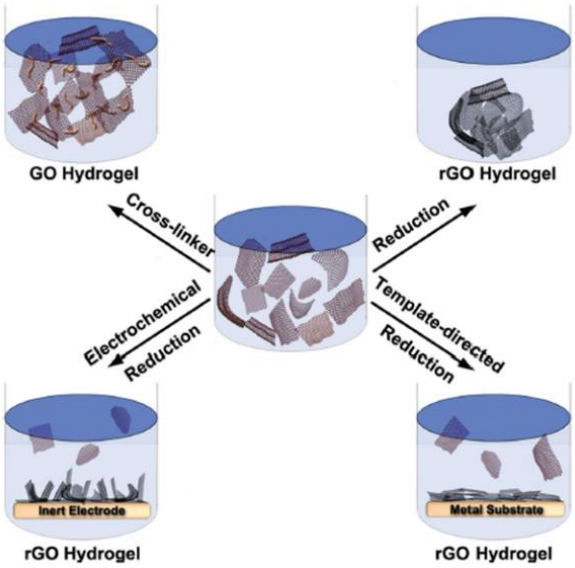

Figure 5.1. Production routes of GO and rGO hydrogels [137].

After the discovery of superior properties of graphene, in recent years other 2D inorganic nanomaterials, especially mono- and multi-layered nanosheets of layered transition metal dichalcogenides (TMDs), such as molybdenum disulfide (MoS_2), titanium disulfide (TiS_2), tungsten diselenide (WSe_2), and etc., received significant attention. Up to now, different techniques have been proposed for the production of single- or few-layer TMD nanosheets, such as CVD, mechanical cleavage technique and intercalation/exfoliation processes (Figure 5.2 (a)). These 2D nanomaterials that are electronically and chemically active showed promising performances in electrocatalysis, opto-electronic/electronic devices, sensors and energy storage applications [139].

MoS_2, has a very similar layered structure to 2D graphene. Research on MoS_2 for utilization in electrochemical energy storage has been going on for a long time. MoS_2 has a 2H phase crystal structure with a monolayer bandgap of about 1.9 eV. Therefore, it has semi-insulating behavior and not preferred as an electrode material for energy storage applications directly. On the other hand, 1T phase of MoS_2 which can be synthesized from 2H phase has 10^7 times higher conductivity than that of semiconducting 2H phase. In addition, it is significantly hydrophilic [140]. The

phase transition from 2H to 1T changes the density of states, resulting in MoS_2 transforming from the semiconducting to metallic phase. Nevertheless, 1T phase is not stable and transforms back to the 2H phase upon annealing at around 300 °C. Both the 1T and 2H phase of MoS_2 may exist in single-layer nanosheets form. Since the two phases with different electronic properties are lattice matched, they form electronic and atomic heterostructures that are chemically homogeneous [141]. Crystal structures of 2H and 1T phases of MoS_2 are schematically illustrated in Figure 5.2 (b).

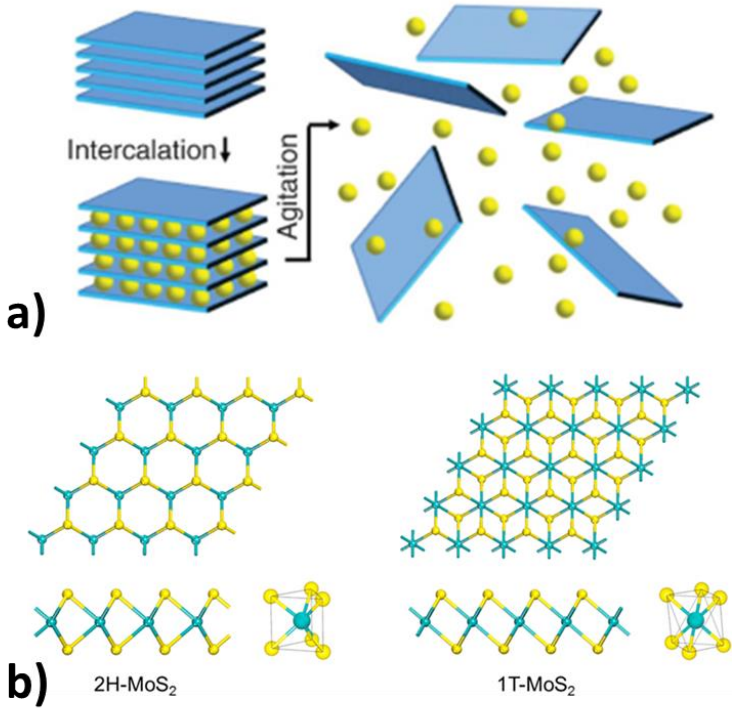

Figure 5.2. Schematic illustration of (a) exfoliation process [142] and (b) crystal structure of 2H and 1T phases of MoS_2 [143] (Mo: Cyan, S: Yellow).

In this work, rGO-MoS_2 nanocomposite electrodes were prepared on nickel foam. These nanocomposite supercapacitors were tested using different electrochemical techniques and the results were compared with a control device consisting of bare rGO electrodes.

5.2 Experimental

GO was synthesized via Tour method [144]. This method was preferred since it is simple and allows high-yield synthesis without release of poisonous gases. Firstly, 3 g graphite and 18 g $KMnO_4$ were mixed. Onto this powder mixture, 400 ml H_2SO_4 and phosphoric acid (H_3PO_4) acid mixture with a ratio of 9:1 was added. Then powder and acid mixture was stirred for 12 hours at 50 °C. After reaching RT the mixture was poured into an ice bath prepared using 400 ml water. The reaction was finalized adding hydrogen peroxide (H_2O_2, 30%). Lastly, acidic components were separated via centrifuge and GO was purified using hydrochloric acid (HCl, 3.4%) and acetone. GO hydrogels were obtained solvothermally from GO dispersions. Then the hydrogels were freeze-dried using a Labconco FreeZone 2.5 freeze dryer and thermally reduced to obtain rGO aerogel [145]. The diagram of rGO aerogel production is given in Figure 5.3.

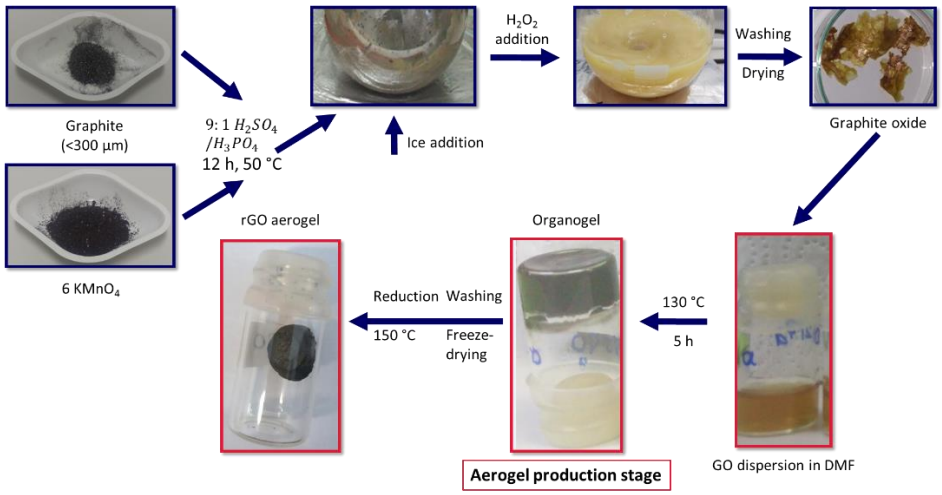

Figure 5.3. Schematic diagram for rGO aerogel production.

Exfoliation of MoS_2 was achieved through Li intercalation as shown schematically in Figure 5.4. In the beginning of the procedure, 0.25 g MoS_2 powder (Sigma-Aldrich, 98%) and 10 ml n-Butyllithium in hexane (Sigma-Aldrich, 1.6 M) was placed in a bottle inside an argon filled glove-box (0.6 ppm H_2O, 14.5 ppm O_2, 4.8 mbar pressure). These precursors were mixed for 48 hours at 80 °C. After mixing,

the solution was washed with hexane by 3 consecutive centrifuge processes. Then the intercalated powder was exfoliated in water by sonication for 1 hour. Final solution was centrifuged 3 times and the exfoliated MoS_2 powder was collected upon drying in a vacuum oven.

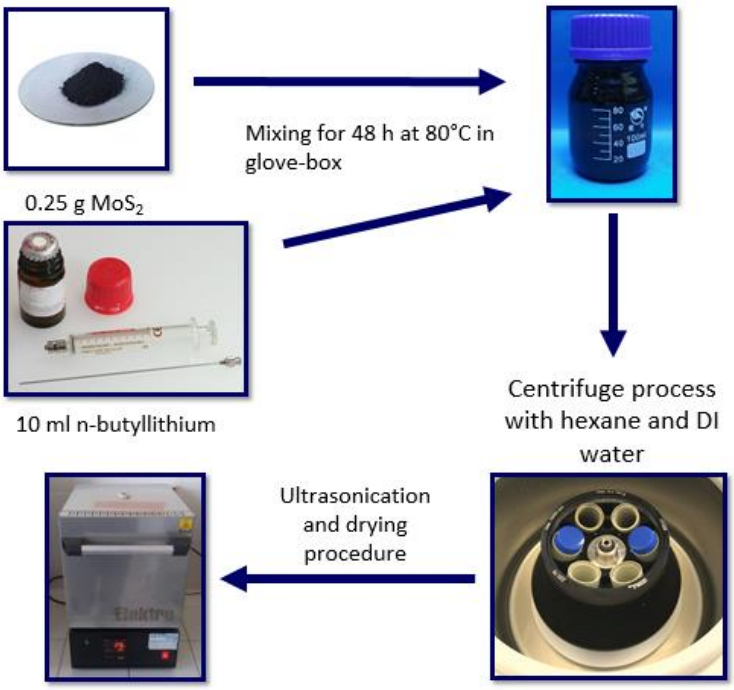

Figure 5.4. Photos showing the MoS_2 exfoliation procedure.

For the fabrication of nanocomposite supercapacitor electrodes, firstly rGO aerogel was pressed on a nickel foam substrate (rGO@nickel foam). After that an exfoliated MoS_2 dispersion in ethanol was simply drop-casted onto rGO@nickel foams. Finally, excess ethanol was evaporated using a hot plate and a symmetric device was assembled using the produced rGO-MoS_2 electrodes. Diagram of rGO-MoS_2 electrode preparation is shown in Figure 5.5. Electrochemical measurements of the fabricated electrodes were carried out through CV, GCD, and EIS tests in a potentiostat/galvanostat system (Biologic VMP3). Two-electrode configuration was set up in a Swagelok cell for the measurements. Results of the tests were compared to that of rGO@nickel foam control samples. 6 M KOH solution was selected as the electrolyte for the measurements.

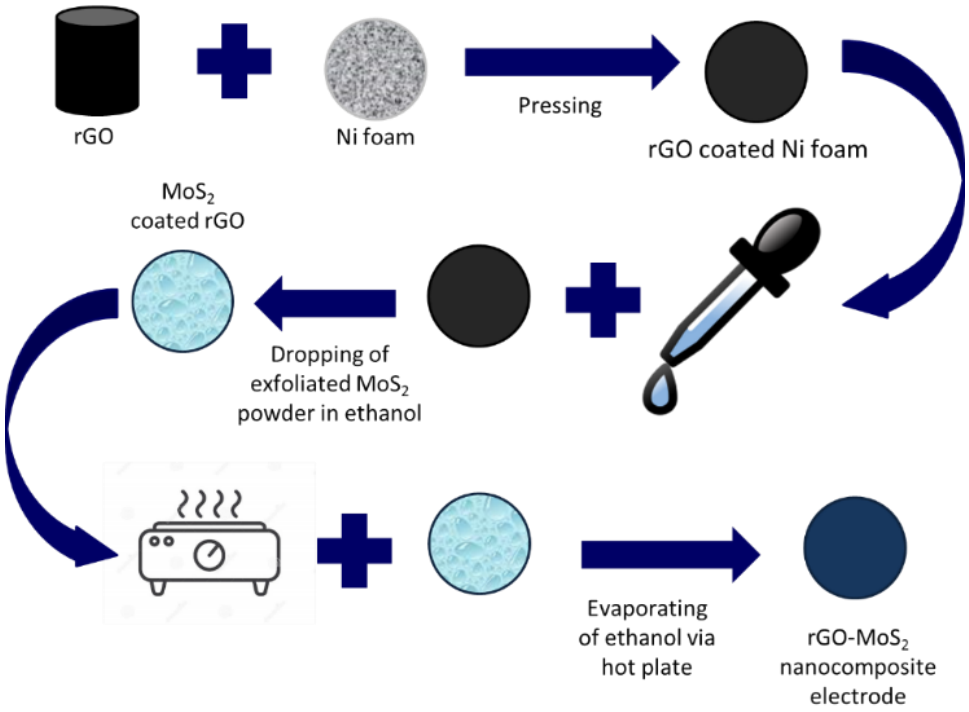

Figure 5.5. Schematic diagram showing the preparation of rGO-MoS_2 nanocomposite supercapacitor electrodes.

5.3 Results and Discussion

SEM images of GO, rGO and pressed rGO aerogels are provided in Figure 5.6 (a), (b) and (c), respectively. In all images well-separated GO and rGO flakes can be seen clearly. Following reduction reaction, it is clear that there are no significant morphological changes when Figure 5.6 (a) and (b) are compared. As seen in Figure 5.6 (c) after pressing, no deformation effects were observed in the rGO@nickel foam and it is concluded that rGO samples retained their morphology upon pressing.

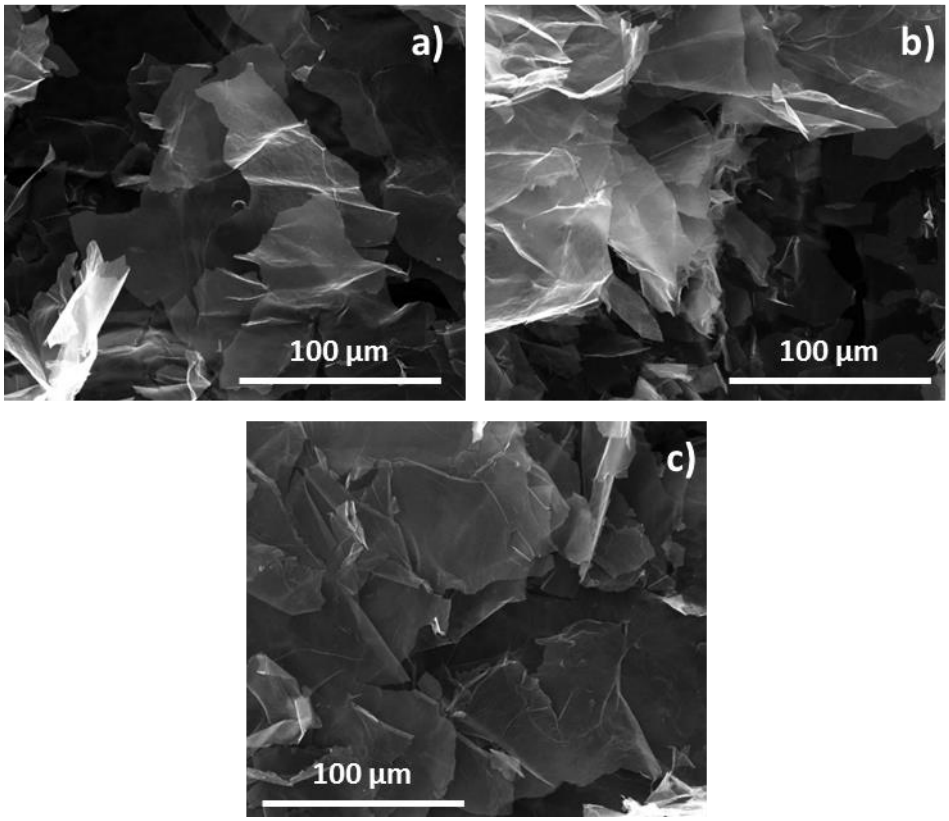

Figure 5.6. SEM images of (a) GO, (b) rGO and (c) pressed rGO aerogels.

On the other hand, SEM images of pristine MoS_2 (p-MoS_2) and exfoliated MoS_2 (e-MoS_2) are provided in Figure 5.7 (a) and (b), respectively. p-MoS_2 powder was very coarse but one can clearly see the e-MoS_2 sheets in Figure 5.7 (b). These morphological modifications are clear signs of successful exfoliation processes for MoS_2.

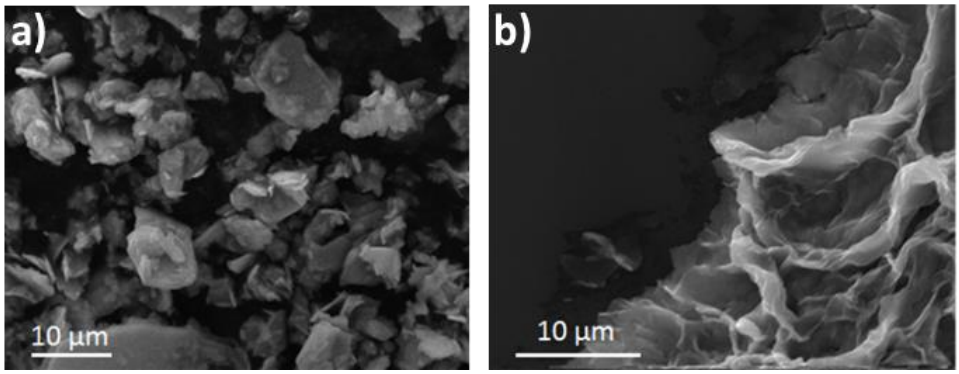

Figure 5.7. SEM images of (a) p-MoS_2 and (b) e-MoS_2.

Characteristic (001) peak of synthesized GO (JCPDS no. 75-2078) was observed at 5° in XRD analysis of the sample (Figure 5.8 (a)). No extra peak was observed in the XRD pattern indicating that the GO was free of contamination and residues within the detection limit of XRD. Diagnosis of D band and G band for carbonaceous materials in Raman analysis is critical in terms of the existence of the graphene structures (see Section 2.3, Figure 2.7). Both D and G bands are clearly seen for GO and rGO aerogel samples (Figure 5.8 (b)).

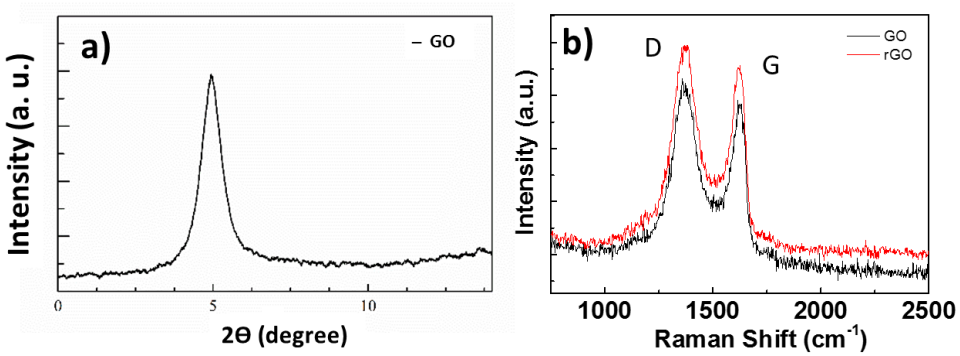

Figure 5.8. (a) XRD pattern of GO and (b) Raman spectra of GO and rGO aerogels.

Figure 5.9 (a) shows the XRD patterns of the pristine and exfoliated MoS_2. The (002) peak of MoS_2 is known to correspond to the interplanar spacing between the nanosheets. The broadness of the (002) peak points out that the nanosheets are randomly distributed with large spacing between the layers. In Figure 5.9 (b), Raman spectra of the p-MoS_2 and e-MoS_2 are shown. The intensity of E^1_{2g} was low in the spectrum of e-MoS_2 and this was attributed to the presence of 1T MoS_2 sheets and a successful exfoliation [140].

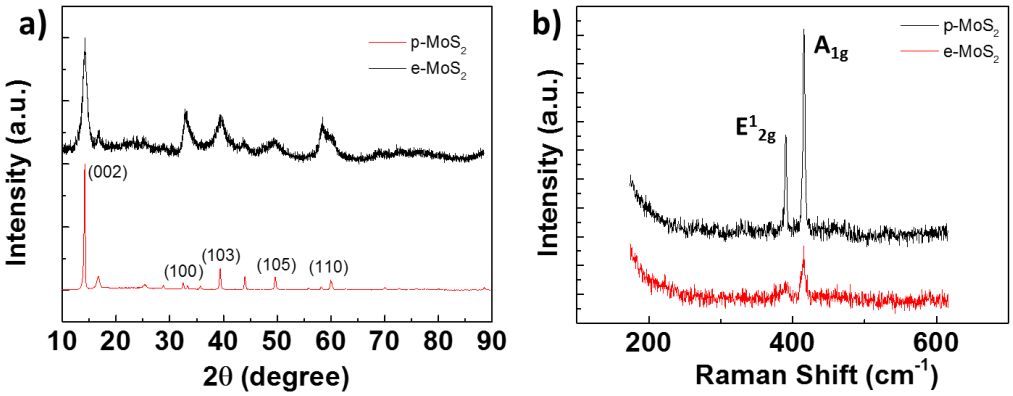

Figure 5.9. (a) XRD pattern and (b) Raman spectra of p-MoS_2 and e-MoS_2.

Figure 5.10 (a) and (b) demonstrate XPS survey spectra and spectra of C for GO, respectively. In the survey spectra, only C peak at 285 eV and O peak at 531 eV were observed as seen in Figure 5.10 (a). Upon deconvolution of C peak, C=C, C-O, C=O, and O=C-OH bonds, which are associated with the GO were identified as shown in Figure 5.10 (b) [146].

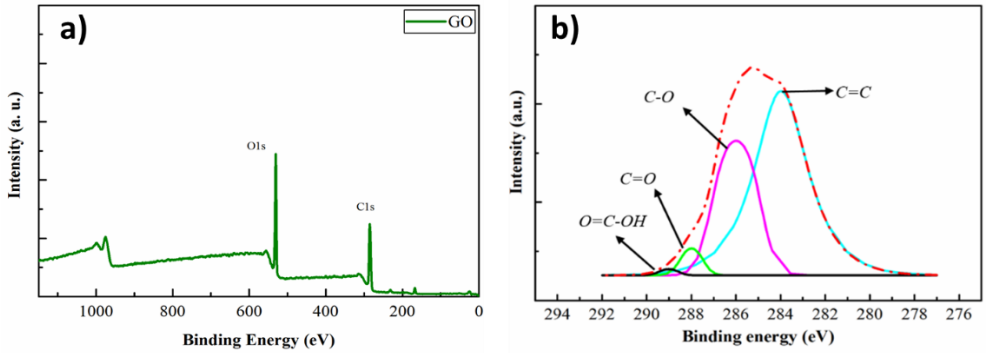

Figure 5.10. XPS (a) survey spectra and (b) spectra of C of GO.

In Figure 5.11 (a) and (b) rGO-MoS_2 nanocomposite electrode and bare rGO@nickel foam electrode are compared in terms of their CV performances at 25 and 400 mV/s, respectively. Area of the CV curve in nanocomposite electrode is larger than that of bare rGO@nickel foam meaning that specific capacitance of rGO-MoS_2 electrode is higher than that of bare rGO@nickel foam electrode. The difference between the electrodes became more evident when the scan rate was increased to 400 from 25 mV/s.

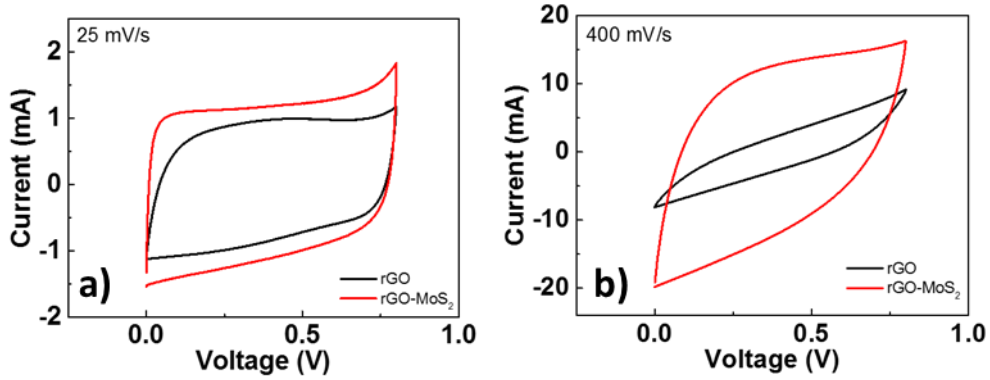

Figure 5.11. CV curves of bare rGO@nickel foam and rGO-MoS_2 nanocomposite electrodes at scan rates of (a) 25 mV/s and (b) 400 mV/s.

In order to determine the rate capabilities, CV curves of bare rGO@nickel foam and rGO-MoS_2 nanocomposite electrodes are provided at different scan rates in Figure 5.12 (a) and (b), respectively. Quasi-rectangular shapes of the CV curves which is a well-known characteristic of supercapacitors are quite clear for both samples at lower scan rates. At higher scan rates, although bare rGO@nickel foam electrode deflected from ideal substantially (Figure 5.12 (a)), rGO-MoS_2 nanocomposite electrode significantly retained its CV shape (Figure 5.12 (b)).

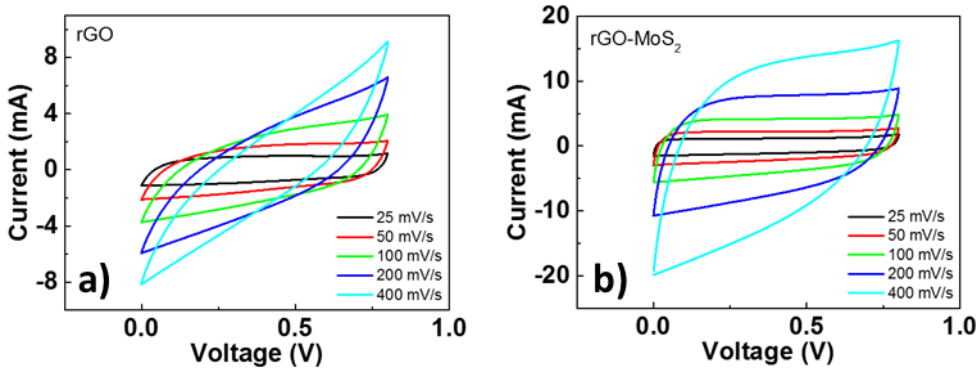

Figure 5.12. CV curves of (a) bare rGO@nickel foam and (b) rGO-MoS_2 nanocomposite electrodes at different scan rates.

Results of the GCD tests are shown in Figure 5.13 for both samples at different current densities. Highly symmetric and plateau-free, triangle-like GCD curves pointing out capacitive behavior were obtained. A small IR drop, can be observed in Figure 5.13 (a). When it comes to rGO-MoS_2 nanocomposite, much lower IR drop was observed than that of bare rGO@nickel foam as shown in Figure 5.13 (b).

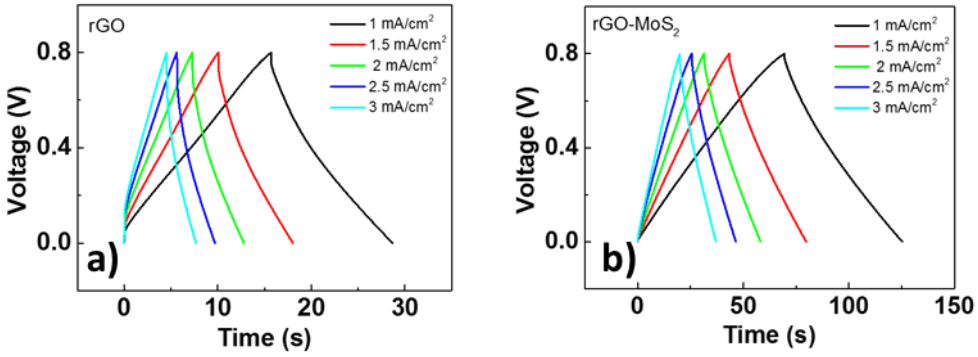

Figure 5.13. GCD curves of (a) bare rGO@nickel foam and (b) rGO-MoS_2 nanocomposite electrodes at different current densities.

As seen in Figure 5.14 (a), discharge time of nanocomposite electrode is longer than that of bare rGO@nickel foam electrode. This means that nanocomposite electrode had higher specific capacitance. Equation 2.1 is used to calculate the specific capacitance values. While 67.5 mF/cm^2 specific capacitance was calculated for nanocomposite electrode, bare rGO@nickel foam electrode had a specific capacitance of 42.5 mF/cm^2. Coulombic efficiency values of the samples are provided in Figure 5.14 (b). Nanocomposite electrode showed higher Coulombic efficiencies at each current density than bare rGO@nickel foam electrode. A maximum Coulombic efficiency of 87% was recorded at a current density of 2 mA/cm^2.

As expected C_{sp} values of both samples decreased with increasing current density as shown in Figure 5.15 (a). In the same interval the Coulombic efficiency of rGO-MoS_2 electrode remained higher than 55%. After 3,000 charge-discharge

cycles, bare rGO@nickel foam electrode conserved 67% of its initial capacitance as shown in Figure 5.15 (b). This value was 81% for nanocomposite electrode. It is clear that the MoS_2 addition increases the capacitance retention of the device. This is attributed to the thin layer of MoS_2 on rGO. MoS_2 coating improves the attachment of rGO to the Ni foam and protects it form external effects such as exposure to electrolyte for prolonged times. Thus, nanocomposite electrode was able to retain much of its capacitance without losing its initial form.

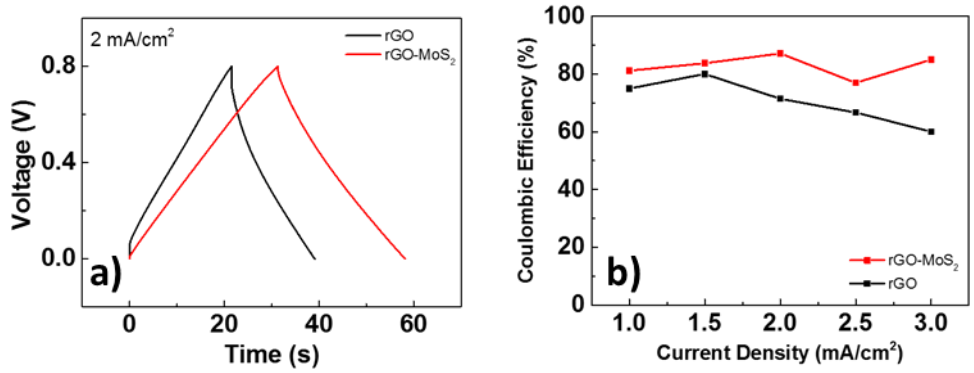

Figure 5.14. (a) Comparison of GCD curves and (b) Coulombic efficiency values of bare rGO@nickel foam and rGO-MoS_2 nanocomposite electrodes.

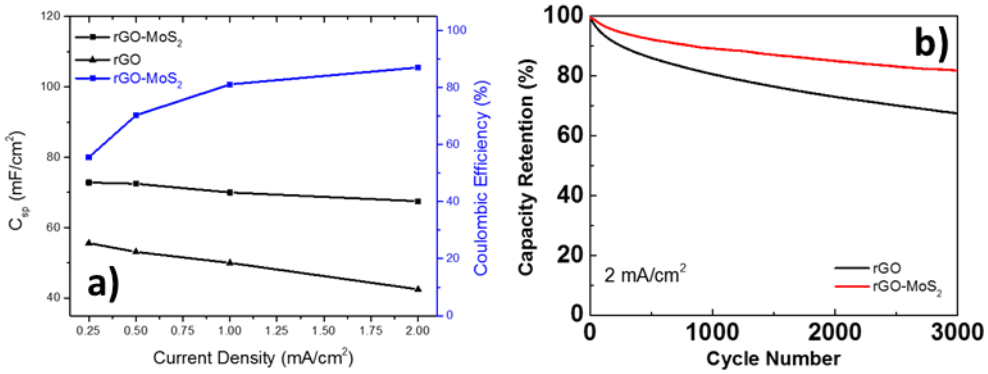

Figure 5.15. (a) C_{sp} values of the bare rGO@nickel foam and rGO-MoS_2 nanocomposite electrode and related Coulombic efficiencies of rGO-MoS_2 electrode with respect to current density and (b) capacitance retention performance of the samples.

EIS measurements were carried out between 100 kHz and 10 mHz frequency and the results are provided in Figure 5.16. Both electrodes showed a nearly vertical line in the low frequency region, which is a supercapacitor behavior as seen in Figure 5.16 (a). As seen in the inset of Figure 5.16 (a), series resistances of both electrodes were determined as nearly the same. Nanocomposite electrode had less charge transfer resistance than bare rGO@nickel foam electrode as demonstrated in Figure 5.16 (b). Therefore, it is concluded that addition of MoS_2 improves the charge transfer efficiency within the electrode. This enhancement is attributed to the filling the pores of rGO by MoS_2 upon drop-casting. Charges are able to find more routes in the electrodes to complete the circuit, thanks to MoS_2 infiltration into the pores of rGO. This case is also considered the reason of the higher Coulombic efficiency of the nanocomposite electrode compared to bare rGO@nickel foam electrode.

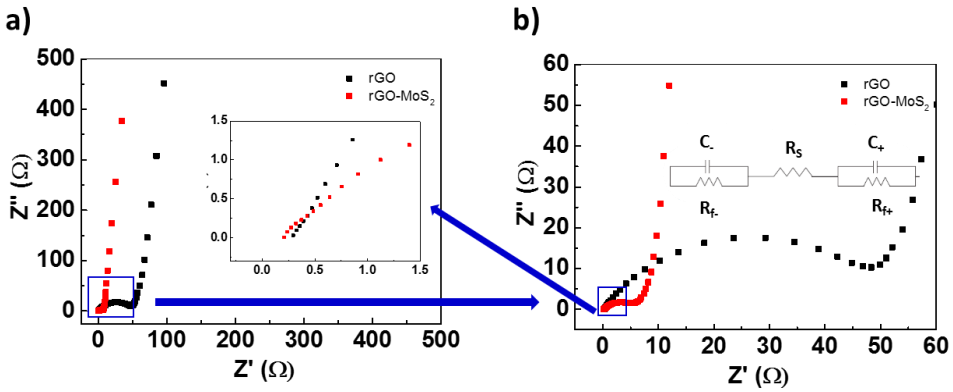

Figure 5.16. (a) Low frequency and (b) high frequency region of EIS results. Inset of (a) demonstrates very high frequency region. EIS model is provided within (b).

Similar to De Levie's [147] explanation to define the distribution of capacitance in porous materials as parallel resistor-capacitor (RC) circuits, for description of the basic operation of a supercapacitor, a simplified RC equivalent circuit model can be considered. An adapted form of this model to the symmetric cells is schematically illustrated in inset of Figure 5.16 (b) for the current study. On the schematic, $R_{f-/+}$ and $C_{-/+}$ stand for the faradic resistance and capacitance for the negative and positive electrodes, respectively. R_S represents the ESR of the device [2].

5.4 Conclusions

A practical method for the fabrication of rGO-MoS_2 nanocomposite supercapacitor electrodes was developed. Nanocomposite electrodes showed higher Coulombic efficiencies compared to the bare rGO@nickel foam electrode for all the applied currents. Following nanocomposite formation, cyclic life of the electrodes increased from 67% to 81%. Specific capacitance of the rGO-MoS_2 nanocomposite electrodes was 67.5 mF/cm^2 at 2 mA/cm^2 in 6 M KOH electrolyte, which was approximately 60% higher than that of bare rGO@nickel foam electrode.

CHAPTER 6

2D HEXAGONAL BORON NITRIDE - MOLYBDENUM DISULFIDE NANOCOMPOSITE SUPERCAPACITOR ELECTRODES

6.1 Introduction

In recent years, 2D hexagonal boron nitride (h-BN) nanosheets received significant attention. They are electrically insulating, have ultra-flat surface and quite stable structures (Figure 6.1). h-BN can well be modified to impart additional functionalities by several methods, such as hybridization, substitution, and doping. In addition, it can be utilized to adjust the carrier mobility level of other 2D materials, such as graphene, MoS_2, and black phosphorus. Driven by the predicted potential, few and single-layer h-BN nanosheets have been successfully obtained and examined. In fact, they have been used showing promising performances in various applications involving photonic and power devices, electronic packaging, fuel cells, and biomedicine [148].

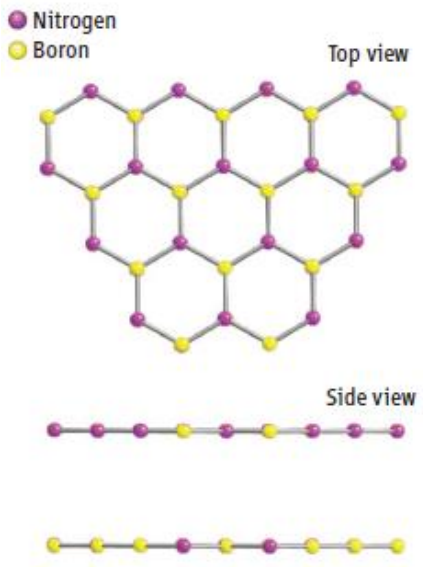

Figure 6.1. Schematic illustration of molecular structure of h-BN [142].

Supercapacitors bridge the gap between rechargeable batteries and electrolytic capacitors. In supercapacitors, collected charges heavily depend on the specific surface area of the electrode materials. Charges are deposited at the interface between the electrolyte solution and the surface of electrodes. 2D materials are very important as supercapacitor components because of their high specific surface area. In the past decade, several techniques have been proposed to exfoliate layered materials to obtain monolayer nanostructures. These exfoliation techniques form significantly high-aspect ratio nanosheets with very high specific surface area. These are desired for applications in which surface activity is crucial. h-BN can also be exfoliated by sonication in surfactant solutions, solvents, or polymeric solutions to produce 2D h-BN nanosheets [142]. In addition to nanosheets, h-BN can be synthesized as nanoparticles, tubes and fibers and the specific surface area of these materials vary from 140 to 900 m^2/g [149,150].

Pristine h-BN is utilized in variety of applications in high-temperature devices. In addition, it is used as a substrate for the synthesis of other 2D materials. Nevertheless, it has electrically insulating nature in its pristine form and this restricts its usage in electrochemistry and in other electronic applications to separators and heat spreaders. Modification of the band gap can alternate the characteristics of h-BN for aforementioned applications. For this purpose, graphene can be used to prepare a composite and it can change the band gap of h-BN. The B−N bond length is approximately 1.7% longer than that in C−C bond and therefore minimal internal stress is anticipated when graphene is mixed with the h-BN. Thus, graphene and h-BN are suitable for combining in heterostructures. The enhanced electrical conductivity and the hierarchical structure of graphene/h-BN nanocomposites are already utilized in energy storage devices, while the use of bare h-BN is limited to conventional dielectric capacitors. A simple and single-step hydrothermal technique was described by Saha et al. [151] for the fabrication of h-BN/reduced graphene oxide (rGO) hybrid nanocomposites. The presence of rGO enhanced electrical conductivity of h-BN and presented better ion exchange with the electrolyte by reducing the ionic resistance and also the charge-transfer resistance. A high specific

capacitance of around 824 F/g was obtained at a current density of 4 A/g for this nanocomposite in three-electrode configuration. In 6 M aqueous KOH electrolyte, the potential window of the supercapacitor electrode was in between −0.1 and 0.5 V. The working voltage was raised to 1.4 V in asymmetric devices, in which a rGO was utilized as the negative electrode and the h-BN/rGO composite was the positive electrode. The device showed a specific capacitance of 146 F/g at a current density of 6 A/g. In another study, Khan et al. [152] fabricated surfactant-exfoliated 2D h-BN nanosheets using sodium cholate which were then immobilized onto graphite electrodes using screen printing. Electrochemical properties of this composite was evaluated using 0.1 M H_2SO_4 electrolyte in a two-electrode system and a specific capacitance of 189 F/g was reported.

In order to alternate the band gap of h-BN, MoS_2 with its very similar properties to graphene can be used as an alternative support material [153]. Nanocomposite materials composed of MoS_2 and h-BN were investigated for various applications [154–157]. Wang et al. [158] reported a direct CVD technique for the production of high-quality monolayer h-BN/MoS_2vertical heterostructured films and it was concluded that there is a notable interaction between the MoS_2 and underlying h-BN.

In this work, 2D h-BN/MoS_2 nanocomposite electrodes were produced using solution-based synthesis methods and their electrochemical performances were examined carefully. Before the fabrication of the electrodes, both MoS_2 and h-BN were chemically exfoliated. Electrochemical characteristics such as specific capacitance and capacitance retention of the produced nanocomposite electrodes were investigated via CV, chronopotentiometry and EIS in a two-electrode cell. Experimental results were compared to that of the control sample prepared from bare 1T MoS_2 nanosheets.

6.2 Experimental

In order to prepare h-BN/MoS_2 nanocomposite supercapacitor electrodes both materials were first exfoliated. The exfoliation process of h-BN, schematically shown in Figure 6.2, was started through mixing 0.2 g h-BN (Nanografi, Turkey, 99.7%) and 4 g urea (Sigma-Aldrich, 99%) with an urea/h-BN ratio of 20. The mixture was placed in a stainless-steel ball mill container including 10 mm-diameter 10 stainless-steel balls. Ball milling was carried out for 5 hours at 200 rpm. After ball milling, product powder was collected and dispersed in DI water. This solution was rinsed with DI water by several centrifuge steps until the final solution had a pH of 7. Finally, exfoliated h-BN was dispersed in DI water for further tests and analysis. The exfoliation procedure of MoS_2 is mentioned in Section 5.2.

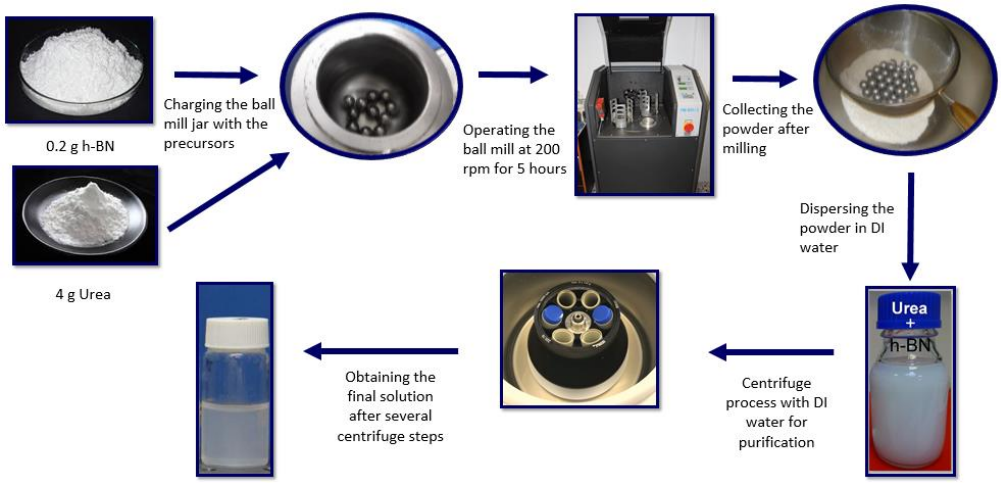

Figure 6.2. Photos showing the h-BN exfoliation procedure.

Electrode preparation procedure is schematically shown in Figure 6.3. First, 70 wt.% MoS_2, 10 wt.% carbon black (C-Nergy Super C65), 10 wt.% PTFE (Sigma-Aldrich, 60 wt. % dispersion in H_2O), and 10 wt.% h-BN were mixed in isopropanol. In control sample, instead of h-BN, 80 wt.% MoS_2 was used. The weights of the electrodes were measured as 6.3 mg. After mixing, the excess isopropanol was evaporated and an electrode dough was obtained. Thinned electrode dough was punched with a diameter of 7 mm. The weights of the punched electrodes were

measured and symmetric supercapacitor devices were assembled in Swagelok cells. Prepared cells were tested in 2-electrode configuration using a potentiostat/galvanostat system (Biologic VMP3). 1 M Na_2SO_4 solution was used as the electrolyte.

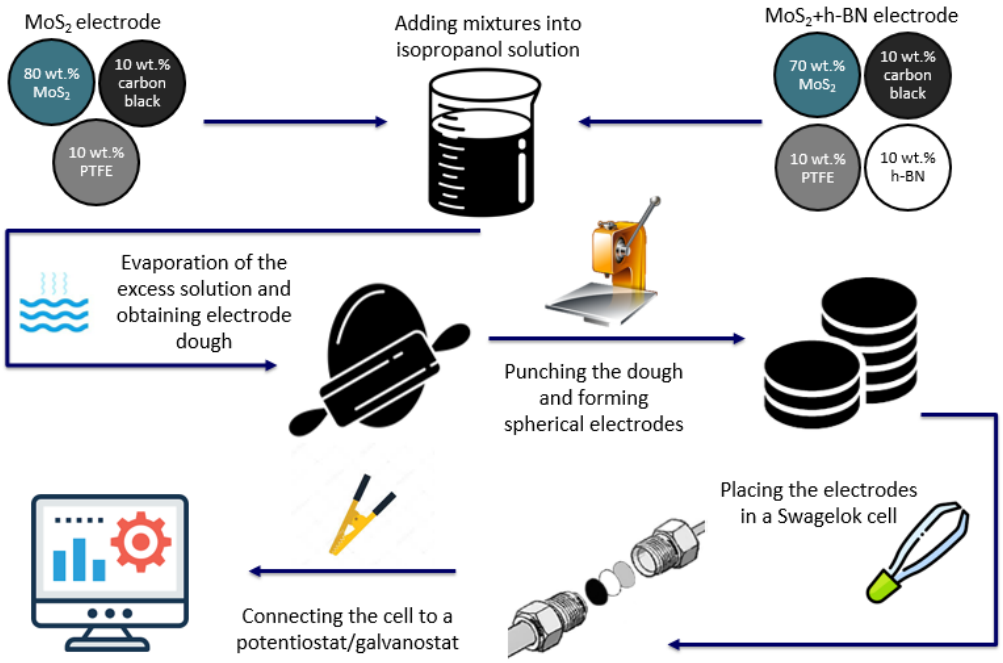

Figure 6.3. Schematic of the supercapacitor electrode preparation procedure.

6.3 Results and Discussion

Structural analysis of pristine and exfoliated MoS_2 was conducted using SEM, XRD and Raman spectroscopy techniques and the results were mentioned in Section 5.3. SEM images of pristine (p/h-BN) and exfoliated (e/h-BN) h-BN samples are provided in Figure 6.4 (a) and (b), respectively. It is clear that the exfoliation process changed the morphology of h-BN powders. Large h-BN particles were replaced with finer ones.

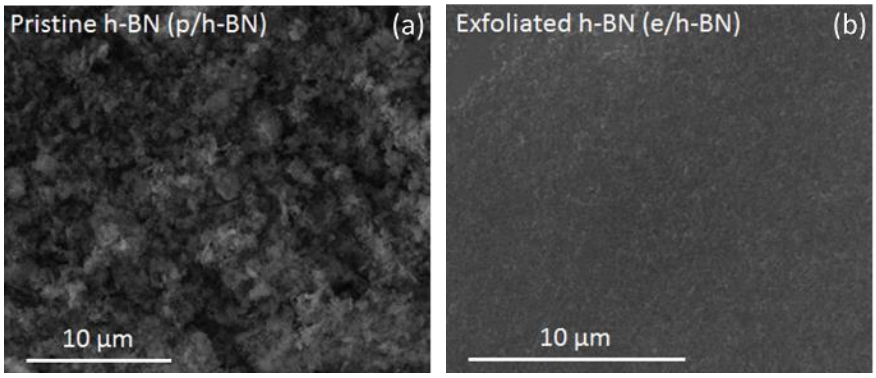

Figure 6.4. SEM images of (a) p/h-BN and (b) e/h-BN.

XRD pattern of h-BN is given in Figure 6.5 (a). In comparison with the p/h-BN, peaks of e/h-BN showed a significantly decreased intensity and notably broadened peaks, proving the presence exfoliated h-BN sheets and much less ordered structure. Raman spectra for both pristine and exfoliated samples are provided in Figure 6.5 (b) and only the characteristic E_{2g} Raman peak of h-BN was observed in both spectra. This means that the exfoliation did not cause any damage to the structure. The decrease in the intensity can be ascribed to the active material concentration in the Raman measurements. Bulk p/h-BN was a dense powder; thus, it gives a high intensity signal. On the other hand, e-h-BN had a loose structure and this led to a decrease in the Raman intensity.

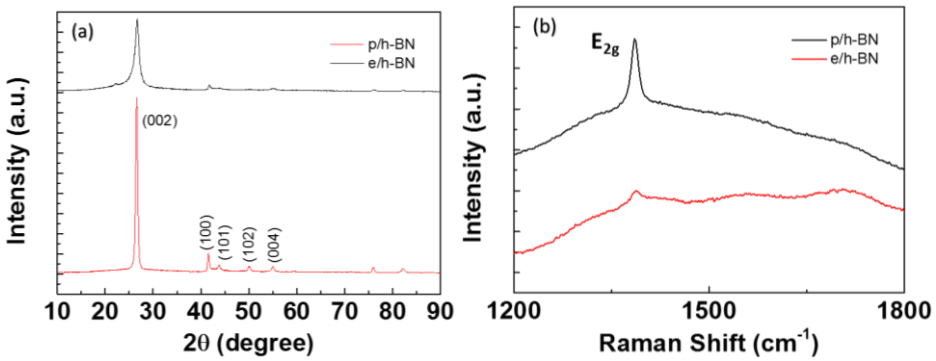

Figure 6.5. (a) XRD pattern and (b) Raman spectra of p/h-BN and e/h-BN.

Electrochemical characterization started with CV tests by applying different scan rates ranging from 20 to 400 mV/s. CV curves shown in Figure 6.6 (a) and (b)

point out that both bare MoS_2 and h-BN/MoS_2 nanocomposite electrodes have very similar rectangular shapes, which is a sign of significant capacitive behavior. At scan rates as high as 400 mV/s seen in Figure 6.6 (d), the curves of the both electrodes almost overlap. Not in striking contrast, at low scan rates such as 20 mV/s, given in Figure 6.6 (c), there is a slight difference between the curves. This means the C_{sp} values are close to each other.

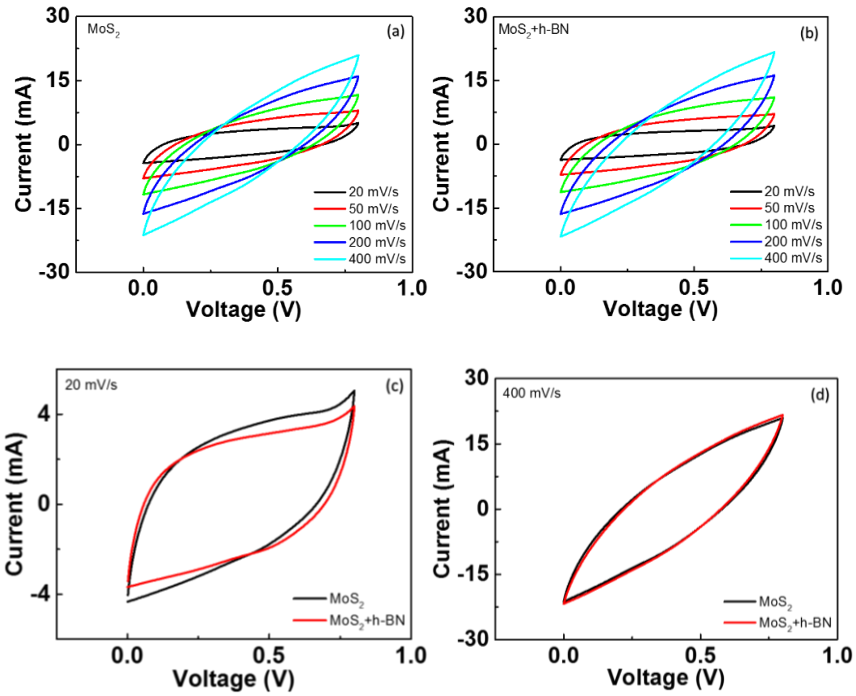

Figure 6.6. CV curves of (a) bare MoS_2 and (b) h-BN/MoS_2 composite electrodes at different scan rates. Comparison of the electrodes at (c) 20 and (d) 400 mV/s.

GCD curves of control and experimental samples, provided in Figure 6.7 (a) and (b), respectively, have characteristic triangle shape of supercapacitors. In Figure 6.7 (c), comparison of GCD curves of electrodes is given at a current density of 0.6 A/g. It is obvious that bare MoS_2 electrode had longer discharge time compared to the composite electrode and this resulted in a slightly higher capacitance in the bare electrode. On the other hand, as seen in Figure 6.7 (d) composite electrode had higher Coulombic efficiency at all current densities compared to bare MoS_2 electrode.

C_{sp} of the electrodes were calculated using Equation 2.1 and graph provided in Figure 6.8 (a) was obtained. While h-BN/MoS_2 nanocomposite electrode had a maximum C_{sp} of 43 F/g at a current density of 0.2 A/g, bare MoS_2 electrode showed a C_{sp} of 49 F/g at the same current density. Energy densities of the devices were calculated using Equation 1.3. Nanocomposite electrode had an energy density of 3.84 Wh/kg at a current density of 0.2 A/g. An energy density of 4.35 Wh/kg was obtained for the bare MoS_2 electrode at the same current density. On the other hand, composite electrode conserved 84% of its initial capacitance after 1,000 charge-discharge cycles, which was higher than the retention of the bare electrode, as shown in Figure 6.8 (b). In Figure 6.8 (c) low frequency region of the Nyquist plot obtained from EIS measurements is provided. The straight line in this region is a result of the capacitive character of the electrodes. A simplified RC equivalent circuit model, schematically illustrated in the inset of Figure 6.8 (c), was proposed for the tested symmetric cell. On the schematic, $R_{f-/+}$ and $C_{-/+}$ stand for the faradic resistance and capacitance for the negative and positive electrodes, respectively. R_S represents the ESR of the device. While bare MoS_2 electrode had an ESR of 0.89 Ω, the nanocomposite electrode showed an ESR of 1.15 Ω. The P_{max} values of the devices were calculated using Equation 1.4. Bare MoS_2 electrode had a P_{max} of 14.26 kW/kg and nanocomposite electrode showed a P_{max} of 11.08 kW/kg. Diameter of the semicircle found in high frequency region represents the charge transfer resistance and bare MoS_2 electrode had a slightly lower resistance compared to the composite electrode, as shown in Figure 6.8 (d). Similar case is valid for the series resistance values given in the inset of Figure 6.8 (d).

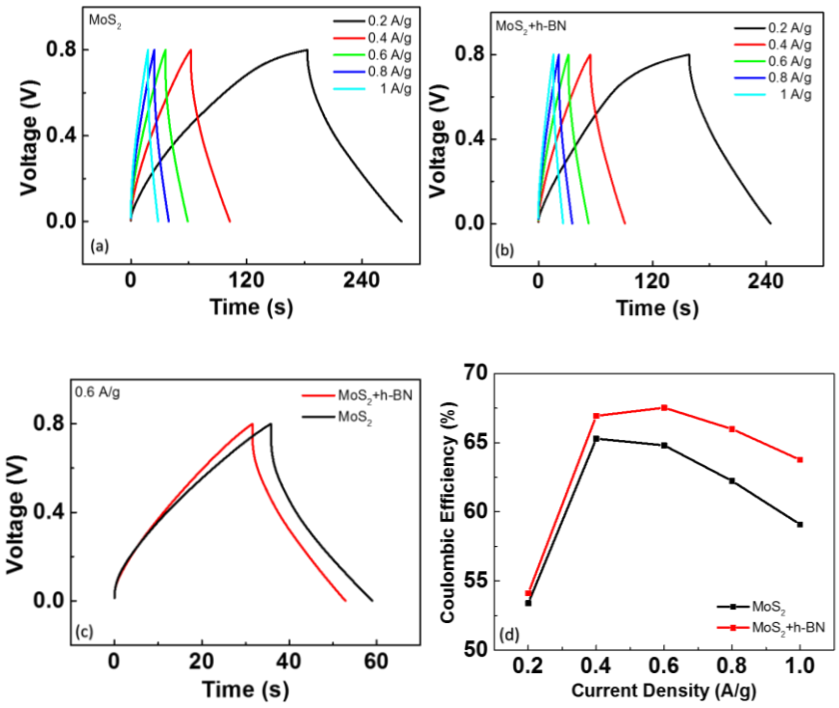

Figure 6.7. GCD curves of (a) bare MoS_2 and (b) h-BN/MoS_2 nanocomposite electrodes at different current densities. Comparison of the electrodes in (c) GCD curves at 0.6 A/g and (d) Coulombic efficiency.

The bare MoS_2 electrode showed a slightly higher C_{sp} compared to h-BN/MoS_2 nanocomposite electrode. This is ascribed to the higher resistance of the nanocomposite electrode determined by the EIS test. The presence of h-BN in the nanocomposite electrode decreased the conductivity slightly and this led to a reduction in C_{sp} compared to bare MoS_2 electrode. On the contrary, the nanocomposite electrode showed higher Coulombic efficiency and capacitance retention compared to the bare MoS_2 electrode. These enhancements are attributed to a decrease in the restacking tendency of MoS_2 nanosheets with the help of h-BN. It is known that h-BN and its derivatives are utilized as restacking inhibitor for 2D materials used in electrochemical energy storage [159]. With decreasing restacking thanks to h-BN, electrolyte ions were able to be released easily from the gaps between the MoS_2 nanosheets during discharge and thus the Coulombic efficiency

of the nanocomposite electrode improved. Similarly, with decreased restacking, the specific surface area of MoS_2 remained relatively high during 1,000 cycles of charge/discharge and therefore a higher capacitance retention performance was observed for nanocomposite electrode compared to bare MoS_2 electrode.

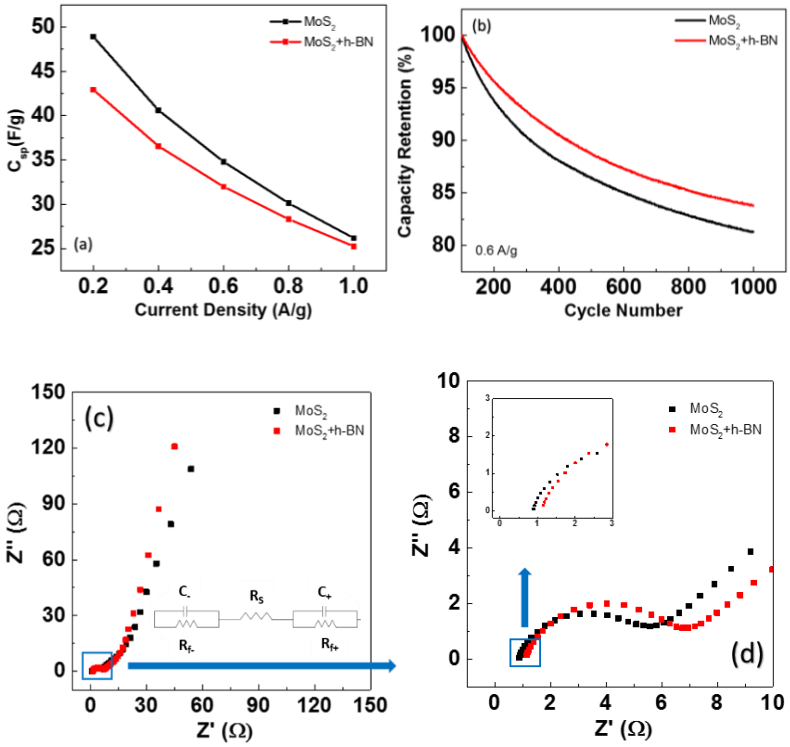

Figure 6.8. (a) *Csp* values of the electrodes at different current densities, (b) capacitance retention of the electrodes after 1,000 cycles. (c) Low and (d) high frequency region of Nyquist plot. Inset shows series resistance values.

6.4 Conclusions

Nanocomposite supercapacitor electrodes with MoS_2 and h-BN were fabricated and electrochemical characteristics were compared to that of bare MoS_2 electrodes. A specific capacitance of 43 F/g, a Coulombic efficiency of 68%, and a series resistance of 1.15 Ω in 1 M Na_2SO_4 electrolyte were obtained from the

fabricated nanocomposite electrodes. After 1,000 charge and discharge cycles, nanocomposite electrodes retained 84% of their initial capacitance. Upon nanocomposite formation, a 3% decrease in specific capacitance was observed, while Coulombic efficiency and capacitance retention was found to increase by 8% and 4%, respectively.

As can be seen here, the addition of h-BN as an active material to MoS_2-based electrodes improved the Coulombic efficiency and capacitance retention performances in the supercapacitor devices. However, the insulator nature of h-BN caused a reduction in the specific capacitance and this prevents h-BN/MoS_2 nanocomposite from being a promising electrode material for supercapacitors. Therefore, in Chapter 7, the use of h-BN as a separator material instead of an electrode material for supercapacitors is proposed.

CHAPTER 7

$Ti_3C_2T_x$ FLEXIBLE SUPERCAPACITOR WITH A HEXAGONAL BORON NITRIDE SEPARATOR DEPOSITED BY SPRAY COATING

7.1 Introduction

The use of mobile electronic devices has increased significantly in recent years, and the energy demand for these devices increased in parallel. Storage of a sufficient amount of energy within a unit directly attached to the mobile device is the most practical and efficient method to fulfill this demand. Here the compatibility of the energy storage unit and the device is quite important. It is expected that the demand for foldable or wearable electronic devices will increase in the forthcoming years, which must be followed by the development of flexible energy storage units. On the other hand, the weight and the volume of mobile electronic devices are crucial in obtaining ergonomic and low energy consuming products. Lighter and smaller mobile devices are more attractive for users. In order to meet these requirements in the electrochemical energy storage field, considerable amount of effort has been spent on electrode active materials, since they directly affect the performance of the devices. However, other device components such as separators, current collectors, binders and conductive additives are just as important as electrode active materials. Therefore, these components should be taken into consideration when designing electrochemical energy storage devices with high efficiency [160].

Following the discovery of the first two-dimensional (2D) titanium carbide ($Ti_3C_2T_x$) in 2011, a new family of 2D transition metal carbides and nitrides named MXenes emerged [161,162]. Since then, the MXene family has grown quickly and continuously. MXenes have a general formula of $M_{n+1}X_nT_x$, where M is an early transition metal, X stands for carbon or nitrogen, and n equals to 1–4 [163,164]. T_x represents the surface termination groups such as =O, -OH, -F, and -Cl on the MXene

surface [165,166]. Electrochemical characteristics of MXenes have been widely investigated because of their promising chemical and physical properties such as redox-active abundant surface groups, high electrical conductivity (up to 20,000 S/cm) [167], rapid ion transport allowed by 2D nature, and facile cation intercalation [168]. More than a quarter of all MXene-based publications to date are related to electrochemical energy storage applications, and $Ti_3C_2T_x$ is the most studied MXene among others due to its high specific capacitance along with high rate capability [169]. Benefiting from the fast surface redox reactions in an acidic electrolyte, a $Ti_3C_2T_x$ hydrogel showed an ultra-high volumetric capacitance of 1500 F/cm^3, and a macroporous $Ti_3C_2T_x$ electrode displayed an excellent rate capability at a scan rate of 100 V/s [170]. Strong surface redox in $Ti_3C_2T_x$ is also observed with organic electrolytes [171] and water-in-salt electrolytes [172], allowing $Ti_3C_2T_x$ to deliver a high capacitance under a large potential window.

In recent years, miniaturized energy storage devices have attracted much attention in mobile and wearable electronics. Long lifetime and high-power density of miniaturized electrochemical capacitors (microsupercapacitors) are highly promising for the microelectronics industry. Choice of electrode materials directly affects the final properties of the microsupercapacitors. Recently, MXenes have shown significant potential in advanced microsupercapacitors with high energy and power densities which do not require metal current collectors [173]. Peng et al. [174] developed all-MXene ($Ti_3C_2T_x$) solid-state interdigitated microsupercapacitors fabricated via spray coating, followed by direct laser cutting. The spray-coated $Ti_3C_2T_x$ was used as both the electrodes and the current collectors in the devices. The all-MXene supercapacitors showed a much lower contact resistance, higher capacitances, and better rate capabilities compared to $Ti_3C_2T_x$ microsupercapacitors containing platinum current collectors. The fabricated devices showed 27 mF/cm^2 areal capacitance and 357 F/cm^3 volumetric capacitance at a scan rate of 20 mV/s. After 10,000 cycles at a scan rate of 50 mV/s, the devices retained almost all of their capacitance, which means excellent cyclic stability. Zhang et al. [175]. fabricated a full inkjet printed MXene microsupercapacitor by employing an AlO_x-coated

polyethylene terephthalate (PET) substrate. Following printing, no stain residue was observed on the substrate, and the print was stable upon scotch tape test. The fabricated microsupercapacitor device showed a significant volumetric capacitance of 562 F/cm^3 and a high energy density of 0.32 μWh/cm^2.

h-BN nanosheets, also known as 'white graphene' or 'non-carbon graphene', are composed of alternating boron and nitrogen atoms in a hexagonal order. High specific surface area, high chemical, mechanical and thermal stability of the 2D h-BN nanosheets are attractive for many applications such as polymer matrix composites [176], sorbents [177], blue light, and ultraviolet emitters [178]. Moreover, the large bandgap and prominent ionic conductivity makes h-BN a highly promising separator in energy storage devices [151]. Gilshteyn et al. developed stretchable supercapacitors with single-walled carbon nanotube thin film electrodes and h-BN nanotube separators [179]. The spray coating method was used for the fabrication. In the two-electrode configuration, the device showed a capacitance retention of 96% after 20,000 charge/discharge cycles. In addition, a specific capacitance of 82 F/g and low series resistance of 4.6 Ω were reported for the fabricated devices. Byun et al. fabricated boron nitride/reduced graphene oxide (h-BN/rGO) hybrid films with alternately stacked layers [159]. h-BN provided proton channels to the rGO film and also enhanced the mechanical stability of the membrane in the formed van der Waals heterostructure. A high volumetric capacitance of 242 F/cm^3 was obtained at a scan rate of 10 mV/s using a 6 M KOH electrolyte. In addition, after 10,000 charge/discharge cycles, the h-BN/rGO supercapacitor device retained 99% of its initial capacitance. Recently Yang et al. fabricated $Ti_3C_2T_x$/h-BN/$Ti_3C_2T_x$ (THT) integrated supercapacitor devices using freeze-tape casting method [180]. In their study, $Ti_3C_2T_x$ layers served as symmetric electrodes, while h-BN layer was used as the separator. A calendaring process was applied to the THT stack to obtain a final thickness of 110 μm for the electrode-separator stack of the device. The device delivered a volumetric capacitance of 18.2 F/cm^3 at a scan rate 50 mV/s.

The method to fabricate microsupercapacitors depend on the type of substrates, and full-cell devices can be produced in planar interdigitated or stacked configurations [6]. In the planar interdigitated configuration, a current collector is typically patterned on an insulating substrate. However, it may not be necessary as in the case of highly conductive MXene-based electrodes. Subsequently, negative and positive electrodes are formed next to each other on the current collector [181]. For the planar interdigitated design, the critical point is to avoid shorting the negative and positive electrodes while forming the electrode material locally onto the microsized patterns [182]. In addition to this, the fabrication technique for the formation of the interdigitated structure has to be compatible with the ones used in the semiconductor industry to ensure the integration of the microsupercapacitors with other electronic units [183]. To pattern the planar designs; inkjet printing, laser scribing, and electrophoretic deposition techniques have been used. The limitation of these techniques is the obtainment of devices with low areal capacitance. In order to overcome this limitation, thick electrodes could be formed by using other techniques such as 3D printing. Meanwhile, stacked designs necessitate the use of simple and low-cost deposition techniques such as spray coating, doctor blading, or tape casting. Stacked configuration needs deposition of the necessary microsupercapacitor components on top of each other, making spray coating one of the most efficient and practical methods to form such structures. In addition, homogeneous and durable coating of 2D materials, such as MXenes and h-BN, can be achieved thanks to the proper alignment of the flakes during spray coating process.

In this study, h-BN separator layers were used in $Ti_3C_2T_x$ symmetric microsupercapacitor devices. All device layers were deposited through spray coating technique adhering to stacked design configuration. The cell was assembled directly following the deposition process without additional steps, avoiding the patterning procedures applied in planar interdigitated configuration. The final stacked microsupercapacitor device had an overall thickness of only 1.5 μm excluding the thickness of PET substrates. The device showed a volumetric capacitance of 284.3

F/cm^3 at 50 mV/s scan rate. The effect of h-BN separator thickness on the electrochemical properties including specific capacitance, series resistances, and capacitance retention was investigated in detail.

7.2 Experimental

$Ti_3C_2T_x$ and h-BN were produced following the procedures described in references [167] and [178], respectively. The flake sizes of $Ti_3C_2T_x$ and h-BN are 100-200 nm and 265 nm in diameter, respectively. All other chemicals were purchased from Sigma Aldrich and used without further purification. Environmentally friendly water-based ink was prepared by dispersing delaminated $Ti_3C_2T_x$ in DI water and used for spray coating.

Spray coating of $Ti_3C_2T_x$: A 10 cm x 5 cm rectangular pieces of PET was used as the flexible substrate. Prior to the deposition of device layers, substrates were sonicated in ethanol and DI water for 10 minutes each, dried with compressed air, and then cleaned by oxygen plasma to remove organic contaminations and increase the hydrophilicity of the surface. Plasma cleaning (Tergeo Plus Plasma Cleaner, PIE Scientific) was carried out for 5 min (4 sccm O_2 gas flow and 50 W power). Following the plasma cleaning procedure, the chamber was purged by Ar gas. 10 ml of $Ti_3C_2T_x$ water dispersion with a concentration of 10 mg/ml was transferred to the spray gun, and the coating was carried out under constant airflow. After coating and drying, a mass loading of 0.54 mg/cm^2 was determined by calculating the difference between the initial and final weights of the substrate. Afterwards, pieces of $Ti_3C_2T_x$ coated PET substrates (0.4 cm x 2.8 cm) were cut for h-BN deposition and electrode preparation.

Spray coating of h-BN: The concentration of the h-BN water dispersion was 8.3 mg/ml. 30 wt.% of the dispersed material was PVA, as the addition of PVA can improve the mechanical durability of the thin film. 1, 2, and 4 ml h-BN dispersions were sprayed onto $Ti_3C_2T_x$ coated PET substrates in order to determine the optimum

thickness of the h-BN layer. After spraying, the electrodes were kept in a vacuum oven overnight for complete drying.

Device assembly: Symmetric devices were fabricated. For this purpose, one piece of $Ti_3C_2T_x$ deposited PET substrate was used as one of the electrodes of the device, and h-BN and $Ti_3C_2T_x$ deposited PET substrate was used as the other electrode. The stacked electrodes were sandwiched between neat PET films with acrylic tapes. Graphite papers were used as current collectors by attaching to the device. Lastly, a 1 M lithium sulfate (Li_2SO_4) electrolyte was injected into the device using a needle and syringe. In addition, a control sample was prepared using identical preparation steps and utilizing a Celgard 3501 separator.

XRD analysis: XRD measurements were performed on a Rigaku D/Max-2000 pc diffractometer using Cu K_α (wavelength: 1.5406 Å) X-ray beam at 40 kV and 30 mA, with a step scan of 0.02°, a 2θ range of 3° to 90°, and a step rate of 1°/min.

SEM analysis: SEM analysis was carried out with a Zeiss Supra 50VP instrument at an accelerating voltage of 5 kV in the InLens mode.

Optical microscopy: In order to determine the evenness and homogeneity of the coatings, the samples were examined under Keyence Laser Microscope optical profilometer.

Electrochemical analysis: For the electrochemical tests of the supercapacitor devices, a Biologic VMP3 potentiostat/galvanostat system was used.

The specific capacitance and cell capacitance values were calculated using the formula below:

$$C_{sp} = \frac{2}{m(V_2 - V_1)} \int_{t=0(V_1)}^{t(V_2)} i(V)dt \quad (7.1)$$

,where i (A) is the measured current, m (g) is the mass of total active material in both electrodes or the total mass of the stacking (both electrodes and the separator), V_1

(V) and V_2 (V) are the initial and final voltage values within the voltage window, and t (s) is the time.

Gravimetric energy density, areal energy density, volumetric energy density, and volumetric power density values were calculated using the formulas below, respectively:

$$E_G = \frac{C \times V^2}{2 \times m}, E_A = \frac{C \times V^2}{2 \times A}, E_V = \frac{C \times V^2}{2 \times \vartheta}, P_V = \frac{E_V}{t} \quad (7.2)$$

,where C (F) is the capacitance of the cell, V is the voltage window, m is the total mass of the electrodes or stacking, A (cm^2) is the contact area of the electrodes, v (cm^3) is the total volume of the electrodes and the separator layer, and t is the discharge time.

7.3 Results and Discussion

The fabrication process of the $Ti_3C_2T_x$-h-BN microsupercapacitor is illustrated in Figure 7.1 (a). Two identical $Ti_3C_2T_x$ coated PET substrates were prepared by spray coating of $Ti_3C_2T_x$ water dispersion. Then, one of the $Ti_3C_2T_x$ coated PET was further spray-coated with h-BN layer. The two electrode films were assembled face to face into a device, which can be tested in a flat or bent form. Figure 7.1 (b) provides XRD patterns of $Ti_3C_2T_x$ coated PET and both $Ti_3C_2T_x$ and h-BN coated PET substrates. The XRD shows the signature peaks of PET substrate at 23° and 26° in both films. h-BN peak located at 26°, overlaps with one of the peaks of PET (JCPDS No. 34-0421). In both diffraction patterns, the characteristic peaks of $Ti_3C_2T_x$ (00l) are observed at 8°, 18°, 26°, 36° and 44°. The *d*-spacing of $Ti_3C_2T_x$ MXene was derived from the 002 peak [184,185]. It was calculated to be 10.99 Å, which is similar to the *d*-spacing of delaminated $Ti_3C_2T_x$ MXene film [184]. After the h-BN coating, the *d*-spacing value only slightly changed to 10.77 Å. This indicated that the h-BN spray coating process did not destroy the layered structure of the underlying $Ti_3C_2T_x$ coated onto PET.

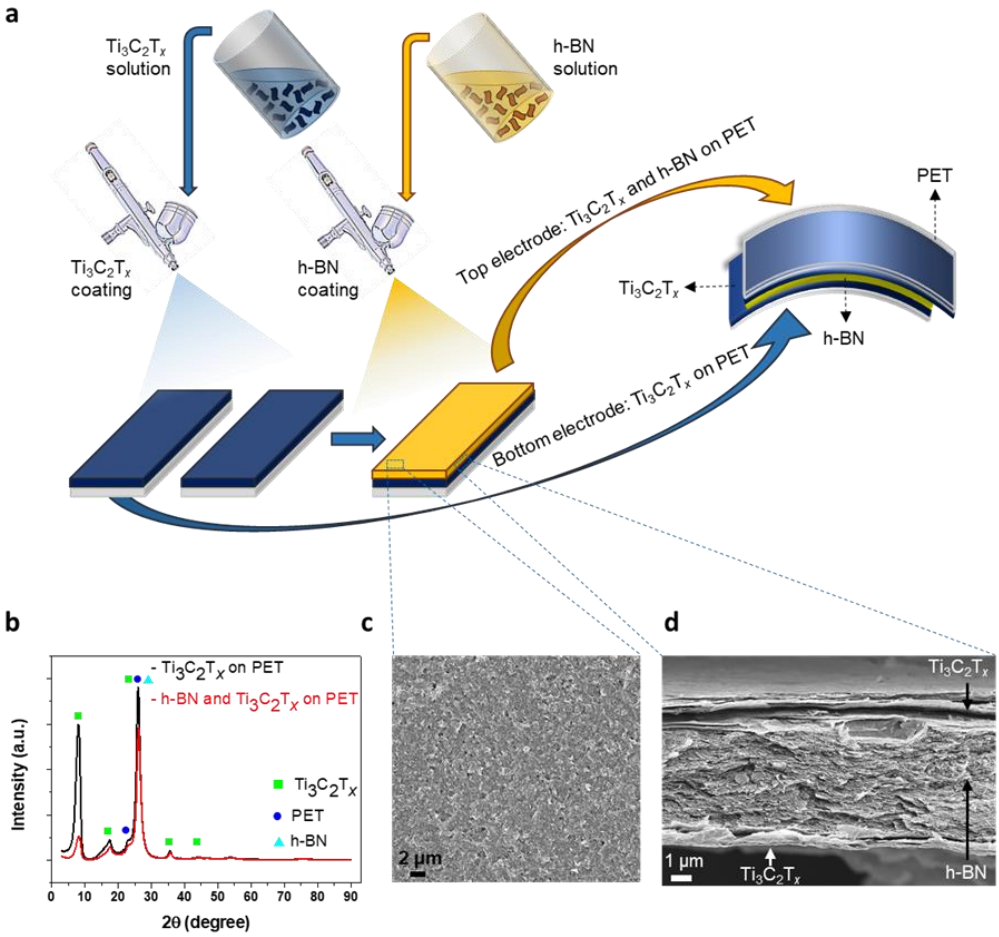

Figure 7.1. (a) Schematic illustration of the fabrication steps of a supercapacitor device with spray-coated h-BN as the separator, (b) XRD patterns of the electrodes before (black) and after (red) h-BN coating on $Ti_3C_2T_x$, (c) top view SEM image of h-BN coating with PVA and (d) cross-sectional SEM image of h-BN layer sandwiched in-between two layers of $Ti_3C_2T_x$ MXenes.

Figure 7.1 (c) shows the top view SEM image of the h-BN coating, demonstrating that h-BN completely covered the surface of the $Ti_3C_2T_x$ electrode. A conductivity measurement was performed by a multimeter on several points of the h-BN coated film, ensuring that the h-BN was able to isolate the surface of the $Ti_3C_2T_x$ electrode as a separator. Moreover, the minimum thickness of h-BN that can achieve a homogeneous and isolative coating on $Ti_3C_2T_x$ was estimated to be 300 nm. Figure A.1 (a) shows the top-view SEM image of h-BN coating without PVA.

The coating of h-BN sheets without PVA was not uniform on the surface of the substrate compared to that with PVA. As shown in Figure 7.1 (c), the deposition of h-BN with PVA resulted in a high homogeneous film across the whole surface. Besides, the PVA assisted h-BN bond to the substrate more effectively and increased the durability of the separator upon electrolyte exposure. A cross-sectional SEM image of h-BN separator sandwiched between two $Ti_3C_2T_x$ layers is provided in Figure 7.1 (d). The edge between the $Ti_3C_2T_x$ layers and h-BN layer can be clearly distinguished, indicating successful separation of two $Ti_3C_2T_x$ layers. The image shows the h-BN thickness of 5 μm, which corresponds to a mass loading of 0.6 mg/cm^2. The mass loading of h-BN was determined by calculating the mass difference before and after the coating. In order to examine the films in more detail an optical profilometer is used, and 3D images of $Ti_3C_2T_x$ and h-BN coatings obtained with the help of this device are provided in Figure A.1 (b) and (c), respectively. 3D optical profilometer images proved that the spray coating procedure resulted in deposition of homogeneous $Ti_3C_2T_x$ and h-BN layers.

1, 2, and 4 ml of h-BN water dispersions (8.3 mg/ml) were spray-coated onto the $Ti_3C_2T_x$ film, which are denoted as 1/h-BN, 2/h-BN, and 4/h-BN, respectively. The thicknesses of 1/h-BN, 2/h-BN and 4/h-BN coatings were estimated to be 300 nm, 600 nm and 1200 nm, respectively. In determination of the thicknesses, the ratio between mass loading and film thickness derived from Figure 7.1 (d) was used. The summary of the relationship between mass loading, sprayed h-BN dispersion amount, and film thickness for all samples is given in Figure A.1 (d). Two-electrode configuration was used to measure the electrochemical properties of the fabricated microsupercapacitor devices with h-BN separator. Meanwhile, the typical Celgard separator was used in a control cell, and this cell with Celgard separator was denoted as CCS. Figure 7.2 (a) shows the CV curves of the 1/h-BN, 2/h-BN, 4/h-BN, and CCS. The area of the CV curve of 1/h-BN is larger than that of 2/h-BN, 4/h-BN, and CCS, indicating its higher specific capacitance among tested devices. The lower capacitance of $Ti_3C_2T_x$ in the cells with a thicker h-BN coating (2/h-BN and 4/h-BN) should be caused by the larger resistance through the whole cell.

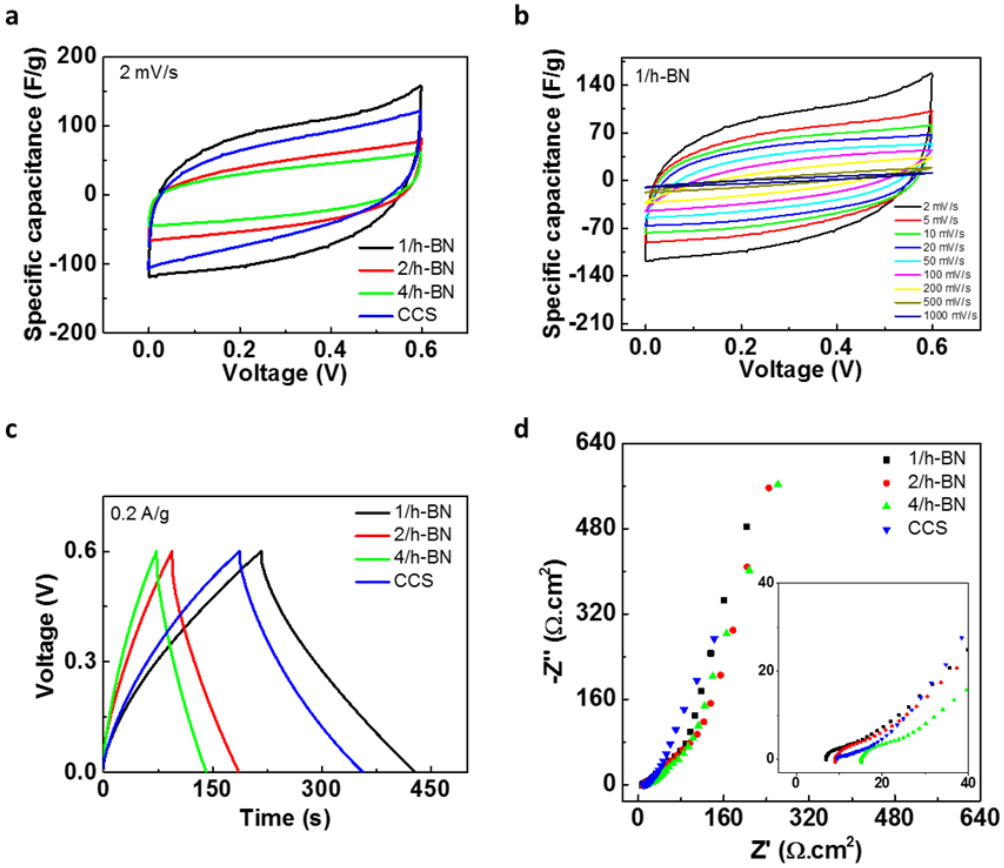

Figure 7.2. (a) Comparison of CV curves of 1/h-BN, 2/h-BN, 4/h-BN and CCS, (b) CV curves of 1/h-BN at scan rates from 2 to 1,000 mV/s, (c) GCD curves of 1/h-BN, 2/h-BN,4/h-BN and CCS at 0.2 A/g, and (d) Nyquist plot of 1/h-BN, 2/h-BN, 4/h-BN and CCS cells. Inset shows the high-frequency region.

The specific capacitances of the cells, which were calculated based only on the weights of the electrode materials, are 92.7, 63.3, 36.4, and 73.5 F/g at a scan rate of 2 mV/s for 1/h-BN, 2/h-BN, 4/h-BN, and CCS, respectively. However, practically, the presence of the separator also contributes to the overall mass/volume of the cell. Therefore, the specific capacitance of full-cells, including the mass of both the electrodes and the separator, were also evaluated and shown in Figure A.2 (a). These capacitance values were referred to as cell capacitances. The cell capacitances were then calculated to be 89.7, 60.4, and 32.3 F/g (or 725.6, 451.6, and 178.1 F/cm^3) for 1/h-BN, 2/h-BN, and 4/h-BN, respectively at a scan rate of 2

mV/s. Meanwhile, the cell capacitance of CCS at 2 mV/s is 24.3 F/g (30.4 F/cm^3). The much lower cell capacitance of CCS cell was due to the much larger weight and volume of the Celgard compared to the thin h-BN separators. This clearly demonstrated that using thin and light-weight separators is highly crucial to increase the overall capacitance of the practical cells.

The rate capabilities of the cells with h-BN and Celgard separators were evaluated at different scan rates from 2 to 1,000 mV/s. CVs of 1/h-BN at different scan rates are shown in Figure 7.2 (b). The 1/h-BN retained its pseudo-rectangular CV shape even at a high scan rate of 1,000 mV/s. The capacitances at different scan rates are given in Figure A.2 (b). CCS had the lowest cell capacitance at different scan rates, while 1/h-BN showed the highest values at each scan rate. Specifically, 1/h-BN delivered a specific capacitance of 92.7 F/g at a scan rate of 2 mV/s and retained about 40% of its performance at 50 mV/s. Increased h-BN thickness lowered the rate capability, which was attributed to the longer ion transport paths through the h-BN separator in higher thicknesses.

Galvanostatic charge/discharge (GCD) curves of the cells at a current density of 0.2 A/g are provided in Figure 7.2 (c). Again, 1/h-BN showed higher capacitance compared to CCS and other h-BN coatings. Figure A.2 (c) shows GCD curves of 1/h-BN recorded at different current densities. It can be observed that 1/h-BN retained its symmetrical triangle GCD shape for all current densities indicating its high Coulombic efficiency. The detailed Coulombic efficiencies for different h-BN thicknesses are shown in Figure A.2 (d) at different current densities ranging from 0.2 A/g to 1 A/g. 1/h-BN along with 2/h-BN exhibited higher Coulombic efficiencies than 4/h-BN and CCS for all current densities. Especially, the Coulombic efficiency of 1/h-BN was larger than 99% for the current densities higher than 0.4 A/g.

Figure 7.2 (d) shows the Nyquist plot obtained through EIS measurements. The test was carried out under an AC perturbation of 10 mV and in a frequency range of 300 kHz to 10 mHz. All samples had nearly vertical Nyquist plots at low frequencies, which signified a combined capacitive and diffusion-controlled process.

The difference between the samples became prominent in the high-frequency region presented in the inset of the Figure 7.2 (d). 1/h-BN showed a lower series resistance than all other samples, including CCS. With increasing h-BN separator thickness, the series resistance was found to increase. The series resistance of 4/h-BN was higher than that of CCS. The straight line with a -45° angle in the mid-frequency region of the Nyquist plot represents Warburg resistance related to the ionic diffusion. Warburg resistance is directly proportional with the slope of the linear fit of real part of impedance ($Z^{'}$) versus frequency to the power of -0.5 ($\omega^{-1/2}$) within the frequency range of Warburg resistance [186]. As shown in Figure A.3 (a), h-BN separators showed a steeper slope than CCS, indicating that ion diffusivity was lower in the h-BN separators than Celgard. However, the ultra-thin coating of h-BN reduced the diffusion length significantly, leading to a higher rate capability especially in 1/h-BN.

The schematic provided in Figure 7.3 (a) illustrates that the volume of the cell was significantly reduced when a 25 μm thick 3501 Celgard separator was replaced by a 300 nm thick h-BN (1/h-BN). The volumetric energy and power density of the cells, calculated by including the volume of the separator, are provided in a Ragone plot (Figure 7.3 (b)). 1/h-BN showed the highest energy and power densities among all samples. When compared to CCS, 1/h-BN showed 25 times higher energy density and 20 times higher power density at a current density of 0.2 A/g. In addition, 1/h-BN was compared with some prototype/commercialized energy storage devices, and it showed higher performance in both energy and power density values [171,187]. On the other hand, gravimetric, areal, and volumetric energy densities of the samples at different scan rates are given in Figure A.3 (b), (c), and (d), respectively. 1/h-BN cell showed 3.7 times higher gravimetric, 1.2 times higher areal, and 23.9 times higher volumetric energy density compared to CCS at a scan rate of 2 mV/s. This enhancement is assigned to the low weight and volume of 1/h-BN.

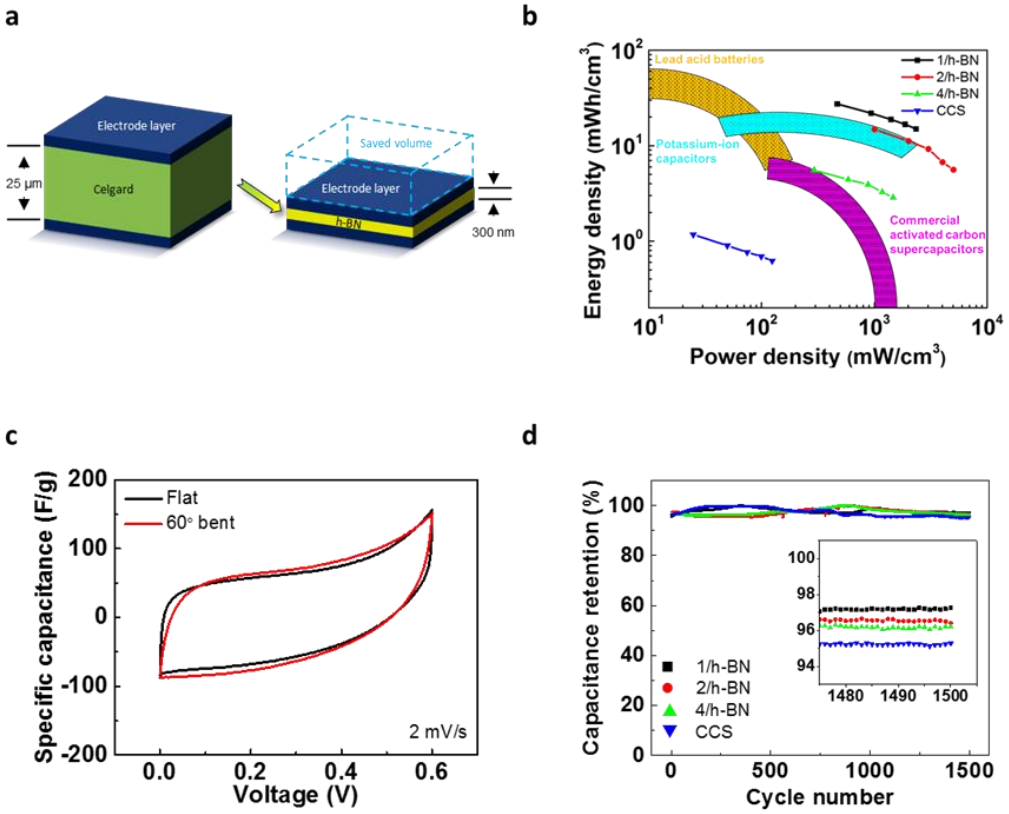

Figure 7.3. (a) Schematic illustration of saved volume upon the use of thin h-BN separator instead of the Celgard separator, (b) Ragone plot for 1/h-BN, 2/h-BN, 4/h-BN, CCS and some prototype/commercialized devices [171,187], (c) CV curves of flat (black) and 60° bent (red) 1/h-BN devices, and (d) capacitance retention tests for the devices. Inset shows the last 30 cycles of the capacitance retention test.

The performance of 1/h-BN cell was also evaluated under bending conditions to demonstrate the flexibility of the cell. The CV curves of the cell with and without bending are shown in Figure 7.3 (c). At a scan rate of 2 mV/s, the performance of the device remained almost the same upon 60° bending. At 20 mV/s, the performance of 60° bent device was also comparable with the flat one (Figure A.4 (a)). Photographs of the fabricated flexible device showing its electrochemical setup and flexible structure can be seen in Figure A.4 (b) and (c), respectively.

The cycling stability of all cells was tested through 1,500 charge/discharge cycles. As shown in Figure 7.3 (d), 1/h-BN showed the highest capacitance retention of around 97%. Not only 1/h-BN but also 2/h-BN and 4/h-BN had higher capacitance retention performances than CCS. This is attributed to the higher Coulombic efficiencies of the cells with h-BN separator compared to CCS (Figure A.2 (d)). The cells reached their maximum capacitance after a certain number of cycles. This can be attributed to the wetting of electrodes and separator upon initial cycles. Meanwhile, the Coulombic efficiency of all samples was monitored during 1,500 charge/discharge cycles (Figure A.4 (d)). All the cells retained their Coulombic efficiencies at above 99% after 1,500 cycles (inset in Figure A.4 (d)).

7.4 Conclusions

In this study, the use of thin-film h-BN as an efficient separator layer in symmetric supercapacitors has been demonstrated. In these devices, $Ti_3C_2T_x$ was used as electrode active material. The spray coating technique was used to deposit both h-BN and $Ti_3C_2T_x$ layers on PET substrates. Fabricated supercapacitors showed improved electrochemical performance in 1 M Li_2SO_4 electrolyte. The reduced thickness of the separator decreased the volume of the full-cell, significantly increasing the energy and power densities. The device with a 300 nm thick h-BN separator outperformed the control device with the Celgard separator in Coulombic efficiency, series resistance, and capacitance retention. The low weight of h-BN separator compared to Celgard provided obtaining higher specific capacitance. In addition, the device with h-BN separator retained its high performance in the bending test. As a result, the $Ti_3C_2T_x$ MXene symmetric supercapacitor device with thin-film h-BN separator layer showed promising performance for flexible energy storage applications.

CHAPTER 8

CONCLUSIONS, RECOMMENDATIONS AND INFERENCES

8.1 Summative Conclusions

In this thesis, it is aimed to develop nanocomposite supercapacitor electrodes. For this purpose, six different nanocomposites are prepared and investigated in six separate studies. The brief summaries and the conclusions of the studies are as follows:

Chapter 2: In this work aluminum foils are coated with VACNTs using CVD technique. This is followed by the coating of PANI on the VACNT layer. A facile and inexpensive technique for the production of nanocomposite supercapacitor devices is designed. Electrochemical properties of the produced nanocomposite electrodes are investigated via CV, GCD and EIS tests. Produced VACNT/PANI nanocomposite electrodes with 15 coating cycles exhibits remarkable electrochemical performance. The specific capacity of nanocomposite electrodes is determined as 16.17 mF/cm^2 at a current density of 0.25 mA/cm^2.

Chapter 3: EG/PPy nanocomposites are employed for the production of highly flexible paper-based supercapacitors. Brush-painted EG papers are used as substrates for the coating of PPy. The prepared nanocomposite electrodes have the effective material loading. Produced paper-based electrodes do not contain conductive additives, current collectors, and heavy binders. In nanocomposite electrodes, EG layer on paper contributes to the charge transfer and homogeneous PPy layer on the surface of the electrode enhances capacitance thanks to its pseudocapacitive behavior. Produced nanocomposite electrodes are quite flexible, with the help of notable mechanical integrity of EG, PPy and paper substrate. A specific capacitance of 177.8 F/g, along with a capacitance retention of more than 94.9% is determined upon 5,000 cycles. With the facile production and notable electrochemical

performance observed, produced paper-based nanocomposite supercapacitors are suitable to use as power units in flexible electronic devices.

Chapter 4: CNF-MnO_2 nanocomposite supercapacitor electrodes are fabricated. While CNFs are synthesized via ICP using ethanol precursor, MnO_2 is produced by a simple wet chemical method. Electrochemical properties of CNF-MnO_2 nanocomposite electrodes are determined and compared to that of bare components. The CNF-MnO_2 nanocomposite electrode shows a specific capacitance of 220.38 F/g at a current density of 0.1 A/g. The Coulombic efficiency and the capacitance retention of the CNF-MnO_2 nanocomposite electrodes are found to be 23% and 18% higher than those of bare MnO_2 electrodes, respectively.

Chapter 5: The production and electrochemical characterization of nanocomposite aerogel supercapacitor electrodes consisting of MoS_2 nanosheets and rGO attached to nickel foams are studied. GO is synthesized through Tour method. rGO aerogel is obtained from GO dispersion via solvothermal method followed by freeze-drying and thermal reduction. For the production of nanocomposite electrodes, prepared rGO aerogels are simply attached onto nickel foams by applying pressure. Then exfoliated MoS_2 nanosheets are drop-casted onto the rGO aerogels. Electrochemical characteristics such as C_{sp} and capacitance retention of the produced nanocomposite electrodes are investigated using CV, GCD and EIS in two-electrode cells. Results of the tests are compared to that of control samples prepared by pressing only neat rGO aerogel onto nickel foam substrates. Prepared nanocomposite supercapacitor electrodes exhibit promising performances in 6 M KOH electrolyte with a specific capacitance of 67.5 mF/cm^2 at 2 mA/cm^2. A Coulombic efficiency of 87% is observed for the fabricated electrodes. Upon 3,000 charge and discharge cycles, C_{sp} of the nanocomposite electrodes diminishes to 81% of its initial capacitance value.

Chapter 6: In this work, 2D h-BN/MoS_2 nanocomposite electrodes are fabricated through solution phase synthesis technique and their electrochemical properties are examined. Before the fabrication of the electrodes both h-BN and MoS_2 are exfoliated using practical methods. Electrochemical characteristics such as C_{sp} and

capacitance retention of the prepared nanocomposite electrodes are evaluated via CV, GCD and EIS in two-electrode configuration. Results are compared to that of the control sample produced from neat MoS_2 nanosheets. Prepared supercapacitor electrodes have notable specific capacitances exceeding 40 F/g.

Chapter 7: In this work, the use of h-BN as an efficient separator in symmetric $Ti_3C_2T_x$ MXene supercapacitors is investigated. The spray coating method is used to deposit both h-BN and $Ti_3C_2T_x$ layers on PET substrate adhering to stacked microsupercapacitor design without any interdigitated patterns. The total thickness of the symmetric $Ti_3C_2T_x$ device with the h-BN separator is about 20 times thinner than the device with the commercial Celgard separator, which significantly increases the volumetric energy density. The increased energy density and facile fabrication procedure make the $Ti_3C_2T_x$ MXene symmetric supercapacitor devices with thin-film h-BN separator promising energy storage units in flexible and wearable electronic devices.

8.2 Future Recommendations

All of these conclusions provide quite a valuable perspective about the nanocomposite supercapacitors mentioned in this thesis. On the other hand, also some recommendations for future work can be given as follows:

Chapter 2: Specific capacitance is directly proportional to specific surface area in supercapacitors. Increasing the thickness of the VACNT layer may improve the specific surface area and thus the specific capacitance of the nanocomposite supercapacitor.

Chapter 3: A more systematic coating method such as ultrasonic spray pyrolysis may be used for the deposition of expanded graphite to obtain more reproducible results.

Chapter 4: The morphology of MnO_2 nanoparticles changes with different crystal structures. The effects of other crystal structures of MnO_2 different from α-MnO_2

nanospheres, such as δ-MnO_2 nanosheets, on the nanocomposite supercapacitors may be examined.

Chapter 5: The active materials may be deposited onto a flexible substrate instead of nickel foam to obtain supercapacitor devices with extra functionalities.

Chapter 6: h-BN nanosheets may be synthesized by easier methods such as shear exfoliation instead of ball milling.

Chapter 7: In asymmetric supercapacitors, $Ti_3C_2T_x$ is very attractive as a negative electrode along with appropriate positive electrodes such as MnO_2. The performance of h-BN/PVA nanocomposite separator may be examined in a $Ti_3C_2T_x/MnO_2$ asymmetric supercapacitor device.

8.3 General Inferences

At the end of this thesis study, the following sights are put forward about the questions asked in the section of dissertation objectives.

- To what extent it is possible to develop nanocomposite supercapacitors without compromising the superior properties of the individual materials?

First of all, it is obvious that transferring all properties of the individual materials to the composites with 100% efficiency is impossible in all application areas of materials science. This case, of course, is also valid for supercapacitors. Yet, approaching 100% efficiency is the ultimate goal in every field. In the light of results obtained from the research conducted during this thesis study, it is concluded that supercapacitors benefit quite efficiently from the formation of composites. This is because two main types of supercapacitors, EDLCs and pseudocapacitors, store charges through two different storage mechanisms. Therefore, generally, pure materials do not suppress the properties of each other. This once more proves the importance of material selection in the formation of composite supercapacitor electrodes.

- What are the contributions of nanocomposites to low energy density, which is the biggest problem for supercapacitors to approach batteries?

Batteries are clearly dominating the energy storage products market. They are widely used in different application areas, from portable devices to electric vehicles. On the other hand, the use of commercial supercapacitors is generally limited in the fields demanding high power density. Since commercial supercapacitors are mostly based on EDLC-type carbonaceous materials, their energy densities are quite low. In this thesis study, it is understood that the formation of EDLC-pseudocapacitor composites can significantly improve the supercapacitors' energy densities and bring supercapacitors closer to batteries in terms of energy density. Here, however, the high costs of the pseudocapacitors start to be a problem and this problem prevents EDLC-pseudocapacitor composite from being widely commercialized. If new techniques can be developed to synthesize pseudocapacitors or cheap alternatives of expensive pseudocapacitors are discovered, we may see more composite supercapacitors competing with batteries in the coming years.

- What can nanocomposites bring in supercapacitors within today's hot topics such as long cycle life, flexibility, and environmentally friendly devices?

Today, expectations from electronic devices have changed significantly. For example, in the past, energy storage devices with relatively high energy density values were sufficient to get commercialized. However, nowadays, in addition to high energy density, many other functionalities are demanded. With developing technology, the time spent with mobile devices has increased notably and consumers have started to charge their devices more in their daily routine. This raises the need for devices with long cycle life. Composite formation improves the Coulombic efficiency and can solve supercapacitors' low cycle life problems. Similarly, the 'Internet of Things' concept became popular in recent years and many objects, including clothes and wearable accessories, started to require energy. Especially wearable technologies need flexible energy storage devices. Composites prepared by adding some reinforcement materials to active materials can improve the mechanical

properties of the energy storage devices and thus, they can withstand repeating bending conditions. On the other hand, industrialization without control causes environmental problems. Therefore, environmentally friendly solutions attract plenty of attention in every field of materials science. Some materials may show high performance as an active energy storage material, but at the same time, they may be quite hazardous to the environment. In such cases, the use of environmentally friendly materials in the form of composites can compete with toxic materials.

In this thesis study, it was observed that the nanocomposites improved the properties of supercapacitors exemplified above and several other unmentioned properties. As the last word, it should be stated that nanocomposites are quite efficient materials to improve the properties of supercapacitors and it is believed that many more studies will be conducted in this area in the coming years.

REFERENCES

[1] Conway BE. Electrochemical Supercapacitors. Springer US; 1999. https://doi.org/10.1007/978-1-4757-3058-6.

[2] Pandolfo T, Ruiz V, Sivakkumar S, Nerkar J. General Properties of Electrochemical Capacitors. Supercapacitors 2013:69–109. https://doi.org/https://doi.org/10.1002/9783527646661.ch2.

[3] Service RF. New "Supercapacitor" Promises to Pack More Electrical Punch. Science (80-) 2006;313:902. https://doi.org/10.1126/science.313.5789.902.

[4] Simon P, Gogotsi Y. Materials for electrochemical capacitors. Nat Mater 2008;7:845. https://doi.org/10.1038/NMAT2297.

[5] Miller JR. Brief History of Supercapacitors. Batter + Energy Storage Technol 2007:61–78.

[6] Simon P, Gogotsi Y. Perspectives for electrochemical capacitors and related devices. Nat Mater 2020;19:1151–63. https://doi.org/10.1038/s41563-020-0747-z.

[7] Patrice S, Yury G, Bruce D. Where Do Batteries End and Supercapacitors Begin? Science (80-) 2014;343:1210–1. https://doi.org/10.1126/science.1249625.

[8] Simon P, Gogotsi Y. Capacitive Energy Storage in Nanostructured Carbon–Electrolyte Systems. Acc Chem Res 2013;46:1094–103. https://doi.org/10.1021/ar200306b.

[9] Conway BE. Transition from "Supercapacitor" to "Battery" Behavior in Electrochemical Energy Storage. J Electrochem Soc 1991;138:1539–48. https://doi.org/10.1149/1.2085829.

[10] Augustyn V, Come J, Lowe MA, Kim JW, Taberna P-L, Tolbert SH, et al. High-rate electrochemical energy storage through Li+ intercalation

pseudocapacitance. Nat Mater 2013;12:518–22. https://doi.org/10.1038/nmat3601.

[11] Aricò AS, Bruce P, Scrosati B, Tarascon J-M, van Schalkwijk W. Nanostructured materials for advanced energy conversion and storage devices. Nat Mater 2005;4:366–77. https://doi.org/10.1038/nmat1368.

[12] Okubo M, Hosono E, Kim J, Enomoto M, Kojima N, Kudo T, et al. Nanosize Effect on High-Rate Li-Ion Intercalation in LiCoO2 Electrode. J Am Chem Soc 2007;129:7444–52. https://doi.org/10.1021/ja0681927.

[13] Boisset A, Athouël L, Jacquemin J, Porion P, Brousse T, Anouti M. Comparative Performances of Birnessite and Cryptomelane MnO2 as Electrode Material in Neutral Aqueous Lithium Salt for Supercapacitor Application. J Phys Chem C 2013;117:7408–22. https://doi.org/10.1021/jp3118488.

[14] Wang G, Zhang L, Zhang J. A review of electrode materials for electrochemical supercapacitors. Chem Soc Rev 2012;41:797–828. https://doi.org/10.1039/C1CS15060J.

[15] Najib S, Erdem E. Current progress achieved in novel materials for supercapacitor electrodes: mini review. Nanoscale Adv 2019;1:2817–27. https://doi.org/10.1039/C9NA00345B.

[16] Fialkov AS. Carbon application in chemical power sources. Russ J Electrochem 2000;36:345–66.

[17] Pandolfo AG, Hollenkamp AF. Carbon properties and their role in supercapacitors. J Power Sources 2006;157:11–27. https://doi.org/10.1016/j.jpowsour.2006.02.065.

[18] Frackowiak E. Electrode Materials with Pseudocapacitive Properties. Supercapacitors 2013:207–37. https://doi.org/https://doi.org/10.1002/9783527646661.ch6.

[19] Shimizu W, Makino S, Takahashi K, Imanishi N, Sugimoto W. Development

of a 4.2 V aqueous hybrid electrochemical capacitor based on MnO2 positive and protected Li negative electrodes. J Power Sources 2013;241:572–7. https://doi.org/https://doi.org/10.1016/j.jpowsour.2013.05.003.

[20] Sathiya M, Prakash AS, Ramesha K, Tarascon J, Shukla AK. V2O5-Anchored Carbon Nanotubes for Enhanced Electrochemical Energy Storage. J Am Chem Soc 2011;133:16291–9. https://doi.org/10.1021/ja207285b.

[21] Gogotsi Y, Penner RM. Energy Storage in Nanomaterials – Capacitive, Pseudocapacitive, or Battery-like? ACS Nano 2018;12:2081–3. https://doi.org/10.1021/acsnano.8b01914.

[22] Zhao X, Sánchez BM, Dobson PJ, Grant PS. The role of nanomaterials in redox-based supercapacitors for next generation energy storage devices. Nanoscale 2011;3:839–55. https://doi.org/10.1039/C0NR00594K.

[23] Liu C, Li F, Ma L-P, Cheng H-M. Advanced Materials for Energy Storage. Adv Mater 2010;22:E28–62. https://doi.org/10.1002/adma.200903328.

[24] Farsi H, Gobal F, Barzgari Z. A study of hydrated nanostructured tungsten trioxide as an electroactive material for pseudocapacitors. Ionics (Kiel) 2013;19:287–94. https://doi.org/10.1007/S11581-012-0726-8.

[25] Zheng JP, Cygan PJ, Jow TR. Hydrous Ruthenium Oxide as an Electrode Material for Electrochemical Capacitors. J Electrochem Soc 1995;142:2699–703. https://doi.org/10.1149/1.2050077.

[26] Trasatti S, Kurzweil P. Electrochemical supercapacitors as versatile energy stores. Platin Met Rev 1994;38:46–56.

[27] Kötz R, Carlen M. Principles and applications of electrochemical capacitors. Electrochim Acta 2000;45:2483–98. https://doi.org/https://doi.org/10.1016/S0013-4686(00)00354-6.

[28] Yu A, Chabot V, Zhang J. Electrochemical Supercapacitors for Energy Storage and Delivery: Fundamentals and Applications. CRC Press; 2017. https://doi.org/10.1201/b14671.

[29] Laforgue A, Simon P, Sarrazin C, Fauvarque JF. Polythiophene-based supercapacitors. J Power Sources 1999;80:142–8. https://doi.org/10.1016/S0378-7753(98)00258-4.

[30] Clemente A, Panero S, Spila E, Scrosati B. Solid-state, polymer-based, redox capacitors. Solid State Ionics 1996;85:273–7. https://doi.org/https://doi.org/10.1016/0167-2738(96)00070-7.

[31] Ryu KS, Kim KM, Park NG, Park YJ, Chang SH. Symmetric redox supercapacitor with conducting polyaniline electrodes. J Power Sources 2002;103:305–9. https://doi.org/10.1016/S0378-7753(01)00862-X.

[32] Arbizzani C, Mastragostino M, Soavi F. New trends in electrochemical supercapacitors. J Power Sources 2001;100:164–70. https://doi.org/10.1016/S0378-7753(01)00892-8.

[33] Chondath SK, Menamparambath MM. Interface-assisted synthesis: a gateway to effective nanostructure tuning of conducting polymers. Nanoscale Adv 2021;3:918–41. https://doi.org/10.1039/D0NA00940G.

[34] Zhong C, Deng Y, Hu W, Qiao J, Zhang L, Zhang J. A review of electrolyte materials and compositions for electrochemical supercapacitors. Chem Soc Rev 2015;44:7484–539. https://doi.org/10.1039/C5CS00303B.

[35] Tsuda T, Hussey CL. Electrochemical Applications of Room-Temperature Ionic Liquids. Electrochem Soc Interface 2007;16:42–9. https://doi.org/10.1149/2.f05071if.

[36] Taberna P-L, Simon P. Electrochemical Techniques. Supercapacitors 2013:111–30. https://doi.org/https://doi.org/10.1002/9783527646661.ch3.

[37] Frackowiak E, Béguin F. Carbon materials for the electrochemical storage of energy in capacitors. Carbon N Y 2001;39:937–50. https://doi.org/https://doi.org/10.1016/S0008-6223(00)00183-4.

[38] Stoller MD, Ruoff RS. Best practice methods for determining an electrode material's performance for ultracapacitors. Energy Environ Sci 2010;3:1294–

301. https://doi.org/10.1039/C0EE00074D.

[39] Gogotsi Y, Simon P. True Performance Metrics in Electrochemical Energy Storage. Science (80-) 2011;334:917 LP – 918. https://doi.org/10.1126/science.1213003.

[40] Ekaterina P, Francesco B, Xinliang F, Yi C, Yury G. Energy storage: The future enabled by nanomaterials. Science (80-) 2019;366:eaan8285. https://doi.org/10.1126/science.aan8285.

[41] Gogotsi Y. What Nano Can Do for Energy Storage. ACS Nano 2014;8:5369–71. https://doi.org/10.1021/nn503164x.

[42] Ates B, Koytepe S, Ulu A, Gurses C, Thakur VK. Chemistry, Structures, and Advanced Applications of Nanocomposites from Biorenewable Resources. Chem Rev 2020;120:9304–62. https://doi.org/10.1021/acs.chemrev.9b00553.

[43] Ebrahimi DYE-F. Application of Nanocomposites for Supercapacitors: Characteristics and Properties, Rijeka: IntechOpen; 2012, p. Ch. 12. https://doi.org/10.5772/50409.

[44] Sripakagorn A, Limwuthigraijirat N. Experimental assessment of fuel cell/supercapacitor hybrid system for scooters. Int J Hydrogen Energy 2009;34:6036–44. https://doi.org/https://doi.org/10.1016/j.ijhydene.2009.04.059.

[45] Wang L, Li X, Guo T, Yan X, Tay BK. Three-dimensional Ni(OH)2 nanoflakes/graphene/nickel foam electrode with high rate capability for supercapacitor applications. Int J Hydrogen Energy 2014;39:7876–84. https://doi.org/https://doi.org/10.1016/j.ijhydene.2014.03.067.

[46] Shin D, Lee K, Chang N. Fuel economy analysis of fuel cell and supercapacitor hybrid systems. Int J Hydrogen Energy 2016;41:1381–90. https://doi.org/https://doi.org/10.1016/j.ijhydene.2015.10.103.

[47] Harfman-Todorovic M, Chellappan M, Palma L, Enjeti P. The role of supercapacitors in designing fuel cell powered portable applications. 2008

IEEE Power Electron. Spec. Conf., 2008, p. 2465–72. https://doi.org/10.1109/PESC.2008.4592311.

[48] Unda JEZ, Roduner E. Reversible transient hydrogen storage in a fuel cell–supercapacitor hybrid device. Phys Chem Chem Phys 2012;14:3816–24. https://doi.org/10.1039/C2CP23140A.

[49] Falcao EHL, Wudl F. Carbon allotropes: Beyond graphite and diamond. J Chem Technol Biotechnol 2007;82:524–31. https://doi.org/10.1002/JCTB.1693.

[50] Gamby J, Taberna PL, Simon P, Fauvarque JF, Chesneau M. Studies and characterisations of various activated carbons used for carbon/carbon supercapacitors. J Power Sources 2001;101:109–16. https://doi.org/10.1016/S0378-7753(01)00707-8.

[51] Masarapu C, Zeng HF, Hung KH, Wei B. Effect of temperature on the capacitance of carbon nanotube supercapacitors. ACS Nano 2009;3:2199–206. https://doi.org/10.1021/NN900500N.

[52] Jost K, Stenger D, Perez CR, McDonough JK, Lian K, Gogotsi Y, et al. Knitted and screen printed carbon-fiber supercapacitors for applications in wearable electronics. Energy Environ Sci 2013;6:2698–705. https://doi.org/10.1039/C3EE40515J.

[53] Kalpana D, Renganathan NG, Pitchumani S. A new class of alkaline polymer gel electrolyte for carbon aerogel supercapacitors. J Power Sources 2006;157:621–3. https://doi.org/10.1016/j.jpowsour.2005.07.057.

[54] Brownson DAC, Banks CE. Fabricating graphene supercapacitors: Highlighting the impact of surfactants and moieties. Chem Commun 2012;48:1425–7. https://doi.org/10.1039/c1cc11276g.

[55] Lu W, Hartman R, Qu L, Dai L. Nanocomposite electrodes for high-performance supercapacitors. J Phys Chem Lett 2011;2:655–60. https://doi.org/10.1021/JZ200104N.

[56] Shokrieh MM, Rafiee R. Prediction of Young's modulus of graphene sheets and carbon nanotubes using nanoscale continuum mechanics approach. Mater Des 2010;31:790–5. https://doi.org/10.1016/j.matdes.2009.07.058.

[57] Zhang L, Zhao XS. Carbon-based materials as supercapacitor electrodes. Chem Soc Rev 2009;38:2520–31. https://doi.org/10.1039/B813846J.

[58] Huang F, Lou F, Chen D. Exploring aligned-carbon-nanotubes@polyaniline arrays on household al as supercapacitors. ChemSusChem 2012;5:888–95. https://doi.org/10.1002/CSSC.201100553.

[59] Dogru IB, Durukan MB, Turel O, Unalan HE. Flexible supercapacitor electrodes with vertically aligned carbon nanotubes grown on aluminum foils. Prog Nat Sci Mater Int 2016;26:232–6. https://doi.org/10.1016/j.pnsc.2016.05.011.

[60] Dörfler S, Felhösi I, Marek T, Thieme S, Althues H, Nyikos L, et al. High power supercap electrodes based on vertical aligned carbon nanotubes on aluminum. J Power Sources 2013;227:218–28. https://doi.org/10.1016/j.jpowsour.2012.11.068.

[61] Liatard S, Benhamouda K, Fournier A, Ramos R, Barchasz C, Dijon J. Vertically-aligned carbon nanotubes on aluminum as a light-weight positive electrode for lithium-polysulfide batteries. Chem Commun 2015;51:7749–52. https://doi.org/10.1039/C4CC08848D.

[62] Esconjauregui S, Bhardwaj S, Yang J, Castellarin-Cudia C, Xie R, D'Arsié L, et al. Carbon nanotube growth on conductors: Influence of the support structure and catalyst thickness. Carbon N Y 2014;73:13–24. https://doi.org/10.1016/j.carbon.2014.02.026.

[63] Lee CJ, Kim DW, Lee TJ, Choi YC, Park YS, Lee YH, et al. Synthesis of aligned carbon nanotubes using thermal chemical vapor deposition. Chem Phys Lett 1999;312:461–8. https://doi.org/10.1016/S0009-2614(99)01074-X.

[64] Meyyappan M, Delzeit L, Cassell A, Hash D. Carbon nanotube growth by

PECVD: A review. Plasma Sources Sci Technol 2003;12:205–16. https://doi.org/10.1088/0963-0252/12/2/312.

[65] Peng HB, Ristroph TG, Schurmann GM, King GM, Yoon J, Narayanamurti V, et al. Patterned growth of single-walled carbon nanotube arrays from a vapor-deposited Fe catalyst. Appl Phys Lett 2003;83:4238–40. https://doi.org/10.1063/1.1627935.

[66] Srivastava S, Kumar S, Vijay YK. Preparation and characterization of tantalum/polyaniline composite based chemiresistor type sensor for hydrogen gas sensing application. Int J Hydrogen Energy 2012;37:3825–32. https://doi.org/https://doi.org/10.1016/j.ijhydene.2011.04.155.

[67] Simotwo SK, Delre C, Kalra V. Supercapacitor Electrodes Based on High-Purity Electrospun Polyaniline and Polyaniline-Carbon Nanotube Nanofibers. ACS Appl Mater Interfaces 2016;8:21261–9. https://doi.org/10.1021/ACSAMI.6B03463.

[68] De A, Adhikary R, Datta J. Proactive role of carbon nanotube-polyaniline conjugate support for Pt nano-particles toward electro-catalysis of ethanol in fuel cell. Int J Hydrogen Energy 2017;42:25316–25. https://doi.org/10.1016/j.ijhydene.2017.08.073.

[69] Hui N, Chai F, Lin P, Song Z, Sun X, Li Y, et al. Electrodeposited Conducting Polyaniline Nanowire Arrays Aligned on Carbon Nanotubes Network for High Performance Supercapacitors and Sensors. Electrochim Acta 2016;199:234–41. https://doi.org/10.1016/j.electacta.2016.03.115.

[70] Zhang H, Cao G, Wang Z, Yang Y, Shi Z, Gu Z. Tube-covering-tube nanostructured polyaniline/carbon nanotube array composite electrode with high capacitance and superior rate performance as well as good cycling stability. Electrochem Commun 2008;10:1056–9. https://doi.org/10.1016/j.elecom.2008.05.007.

[71] Faraji M. Interlaced polyaniline/carbon nanotube nanocomposite co-electrodeposited on TiO2 nanotubes/Ti for high-performance supercapacitors.

J Solid State Electrochem 2018;22:677–84. https://doi.org/10.1007/S10008-017-3804-Z.

[72] Zhang J, Kong L Bin, Wang B, Luo YC, Kang L. In-situ electrochemical polymerization of multi-walled carbon nanotube/polyaniline composite films for electrochemical supercapacitors. Synth Met 2009;159:260–6. https://doi.org/10.1016/j.synthmet.2008.09.018.

[73] Aydinli A, Yuksel R, Unalan HE. Vertically aligned carbon nanotube – Polyaniline nanocomposite supercapacitor electrodes. Int J Hydrogen Energy 2018;43:18617–25. https://doi.org/https://doi.org/10.1016/j.ijhydene.2018.05.126.

[74] Yamashita T, Hayes P. Analysis of XPS spectra of Fe 2+ and Fe 3+ ions in oxide materials. Appl Surf Sci 2008;254:2441–9. https://doi.org/10.1016/j.apsusc.2007.09.063.

[75] Bachhav SG, Patil DR. Synthesis and characterization of polyaniline-multiwalled carbon nanotube nanocomposites and its electrical percolation behavior. Am J Mater Sci 2015;5:90–5.

[76] Chu CY, Tsai JT, Sun CL. Synthesis of PEDOT-modified graphene composite materials as flexible electrodes for energy storage and conversion applications. Int J Hydrogen Energy 2012;37:13880–6. https://doi.org/10.1016/j.ijhydene.2012.05.017.

[77] Chen Y, Cai K, Liu C, Song H, Yang X. High-Performance and Breathable Polypyrrole Coated Air-Laid Paper for Flexible All-Solid-State Supercapacitors. Adv Energy Mater 2017;7:1701247. https://doi.org/https://doi.org/10.1002/aenm.201701247.

[78] Abdelkader A, Karim N, Vallés C, Afroj S, Novoselov K, Yeates S. Ultraflexible and robust graphene supercapacitors printed on textiles for wearable electronics applications. 2D Mater 2017;4:35016. https://doi.org/10.1088/2053-1583/aa7d71.

[79] Yuksel R, Coskun S, Gunbas G, Cirpan A, Toppare L, Unalan HE. Silver Nanowire/Conducting Polymer Nanocomposite Electrochromic Supercapacitor Electrodes. J Electrochem Soc 2017;164:A721–7. https://doi.org/10.1149/2.0791704jes.

[80] Zhang Y-Z, Wang Y, Cheng T, Lai W-Y, Pang H, Huang W. Flexible supercapacitors based on paper substrates: a new paradigm for low-cost energy storage. Chem Soc Rev 2015;44:5181–99. https://doi.org/10.1039/C5CS00174A.

[81] Stoppa M, Chiolerio A. Wearable Electronics and Smart Textiles: A Critical Review. Sensors 2014;14. https://doi.org/10.3390/s140711957.

[82] Zeng W, Shu L, Li Q, Chen S, Wang F, Tao X-M. Fiber-Based Wearable Electronics: A Review of Materials, Fabrication, Devices, and Applications. Adv Mater 2014;26:5310–36. https://doi.org/https://doi.org/10.1002/adma.201400633.

[83] Tobjörk D, Österbacka R. Paper Electronics. Adv Mater 2011;23:1935–61. https://doi.org/https://doi.org/10.1002/adma.201004692.

[84] Nyholm L, Nyström G, Mihranyan A, Strømme M. Toward Flexible Polymer and Paper-Based Energy Storage Devices. Adv Mater 2011;23:3751–69. https://doi.org/https://doi.org/10.1002/adma.201004134.

[85] Guo R, Chen J, Yang B, Liu L, Su L, Shen B, et al. In-Plane Micro-Supercapacitors for an Integrated Device on One Piece of Paper. Adv Funct Mater 2017;27:1702394. https://doi.org/https://doi.org/10.1002/adfm.201702394.

[86] Hu L, Choi JW, Yang Y, Jeong S, La Mantia F, Cui L-F, et al. Highly conductive paper for energy-storage devices. Proc Natl Acad Sci 2009;106:21490 LP – 21494. https://doi.org/10.1073/pnas.0908858106.

[87] Wan C, Jiao Y, Li J. Flexible, highly conductive, and free-standing reduced graphene oxide/polypyrrole/cellulose hybrid papers for supercapacitor

electrodes. J Mater Chem A 2017;5:3819–31. https://doi.org/10.1039/C6TA04844G.

[88] Yuksel R, Unalan HE. Textile supercapacitors-based on MnO2/SWNT/conducting polymer ternary composites. Int J Energy Res 2015;39:2042–52. https://doi.org/https://doi.org/10.1002/er.3439.

[89] Hu S, Rajamani R, Yu X. Flexible solid-state paper based carbon nanotube supercapacitor. Appl Phys Lett 2012;100:104103. https://doi.org/10.1063/1.3691948.

[90] Yu J, Lu W, Smith JP, Booksh KS, Meng L, Huang Y, et al. A High Performance Stretchable Asymmetric Fiber-Shaped Supercapacitor with a Core-Sheath Helical Structure. Adv Energy Mater 2017;7:1600976. https://doi.org/https://doi.org/10.1002/aenm.201600976.

[91] Li L, Lou Z, Han W, Chen D, Jiang K, Shen G. Highly Stretchable Micro-Supercapacitor Arrays with Hybrid MWCNT/PANI Electrodes. Adv Mater Technol 2017;2:1600282. https://doi.org/https://doi.org/10.1002/admt.201600282.

[92] Li Z, Mi Y, Liu X, Liu S, Yang S, Wang J. Flexible graphene/MnO2 composite papers for supercapacitor electrodes. J Mater Chem 2011;21:14706–11. https://doi.org/10.1039/C1JM11941A.

[93] Meyyappan M. Nanostructured materials for supercapacitors. J Vac Sci Technol A 2013;31:50803. https://doi.org/10.1116/1.4802772.

[94] Stoller MD, Park S, Zhu Y, An J, Ruoff RS. Graphene-Based Ultracapacitors. Nano Lett 2008;8:3498–502. https://doi.org/10.1021/nl802558y.

[95] Park S, Ruoff RS. Chemical methods for the production of graphenes. Nat Nanotechnol 2009;4:217–24. https://doi.org/10.1038/nnano.2009.58.

[96] Weng Z, Su Y, Wang D-W, Li F, Du J, Cheng H-M. Graphene–Cellulose Paper Flexible Supercapacitors. Adv Energy Mater 2011;1:917–22. https://doi.org/https://doi.org/10.1002/aenm.201100312.

[97] Cong H-P, Ren X-C, Wang P, Yu S-H. Flexible graphene–polyaniline composite paper for high-performance supercapacitor. Energy Environ Sci 2013;6:1185–91. https://doi.org/10.1039/C2EE24203F.

[98] Shi Y, Pan L, Liu B, Wang Y, Cui Y, Bao Z, et al. Nanostructured conductive polypyrrole hydrogels as high-performance, flexible supercapacitor electrodes. J Mater Chem A 2014;2:6086–91. https://doi.org/10.1039/C4TA00484A.

[99] Huang Y, Li H, Wang Z, Zhu M, Pei Z, Xue Q, et al. Nanostructured Polypyrrole as a flexible electrode material of supercapacitor. Nano Energy 2016;22:422–38. https://doi.org/https://doi.org/10.1016/j.nanoen.2016.02.047.

[100] Zhang D, Zhang X, Chen Y, Yu P, Wang C, Ma Y. Enhanced capacitance and rate capability of graphene/polypyrrole composite as electrode material for supercapacitors. J Power Sources 2011;196:5990–6. https://doi.org/https://doi.org/10.1016/j.jpowsour.2011.02.090.

[101] Zhu C, Zhai J, Wen D, Dong S. Graphene oxide/polypyrrole nanocomposites: one-step electrochemical doping, coating and synergistic effect for energy storage. J Mater Chem 2012;22:6300–6. https://doi.org/10.1039/C2JM16699B.

[102] Hu H, Zhao Z, Zhou Q, Gogotsi Y, Qiu J. The role of microwave absorption on formation of graphene from graphite oxide. Carbon N Y 2012;50:3267–73. https://doi.org/https://doi.org/10.1016/j.carbon.2011.12.005.

[103] Wang Z-L, He X-J, Ye S-H, Tong Y-X, Li G-R. Design of Polypyrrole/Polyaniline Double-Walled Nanotube Arrays for Electrochemical Energy Storage. ACS Appl Mater Interfaces 2014;6:642–7. https://doi.org/10.1021/am404751k.

[104] Tang H, Wang J, Yin H, Zhao H, Wang D, Tang Z. Growth of Polypyrrole Ultrathin Films on MoS2 Monolayers as High-Performance Supercapacitor Electrodes. Adv Mater 2015;27:1117–23.

https://doi.org/https://doi.org/10.1002/adma.201404622.

[105] Hepel M. The Electrocatalytic Oxidation of Methanol at Finely Dispersed Platinum Nanoparticles in Polypyrrole Films. J Electrochem Soc 1998;145:124–34. https://doi.org/10.1149/1.1838224.

[106] Miao Y, Qi M, Zhan S, He N, Wang J, Yuan C. Construction of a Glucose Biosensor Immobilized With Glucose Oxidase in the Film of Polypyrrole Nanotubules. Anal Lett 1999;32:1287–99. https://doi.org/10.1080/00032719908542897.

[107] Yeh J-M, Chin C-P, Chang S. Enhanced corrosion protection coatings prepared from soluble electronically conductive polypyrrole-clay nanocomposite materials. J Appl Polym Sci 2003;88:3264–72. https://doi.org/10.1002/app.12146.

[108] Hong JS, Joo M, Vittal R, Kim K-J. Improved Photocurrent-Voltage Characteristics of Ru(II)-Dye Sensitized Solar Cells with Polypyrrole-Anchored TiO[sub 2] Films. J Electrochem Soc 2002;149:E493. https://doi.org/10.1149/1.1518486.

[109] Jurewicz K, Delpeux S, Bertagna V, Béguin F, Frackowiak E. Supercapacitors from nanotubes/polypyrrole composites. Chem Phys Lett 2001;347:36–40. https://doi.org/https://doi.org/10.1016/S0009-2614(01)01037-5.

[110] Xiao Q, Zhou X. The study of multiwalled carbon nanotube deposited with conducting polymer for supercapacitor. Electrochim Acta 2003;48:575–80. https://doi.org/https://doi.org/10.1016/S0013-4686(02)00727-2.

[111] Khomenko V, Frackowiak E, Béguin F. Determination of the specific capacitance of conducting polymer/nanotubes composite electrodes using different cell configurations. Electrochim Acta 2005;50:2499–506. https://doi.org/https://doi.org/10.1016/j.electacta.2004.10.078.

[112] An KH, Jeon KK, Heo JK, Lim SC, Bae DJ, Lee YH. High-Capacitance Supercapacitor Using a Nanocomposite Electrode of Single-Walled Carbon

Nanotube and Polypyrrole. J Electrochem Soc 2002;149:A1058. https://doi.org/10.1149/1.1491235.

[113] Kim J-H, Lee Y-S, Sharma AK, Liu CG. Polypyrrole/carbon composite electrode for high-power electrochemical capacitors. Electrochim Acta 2006;52:1727–32. https://doi.org/https://doi.org/10.1016/j.electacta.2006.02.059.

[114] Muthulakshmi B, Kalpana D, Pitchumani S, Renganathan NG. Electrochemical deposition of polypyrrole for symmetric supercapacitors. J Power Sources 2006;158:1533–7. https://doi.org/https://doi.org/10.1016/j.jpowsour.2005.10.013.

[115] He W, Li G, Zhang S, Wei Y, Wang J, Li Q, et al. Polypyrrole/Silver Coaxial Nanowire Aero-Sponges for Temperature-Independent Stress Sensing and Stress-Triggered Joule Heating. ACS Nano 2015;9:4244–51. https://doi.org/10.1021/acsnano.5b00626.

[116] Boota M, Anasori B, Voigt C, Zhao M-Q, Barsoum MW, Gogotsi Y. Pseudocapacitive Electrodes Produced by Oxidant-Free Polymerization of Pyrrole between the Layers of 2D Titanium Carbide (MXene). Adv Mater 2016;28:1517–22. https://doi.org/https://doi.org/10.1002/adma.201504705.

[117] Liu Y, Zhang Y, Ma G, Wang Z, Liu K, Liu H. Ethylene glycol reduced graphene oxide/polypyrrole composite for supercapacitor. Electrochim Acta 2013;88:519–25. https://doi.org/https://doi.org/10.1016/j.electacta.2012.10.082.

[118] Zhao Y, Liu J, Hu Y, Cheng H, Hu C, Jiang C, et al. Highly Compression-Tolerant Supercapacitor Based on Polypyrrole-mediated Graphene Foam Electrodes. Adv Mater 2013;25:591–5. https://doi.org/https://doi.org/10.1002/adma.201203578.

[119] Liangbing H, Wook CJ, Yuan Y, Sangmoo J, Fabio LM, Li-Feng C, et al. Highly conductive paper for energy-storage devices. Proc Natl Acad Sci 2009;106:21490–4. https://doi.org/10.1073/pnas.0908858106.

[120] Pääkkö M, Vapaavuori J, Silvennoinen R, Kosonen H, Ankerfors M, Lindström T, et al. Long and entangled native cellulose I nanofibers allow flexible aerogels and hierarchically porous templates for functionalities. Soft Matter 2008;4:2492–9. https://doi.org/10.1039/B810371B.

[121] Wang Z, Tammela P, Zhang P, Strømme M, Nyholm L. High areal and volumetric capacity sustainable all-polymer paper-based supercapacitors. J Mater Chem A 2014;2:16761–9. https://doi.org/10.1039/C4TA03724C.

[122] Gui Z, Zhu H, Gillette E, Han X, Rubloff GW, Hu L, et al. Natural Cellulose Fiber as Substrate for Supercapacitor. ACS Nano 2013;7:6037–46. https://doi.org/10.1021/nn401818t.

[123] Yuksel R, Uysal N, Aydinli A, Unalan HE. Paper Based, Expanded Graphite/Polypyrrole Nanocomposite Supercapacitors Free from Binders and Current Collectors. J Electrochem Soc 2018;165:A283–90. https://doi.org/10.1149/2.1051802jes.

[124] Damien V, Jieun Y, Jacob K, Raymond F, Calvin L, Young JH, et al. High-quality graphene via microwave reduction of solution-exfoliated graphene oxide. Science (80-) 2016;353:1413–6. https://doi.org/10.1126/science.aah3398.

[125] Zhu Y, Murali S, Stoller MD, Velamakanni A, Piner RD, Ruoff RS. Microwave assisted exfoliation and reduction of graphite oxide for ultracapacitors. Carbon N Y 2010;48:2118–22. https://doi.org/https://doi.org/10.1016/j.carbon.2010.02.001.

[126] Gokoglan TC, Kesik M, Soylemez S, Yuksel R, Unalan HE, Toppare L. Paper Based Glucose Biosensor Using Graphene Modified with a Conducting Polymer and Gold Nanoparticles. J Electrochem Soc 2017;164:G59–64. https://doi.org/10.1149/2.0791706jes.

[127] Yuksel R, Alpugan E, Unalan HE. Coaxial silver nanowire/polypyrrole nanocomposite supercapacitors. Org Electron 2018;52:272–80. https://doi.org/https://doi.org/10.1016/j.orgel.2017.10.012.

[128] Aktekin B, Çakmak G, Öztürk T. Induction thermal plasma synthesis of Mg2Ni nanoparticles. Int J Hydrogen Energy 2014;39:9859–64. https://doi.org/10.1016/j.ijhydene.2014.02.066.

[129] Zhang H, Cao T, Cheng Y. Preparation of few-layer graphene nanosheets by radio-frequency induction thermal plasma. Carbon N Y 2015;86:38–45. https://doi.org/https://doi.org/10.1016/j.carbon.2015.01.021.

[130] Pristavita R, Meunier J-L, Berk D. Carbon Nano-Flakes Produced by an Inductively Coupled Thermal Plasma System for Catalyst Applications. Plasma Chem Plasma Process 2011;31:393–403. https://doi.org/10.1007/s11090-011-9289-0.

[131] Brousse T, Bélanger D, Long JW. To Be or Not To Be Pseudocapacitive? J Electrochem Soc 2015;162:A5185–9. https://doi.org/10.1149/2.0201505jes.

[132] Lee HY, Goodenough JB. Supercapacitor Behavior with KCl Electrolyte. J Solid State Chem 1999;144:220–3. https://doi.org/https://doi.org/10.1006/jssc.1998.8128.

[133] Wei W, Cui X, Chen W, Ivey DG. Manganese oxide-based materials as electrochemical supercapacitor electrodes. Chem Soc Rev 2011;40:1697–721. https://doi.org/10.1039/C0CS00127A.

[134] Devaraj S, Munichandraiah N. Effect of Crystallographic Structure of MnO2 on Its Electrochemical Capacitance Properties. J Phys Chem C 2008;112:4406–17. https://doi.org/10.1021/jp7108785.

[135] Donnet JB. Carbon Black: Science and Technology, Second Edition. Taylor & Francis; 1993.

[136] Arduini F, Giorgio F Di, Amine A, Cataldo F, Moscone D, Palleschi G. Electroanalytical Characterization of Carbon Black Nanomaterial Paste Electrode: Development of Highly Sensitive Tyrosinase Biosensor for Catechol Detection. Anal Lett 2010;43:1688–702. https://doi.org/10.1080/00032711003653932.

[137] Li C, Shi G. Functional Gels Based on Chemically Modified Graphenes. Adv Mater 2014;26:3992–4012. https://doi.org/10.1002/adma.201306104.

[138] Xu Y, Sheng K, Li C, Shi G. Self-Assembled Graphene Hydrogel via a One-Step Hydrothermal Process. ACS Nano 2010;4:4324–30. https://doi.org/10.1021/nn101187z.

[139] Tan C, Zhang H. Two-dimensional transition metal dichalcogenide nanosheet-based composites. Chem Soc Rev 2015;44:2713–31. https://doi.org/10.1039/C4CS00182F.

[140] Acerce M, Voiry D, Chhowalla M. Metallic 1T phase MoS2 nanosheets as supercapacitor electrode materials. Nat Nanotechnol 2015;10:313–8. https://doi.org/10.1038/nnano.2015.40.

[141] Huang X, Zeng Z, Zhang H. Metal dichalcogenide nanosheets: preparation, properties and applications. Chem Soc Rev 2013;42:1934–46. https://doi.org/10.1039/C2CS35387C.

[142] Valeria N, Manish C, G. KM, S. SM, N. CJ. Liquid Exfoliation of Layered Materials. Science (80-) 2013;340:1226419. https://doi.org/10.1126/science.1226419.

[143] Tang Q, Jiang D. Stabilization and Band-Gap Tuning of the 1T-MoS2 Monolayer by Covalent Functionalization. Chem Mater 2015;27:3743–8. https://doi.org/10.1021/acs.chemmater.5b00986.

[144] Marcano DC, Kosynkin D V, Berlin JM, Sinitskii A, Sun Z, Slesarev A, et al. Improved Synthesis of Graphene Oxide. ACS Nano 2010;4:4806–14. https://doi.org/10.1021/nn1006368.

[145] Doğan Ö. Development of graphene oxide based aerogels. Middle East Technical University, 2017.

[146] Al-Gaashani R, Najjar A, Zakaria Y, Mansour S, Atieh MA. XPS and structural studies of high quality graphene oxide and reduced graphene oxide prepared by different chemical oxidation methods. Ceram Int 2019;45:14439–

48. https://doi.org/https://doi.org/10.1016/j.ceramint.2019.04.165.

[147] De Levie R. On porous electrodes in electrolyte solutions: I. Capacitance effects. Electrochim Acta 1963;8:751–80.

[148] Zhang K, Feng Y, Wang F, Yang Z, Wang J. Two dimensional hexagonal boron nitride (2D-hBN): synthesis, properties and applications. J Mater Chem C 2017;5:11992–2022. https://doi.org/10.1039/C7TC04300G.

[149] Wang X, Pakdel A, Zhang J, Weng Q, Zhai T, Zhi C, et al. Large-surface-area BN nanosheets and their utilization in polymeric composites with improved thermal and dielectric properties. Nanoscale Res Lett 2012;7:662. https://doi.org/10.1186/1556-276X-7-662.

[150] Wu X, Zhao Z, Sun Y, Li H, Wang Y, Zhang C, et al. Boron Nitride Nanoparticles with High Specific Surface Area: Preparation by a Calcination Method and Application in Epoxy Resin. J Inorg Organomet Polym Mater 2017;27:1142–7. https://doi.org/10.1007/s10904-017-0540-x.

[151] Saha S, Jana M, Khanra P, Samanta P, Koo H, Murmu NC, et al. Band Gap Engineering of Boron Nitride by Graphene and Its Application as Positive Electrode Material in Asymmetric Supercapacitor Device. ACS Appl Mater Interfaces 2015;7:14211–22. https://doi.org/10.1021/acsami.5b03562.

[152] Khan AF, Down MP, Smith GC, Foster CW, Banks CE. Surfactant-exfoliated 2D hexagonal boron nitride (2D-hBN): role of surfactant upon the electrochemical reduction of oxygen and capacitance applications. J Mater Chem A 2017;5:4103–13. https://doi.org/10.1039/C6TA09999H.

[153] Huang Z, Qi X, Yang H, He C, Wei X, Peng X, et al. Band-gap engineering of the h-BN/MoS2/h-BN sandwich heterostructure under an external electric field. J Phys D Appl Phys 2015;48:205302. https://doi.org/10.1088/0022-3727/48/20/205302.

[154] Yan A, Velasco J, Kahn S, Watanabe K, Taniguchi T, Wang F, et al. Direct Growth of Single- and Few-Layer MoS2 on h-BN with Preferred Relative

Rotation Angles. Nano Lett 2015;15:6324–31. https://doi.org/10.1021/acs.nanolett.5b01311.

[155] Wang J, Yao Q, Huang C-W, Zou X, Liao L, Chen S, et al. High Mobility MoS2 Transistor with Low Schottky Barrier Contact by Using Atomic Thick h-BN as a Tunneling Layer. Adv Mater 2016;28:8302–8. https://doi.org/https://doi.org/10.1002/adma.201602757.

[156] Jeong H, Bang S, Oh HM, Jeong HJ, An S-J, Han GH, et al. Semiconductor–Insulator–Semiconductor Diode Consisting of Monolayer MoS2, h-BN, and GaN Heterostructure. ACS Nano 2015;9:10032–8. https://doi.org/10.1021/acsnano.5b04233.

[157] Lee G-H, Yu Y-J, Cui X, Petrone N, Lee C-H, Choi MS, et al. Flexible and Transparent MoS2 Field-Effect Transistors on Hexagonal Boron Nitride-Graphene Heterostructures. ACS Nano 2013;7:7931–6. https://doi.org/10.1021/nn402954e.

[158] Wang S, Wang X, Warner JH. All Chemical Vapor Deposition Growth of MoS2:h-BN Vertical van der Waals Heterostructures. ACS Nano 2015;9:5246–54. https://doi.org/10.1021/acsnano.5b00655.

[159] Byun S, Kim JH, Song SH, Lee M, Park J-J, Lee G, et al. Ordered, Scalable Heterostructure Comprising Boron Nitride and Graphene for High-Performance Flexible Supercapacitors. Chem Mater 2016;28:7750–6. https://doi.org/10.1021/acs.chemmater.6b02947.

[160] Schütter C, Pohlmann S, Balducci A. Industrial Requirements of Materials for Electrical Double Layer Capacitors: Impact on Current and Future Applications. Adv Energy Mater 2019;9:1900334. https://doi.org/10.1002/aenm.201900334.

[161] Naguib M, Kurtoglu M, Presser V, Lu J, Niu J, Heon M, et al. Two-Dimensional Nanocrystals Produced by Exfoliation of Ti3AlC2. Adv Mater 2011;23:4248–53. https://doi.org/10.1002/adma.201102306.

[162] Naguib M, Mashtalir O, Carle J, Presser V, Lu J, Hultman L, et al. Two-Dimensional Transition Metal Carbides. ACS Nano 2012;6:1322–31. https://doi.org/10.1021/nn204153h.

[163] Gogotsi Y, Huang Q. MXenes: Two-Dimensional Building Blocks for Future Materials and Devices. ACS Nano 2021;15:5775–80. https://doi.org/10.1021/acsnano.1c03161.

[164] Anasori B, Lukatskaya MR, Gogotsi Y. 2D metal carbides and nitrides (MXenes) for energy storage. Nat Rev Mater 2017;2:16098.

[165] Sun W, Shah SA, Chen Y, Tan Z, Gao H, Habib T, et al. Electrochemical etching of Ti2AlC to Ti2CTx (MXene) in low-concentration hydrochloric acid solution. J Mater Chem A 2017;5:21663–8. https://doi.org/10.1039/C7TA05574A.

[166] Yang S, Zhang P, Wang F, Ricciardulli AG, Lohe MR, Blom PWM, et al. Fluoride-Free Synthesis of Two-Dimensional Titanium Carbide (MXene) Using A Binary Aqueous System. Angew Chemie Int Ed 2018;57:15491–5. https://doi.org/https://doi.org/10.1002/anie.201809662.

[167] Mathis TS, Maleski K, Goad A, Sarycheva A, Anayee M, Foucher AC, et al. Modified MAX Phase Synthesis for Environmentally Stable and Highly Conductive Ti3C2 MXene. ACS Nano 2021;15:6420–9. https://doi.org/10.1021/acsnano.0c08357.

[168] Wang X, Bannenberg L. Design and characterization of 2D MXene-based electrode with high-rate capability. MRS Bull 2021;46:755–66. https://doi.org/10.1557/s43577-021-00150-z.

[169] Anasori B, Gogotsi Y. 2D Metal Carbides and Nitrides (MXenes): Structure, Properties and Applications. Springer International Publishing; 2019.

[170] Lukatskaya MR, Kota S, Lin Z, Zhao M-Q, Shpigel N, Levi MD, et al. Ultra-high-rate pseudocapacitive energy storage in two-dimensional transition metal carbides. Nat Energy 2017;2:17105.

https://doi.org/10.1038/nenergy.2017.105.

[171] Wang X, Mathis TS, Li K, Lin Z, Vlcek L, Torita T, et al. Influences from solvents on charge storage in titanium carbide MXenes. Nat Energy 2019;4:241–8. https://doi.org/10.1038/s41560-019-0339-9.

[172] Wang X, Bak S-M, Han M, Shuck CE, McHugh C, Li K, et al. Surface Redox Pseudocapacitance of Partially Oxidized Titanium Carbide MXene in Water-in-Salt Electrolyte. ACS Energy Lett 2021:30–5. https://doi.org/10.1021/acsenergylett.1c02262.

[173] Jiang Q, Lei Y, Liang H, Xi K, Xia C, Alshareef HN. Review of MXene electrochemical microsupercapacitors. Energy Storage Mater 2020;27:78–95. https://doi.org/https://doi.org/10.1016/j.ensm.2020.01.018.

[174] Peng Y-Y, Akuzum B, Kurra N, Zhao M-Q, Alhabeb M, Anasori B, et al. All-MXene (2D titanium carbide) solid-state microsupercapacitors for on-chip energy storage. Energy Environ Sci 2016;9:2847–54. https://doi.org/10.1039/C6EE01717G.

[175] Zhang C (John), McKeon L, Kremer MP, Park S-H, Ronan O, Seral-Ascaso A, et al. Additive-free MXene inks and direct printing of micro-supercapacitors. Nat Commun 2019;10:1795. https://doi.org/10.1038/s41467-019-09398-1.

[176] Wang X, Zhi C, Weng Q, Bando Y, Golberg D. Boron Nitride Nanosheets: novel Syntheses and Applications in polymeric Composites. J Phys Conf Ser 2013;471:12003. https://doi.org/10.1088/1742-6596/471/1/012003.

[177] Lei W, Portehault D, Liu D, Qin S, Chen Y. Porous boron nitride nanosheets for effective water cleaning. Nat Commun 2013;4:1777. https://doi.org/10.1038/ncomms2818.

[178] Lei W, Mochalin VN, Liu D, Qin S, Gogotsi Y, Chen Y. Boron nitride colloidal solutions, ultralight aerogels and freestanding membranes through one-step exfoliation and functionalization. Nat Commun 2015;6:8849.

https://doi.org/10.1038/ncomms9849.

[179] Gilshteyn EP, Amanbayev D, Anisimov AS, Kallio T, Nasibulin AG. All-nanotube stretchable supercapacitor with low equivalent series resistance. Sci Rep 2017;7:17449. https://doi.org/10.1038/s41598-017-17801-4.

[180] Yang W, Byun JJ, Yang J, Moissinac FP, Ma Y, Ding H, et al. All-In-One MXene–Boron Nitride–MXene "OREO" with Vertically Aligned Channels for Flexible Structural Supercapacitor Design. ACS Appl Energy Mater 2021. https://doi.org/10.1021/acsaem.1c01240.

[181] Kyerematen NA, Brousse T, Pech D. Microsupercapacitors as miniaturized energy-storage components for on-chip electronics. Nat Nanotechnol 2017;12:7–15. https://doi.org/10.1038/nnano.2016.196.

[182] Makino S, Yamauchi Y, Sugimoto W. Synthesis of electro-deposited ordered mesoporous RuOx using lyotropic liquid crystal and application toward micro-supercapacitors. J Power Sources 2013;227:153–60. https://doi.org/https://doi.org/10.1016/j.jpowsour.2012.11.032.

[183] Dinh TM, Armstrong K, Guay D, Pech D. High-resolution on-chip supercapacitors with ultra-high scan rate ability. J Mater Chem A 2014;2:7170–4. https://doi.org/10.1039/C4TA00640B.

[184] Shekhirev M, Shuck CE, Sarycheva A, Gogotsi Y. Characterization of MXenes at every step, from their precursors to single flakes and assembled films. Prog Mater Sci 2021;120:100757. https://doi.org/https://doi.org/10.1016/j.pmatsci.2020.100757.

[185] Sarycheva A, Polemi A, Liu Y, Dandekar K, Anasori B, Gogotsi Y. 2D titanium carbide (MXene) for wireless communication. Sci Adv 2018;4:eaau0920. https://doi.org/10.1126/sciadv.aau0920.

[186] Wang X, Mathis TS, Sun Y, Tsai W-Y, Shpigel N, Shao H, et al. Titanium Carbide MXene Shows an Electrochemical Anomaly in Water-in-Salt Electrolytes. ACS Nano 2021;15:15274–84.

https://doi.org/10.1021/acsnano.1c06027.

[187] Le Comte A, Reynier Y, Vincens C, Leys C, Azaïs P. First prototypes of hybrid potassium-ion capacitor (KIC): An innovative, cost-effective energy storage technology for transportation applications. J Power Sources 2017;363:34–43.
https://doi.org/https://doi.org/10.1016/j.jpowsour.2017.07.005.

APPENDICES

A. Supporting Information for Chapter 7

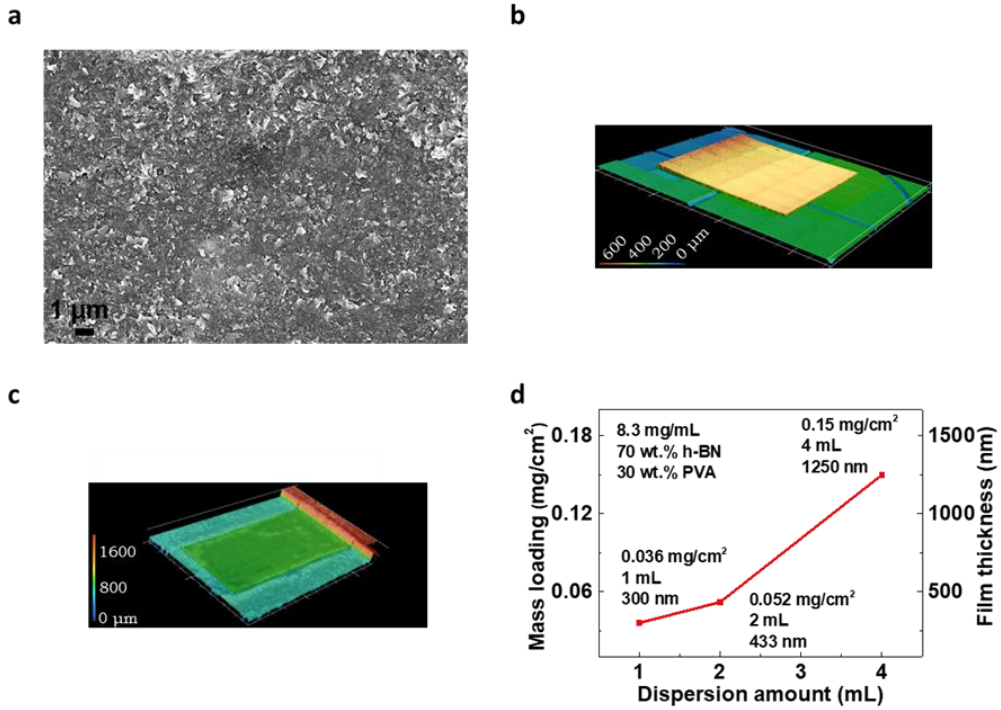

Figure A.1. (a) Top-view SEM image of h-BN coating without PVA, (b) 3D image of $Ti_3C_2T_x$ film, c) 3D image of h-BN film, and (d) h-BN dispersion amount versus mass loading and thickness data of the coatings.

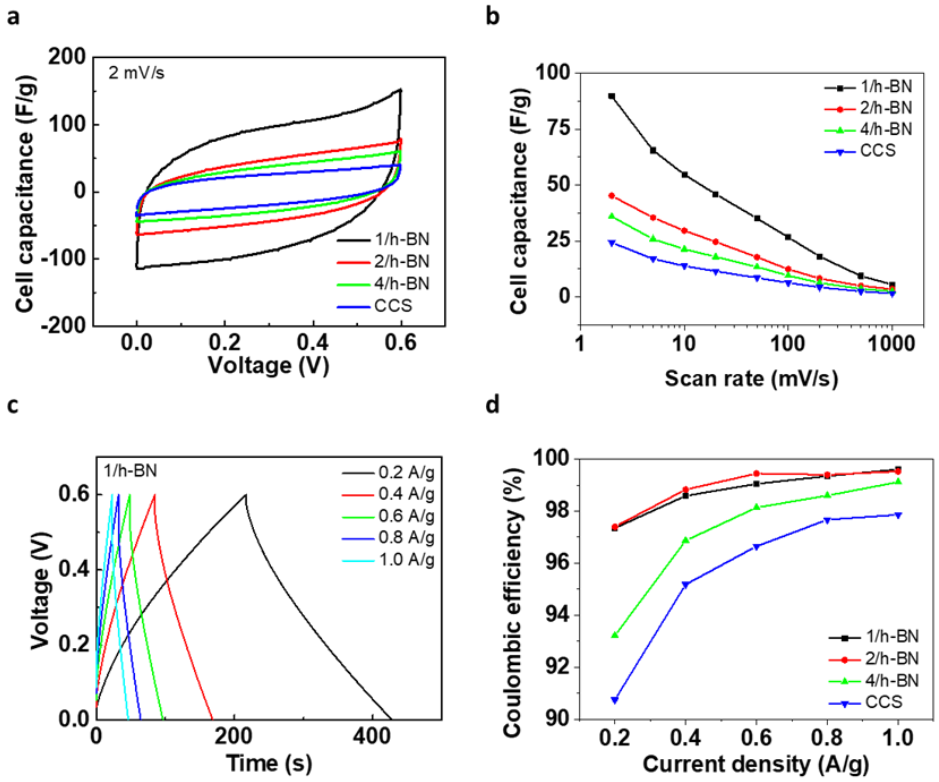

Figure A.2. (a) Cell capacitance comparison of the devices by CV test, (b) cell capacitance versus scan rate data of the devices, (c) GCD curves of 1/h-BN at different current densities, and (d) Coulombic efficiency versus current density data of the devices.

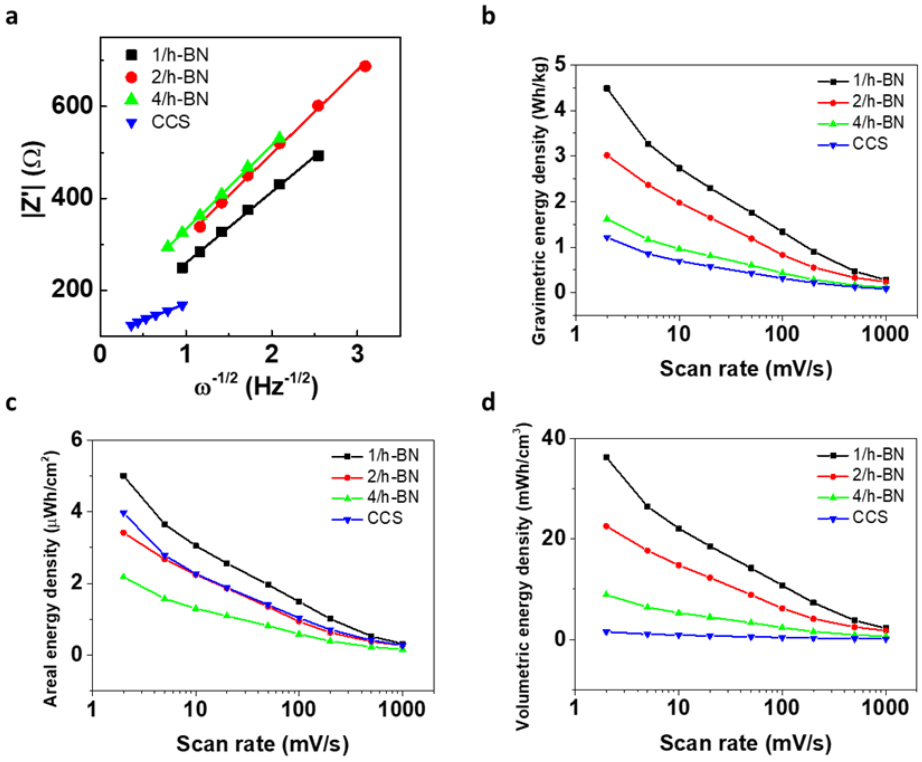

Figure A.3. (a) Linear fit demonstrating the relationship between the real part of impedance (Z') and frequency to the power of -0.5 ($\omega^{-1/2}$) in the Warburg region, (b) gravimetric energy density versus scan rate, (c) areal energy density versus scan rate, and (d) volumetric energy density versus scan rate data of the devices.

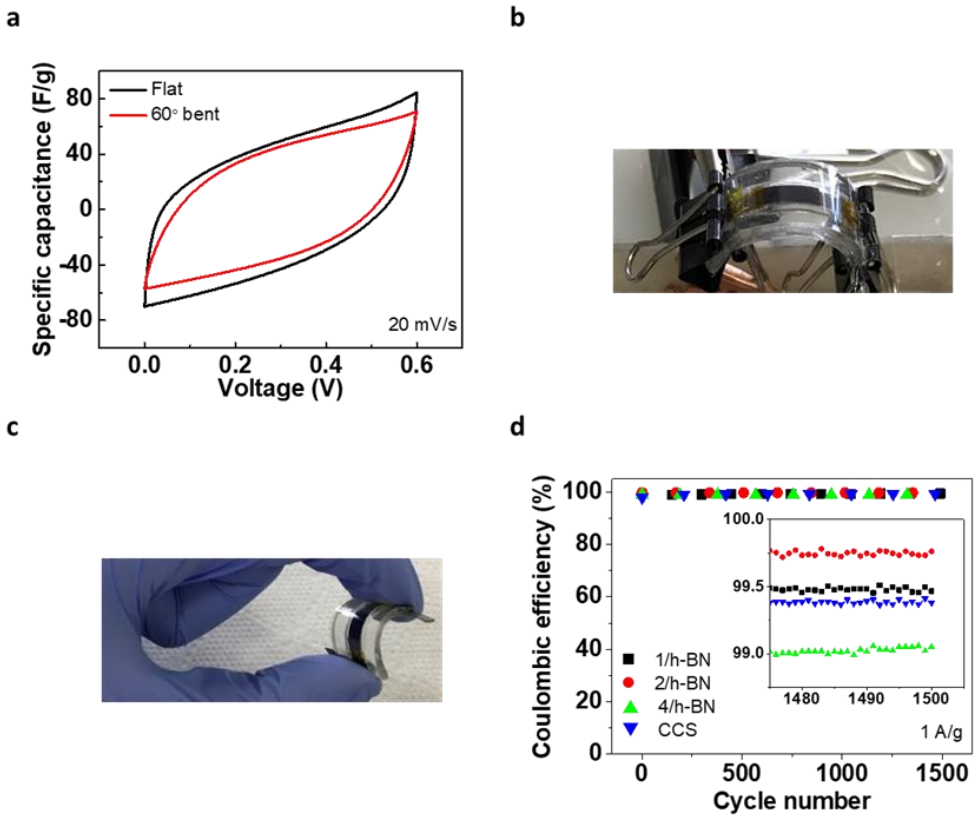

Figure A.4. (a) CV curves of flat and 60° bent forms of 1/h-BN at 20 mV/s, (b) photograph of a flexible device while testing, (c) photograph of the same flexible device when bent by hand, and (d) Coulombic efficiency versus cycle number data of the devices.

B. Permission Licenses

CCC | Marketplace™

This is a License Agreement between Alptekin AYDINLI ("User") and Copyright Clearance Center, Inc. ("CCC") on behalf of the Rightsholder identified in the order details below. The license consists of the order details, the CCC Terms and Conditions below, and any Rightsholder Terms and Conditions which are included below.

All payments must be made in full to CCC in accordance with the CCC Terms and Conditions below.

Order Date	28-Feb-2022	Type of Use	Republish in a thesis/dissertation
Order License ID	1193909-1		
ISSN	0360-3199	Publisher	PERGAMON
		Portion	Chapter/article

LICENSED CONTENT

Publication Title	International journal of hydrogen energy	Rightsholder	Elsevier Science & Technology Journals
Article Title	Vertically aligned carbon nanotube – Polyaniline nanocomposite supercapacitor electrodes	Publication Type	Journal
		Start Page	18617
		End Page	18625
Author/Editor	INTERNATIONAL ASSOCIATION FOR HYDROGEN ENERGY.	Issue	40
		Volume	43
Date	01/01/1976		
Language	English		
Country	United Kingdom of Great Britain and Northern Ireland		

REQUEST DETAILS

Portion Type	Chapter/article	Rights Requested	Main product
Page range(s)	18617-18625	Distribution	Worldwide
Total number of pages	9	Translation	Original language of publication
Format (select all that apply)	Print, Electronic	Copies for the disabled?	No
Who will republish the content?	Author of requested content	Minor editing privileges?	No
Duration of Use	Life of current edition	Incidental promotional use?	No
Lifetime Unit Quantity	Up to 499	Currency	USD

NEW WORK DETAILS

Title	DEVELOPMENT OF NANOCOMPOSITE ELECTRODES AND SEPARATORS FOR SUPERCAPACITORS	Institution name	Middle East Technical University
		Expected presentation date	2022-03-10
Instructor name	Alptekin AYDINLI		

ADDITIONAL DETAILS

Order reference number	N/A	The requesting person / organization to appear on the license	Alptekin AYDINLI

REUSE CONTENT DETAILS

Title, description or numeric reference of the portion(s)	All of the article	Title of the article/chapter the portion is from	Vertically aligned carbon nanotube – Polyaniline nanocomposite supercapacitor electrodes
Editor of portion(s)	Yuksel, Recep; Unalan, Husnu Emrah; Aydinli, Alptekin	Author of portion(s)	Yuksel, Recep; Unalan, Husnu Emrah; Aydinli, Alptekin
Volume of serial or monograph	43	Issue, if republishing an article from a serial	40
Page or page range of portion	18617-18625	Publication date of portion	2018-06-01

RIGHTSHOLDER TERMS AND CONDITIONS

Elsevier publishes Open Access articles in both its Open Access journals and via its Open Access articles option in subscription journals, for which an author selects a user license permitting certain types of reuse without permission. Before proceeding please check if the article is Open Access on **http://www.sciencedirect.com** and refer to the user license for the individual article. Any reuse not included in the user license terms will require permission. You must always fully and appropriately credit the author and source. If any part of the material to be used (for example, figures) has appeared in the Elsevier publication for which you are seeking permission, with credit or acknowledgement to another source it is the responsibility of the user to ensure their reuse complies with the terms and conditions determined by the rights holder. Please contact **permissions@elsevier.com** with any queries.

CCC Terms and Conditions

1. Description of Service; Defined Terms. This Republication License enables the User to obtain licenses for republication of one or more copyrighted works as described in detail on the relevant Order Confirmation (the "Work(s)"). Copyright Clearance Center, Inc. ("CCC") grants licenses through the Service on behalf of the rightsholder identified on the Order Confirmation (the "Rightsholder"). "Republication", as used herein, generally means the inclusion of a Work, in whole or in part, in a new work or works, also as described on the Order Confirmation. "User", as used herein, means the person or entity making such republication.

2. The terms set forth in the relevant Order Confirmation, and any terms set by the Rightsholder with respect to a particular Work, govern the terms of use of Works in connection with the Service. By using the Service, the person transacting for a republication license on behalf of the User represents and warrants that he/she/it (a) has been duly authorized by the User to accept, and hereby does accept, all such terms and conditions on behalf of User, and (b) shall inform User of all such terms and conditions. In the event such person is a "freelancer" or other third party independent of User and CCC, such party shall be deemed jointly a "User" for purposes of these terms and conditions. In any event, User shall be deemed to have accepted and agreed to all such terms and conditions if User republishes the Work in any fashion.

3. Scope of License; Limitations and Obligations.

   3.1. All Works and all rights therein, including copyright rights, remain the sole and exclusive property of the Rightsholder. The license created by the exchange of an Order Confirmation (and/or any invoice) and payment by User of the full amount set forth on that document includes only those rights expressly set forth in the Order Confirmation and in these terms and conditions, and conveys no other rights in the Work(s) to User. All rights not expressly granted are hereby reserved.

   3.2. General Payment Terms: You may pay by credit card or through an account with us payable at the end of the month. If you and we agree that you may establish a standing account with CCC, then the following terms apply: Remit Payment to: Copyright Clearance Center, 29118 Network Place, Chicago, IL 60673-1291. Payments Due: Invoices are payable upon their delivery to you (or upon our notice to you that they are available to you for downloading). After 30 days, outstanding amounts will be subject to a service charge of 1-1/2% per month or, if less, the maximum rate allowed by applicable law. Unless otherwise specifically set forth in the Order Confirmation or in a separate written agreement signed by CCC, invoices are due and payable on "net 30" terms. While User may exercise the rights licensed immediately upon issuance of the Order Confirmation, the license is automatically revoked and is null and void, as if it had never been issued, if complete payment for the license is not received on a timely basis either from User directly or through a payment agent, such as a credit card company.

3.3. Unless otherwise provided in the Order Confirmation, any grant of rights to User (i) is "one-time" (including the editions and product family specified in the license), (ii) is non-exclusive and non-transferable and (iii) is subject to any and all limitations and restrictions (such as, but not limited to, limitations on duration of use or circulation) included in the Order Confirmation or invoice and/or in these terms and conditions. Upon completion of the licensed use, User shall either secure a new permission for further use of the Work(s) or immediately cease any new use of the Work(s) and shall render inaccessible (such as by deleting or by removing or severing links or other locators) any further copies of the Work (except for copies printed on paper in accordance with this license and still in User's stock at the end of such period).

3.4. In the event that the material for which a republication license is sought includes third party materials (such as photographs, illustrations, graphs, inserts and similar materials) which are identified in such material as having been used by permission, User is responsible for identifying, and seeking separate licenses (under this Service or otherwise) for, any of such third party materials; without a separate license, such third party materials may not be used.

3.5. Use of proper copyright notice for a Work is required as a condition of any license granted under the Service. Unless otherwise provided in the Order Confirmation, a proper copyright notice will read substantially as follows: "Republished with permission of [Rightsholder's name], from [Work's title, author, volume, edition number and year of copyright]; permission conveyed through Copyright Clearance Center, Inc. " Such notice must be provided in a reasonably legible font size and must be placed either immediately adjacent to the Work as used (for example, as part of a by-line or footnote but not as a separate electronic link) or in the place where substantially all other credits or notices for the new work containing the republished Work are located. Failure to include the required notice results in loss to the Rightsholder and CCC, and the User shall be liable to pay liquidated damages for each such failure equal to twice the use fee specified in the Order Confirmation, in addition to the use fee itself and any other fees and charges specified.

3.6. User may only make alterations to the Work if and as expressly set forth in the Order Confirmation. No Work may be used in any way that is defamatory, violates the rights of third parties (including such third parties' rights of copyright, privacy, publicity, or other tangible or intangible property), or is otherwise illegal, sexually explicit or obscene. In addition, User may not conjoin a Work with any other material that may result in damage to the reputation of the Rightsholder. User agrees to inform CCC if it becomes aware of any infringement of any rights in a Work and to cooperate with any reasonable request of CCC or the Rightsholder in connection therewith.

4. Indemnity. User hereby indemnifies and agrees to defend the Rightsholder and CCC, and their respective employees and directors, against all claims, liability, damages, costs and expenses, including legal fees and expenses, arising out of any use of a Work beyond the scope of the rights granted herein, or any use of a Work which has been altered in any unauthorized way by User, including claims of defamation or infringement of rights of copyright, publicity, privacy or other tangible or intangible property.

5. Limitation of Liability. UNDER NO CIRCUMSTANCES WILL CCC OR THE RIGHTSHOLDER BE LIABLE FOR ANY DIRECT, INDIRECT, CONSEQUENTIAL OR INCIDENTAL DAMAGES (INCLUDING WITHOUT LIMITATION DAMAGES FOR LOSS OF BUSINESS PROFITS OR INFORMATION, OR FOR BUSINESS INTERRUPTION) ARISING OUT OF THE USE OR INABILITY TO USE A WORK, EVEN IF ONE OF THEM HAS BEEN ADVISED OF THE POSSIBILITY OF SUCH DAMAGES. In any event, the total liability of the Rightsholder and CCC (including their respective employees and directors) shall not exceed the total amount actually paid by User for this license. User assumes full liability for the actions and omissions of its principals, employees, agents, affiliates, successors and assigns.

6. Limited Warranties. THE WORK(S) AND RIGHT(S) ARE PROVIDED "AS IS". CCC HAS THE RIGHT TO GRANT TO USER THE RIGHTS GRANTED IN THE ORDER CONFIRMATION DOCUMENT. CCC AND THE RIGHTSHOLDER DISCLAIM ALL OTHER WARRANTIES RELATING TO THE WORK(S) AND RIGHT(S), EITHER EXPRESS OR IMPLIED, INCLUDING WITHOUT LIMITATION IMPLIED WARRANTIES OF MERCHANTABILITY OR FITNESS FOR A PARTICULAR PURPOSE. ADDITIONAL RIGHTS MAY BE REQUIRED TO USE ILLUSTRATIONS, GRAPHS, PHOTOGRAPHS, ABSTRACTS, INSERTS OR OTHER PORTIONS OF THE WORK (AS OPPOSED TO THE ENTIRE WORK) IN A MANNER CONTEMPLATED BY USER; USER UNDERSTANDS AND AGREES THAT NEITHER CCC NOR THE RIGHTSHOLDER MAY HAVE SUCH ADDITIONAL RIGHTS TO GRANT.

7. Effect of Breach. Any failure by User to pay any amount when due, or any use by User of a Work beyond the scope of the license set forth in the Order Confirmation and/or these terms and conditions, shall be a material breach of the license created by the Order Confirmation and these terms and conditions. Any breach not cured within 30 days of written notice thereof shall result in immediate termination of such license without further notice. Any unauthorized

(but licensable) use of a Work that is terminated immediately upon notice thereof may be liquidated by payment of the Rightsholder's ordinary license price therefor; any unauthorized (and unlicensable) use that is not terminated immediately for any reason (including, for example, because materials containing the Work cannot reasonably be recalled) will be subject to all remedies available at law or in equity, but in no event to a payment of less than three times the Rightsholder's ordinary license price for the most closely analogous licensable use plus Rightsholder's and/or CCC's costs and expenses incurred in collecting such payment.

8. Miscellaneous.

8.1. User acknowledges that CCC may, from time to time, make changes or additions to the Service or to these terms and conditions, and CCC reserves the right to send notice to the User by electronic mail or otherwise for the purposes of notifying User of such changes or additions; provided that any such changes or additions shall not apply to permissions already secured and paid for.

8.2. Use of User-related information collected through the Service is governed by CCC's privacy policy, available online here:https://marketplace.copyright.com/rs-ui-web/mp/privacy-policy

8.3. The licensing transaction described in the Order Confirmation is personal to User. Therefore, User may not assign or transfer to any other person (whether a natural person or an organization of any kind) the license created by the Order Confirmation and these terms and conditions or any rights granted hereunder; provided, however, that User may assign such license in its entirety on written notice to CCC in the event of a transfer of all or substantially all of User's rights in the new material which includes the Work(s) licensed under this Service.

8.4. No amendment or waiver of any terms is binding unless set forth in writing and signed by the parties. The Rightsholder and CCC hereby object to any terms contained in any writing prepared by the User or its principals, employees, agents or affiliates and purporting to govern or otherwise relate to the licensing transaction described in the Order Confirmation, which terms are in any way inconsistent with any terms set forth in the Order Confirmation and/or in these terms and conditions or CCC's standard operating procedures, whether such writing is prepared prior to, simultaneously with or subsequent to the Order Confirmation, and whether such writing appears on a copy of the Order Confirmation or in a separate instrument.

8.5. The licensing transaction described in the Order Confirmation document shall be governed by and construed under the law of the State of New York, USA, without regard to the principles thereof of conflicts of law. Any case, controversy, suit, action, or proceeding arising out of, in connection with, or related to such licensing transaction shall be brought, at CCC's sole discretion, in any federal or state court located in the County of New York, State of New York, USA, or in any federal or state court whose geographical jurisdiction covers the location of the Rightsholder set forth in the Order Confirmation. The parties expressly submit to the personal jurisdiction and venue of each such federal or state court.If you have any comments or questions about the Service or Copyright Clearance Center, please contact us at 978-750-8400 or send an e-mail to support@copyright.com.

v 1.1

CCC | Marketplace™

Order Date	02-Mar-2022	Type of Use	Republish in a thesis/dissertation
Order License ID	1195054-1		
ISSN	1945-7111	Publisher	IOP Publishing
		Portion	Chapter/article

LICENSED CONTENT

Publication Title	Journal of the Electrochemical Society	Country	United States of America
		Rightsholder	IOP Publishing, Ltd
Author/Editor	Electrochemical Society.	Publication Type	e-Journal
Date	01/01/1948	URL	http://www.scitation.org/JES
Language	English		

REQUEST DETAILS

Portion Type	Chapter/article	Rights Requested	Main product
Page range(s)	A283-290	Distribution	Worldwide
Total number of pages	8	Translation	Original language of publication
Format (select all that apply)	Print, Electronic	Copies for the disabled?	No
Who will republish the content?	Author of requested content	Minor editing privileges?	No
Duration of Use	Life of current and all future editions	Incidental promotional use?	No
		Currency	USD
Lifetime Unit Quantity	Up to 499		

NEW WORK DETAILS

Title	DEVELOPMENT OF NANOCOMPOSITE ELECTRODES AND SEPARATORS FOR SUPERCAPACITORS	Institution name	Middle East Technical University
		Expected presentation date	2022-03-10
Instructor name	Alptekin AYDINLI		

ADDITIONAL DETAILS

Order reference number	N/A	The requesting person / organization to appear on the license	Alptekin AYDINLI

REUSE CONTENT DETAILS

Title, description or numeric reference of the portion(s)	All of the article	Title of the article/chapter the portion is from	Paper Based, Expanded Graphite/Polypyrrole Nanocomposite Supercapacitors Free from Binders and Current Collectors
Editor of portion(s)	N/A		

Volume of serial or monograph	N/A	Author of portion(s)	Electrochemical Society.
Page or page range of portion	A283-A290	Issue, if republishing an article from a serial	N/A
		Publication date of portion	2018-01-25

RIGHTSHOLDER TERMS AND CONDITIONS

These special terms and conditions are in addition to the standard terms and conditions for CCC's Republication Service and, together with those standard terms and conditions, govern the use of the Works. As the User you will make all reasonable efforts to contact the author(s) of the article which the Work is to be reused from, to seek consent for your intended use. Contacting one author who is acting expressly as authorised agent for their co-author(s) is acceptable. User will reproduce the following wording prominently alongside the Work: the source of the Work, including author, article title, title of journal, volume number, issue number (if relevant), page range (or first page if this is the only information available) and date of first publication; and a link back to the article (via DOI); and if practicable, and IN ALL CASES for new works published under any of the Creative Commons licences, the words "© The Electrochemical Society. Reproduced by permission of IOP Publishing Ltd. All rights reserved" Without the express permission of the author(s) and the Rightsholder of the article from which the Work is to be reused, User shall not use it in any way which, in the opinion of IOP Publishing Ltd, could: (i) distort or alter the author(s)' original intention(s) and meaning; (ii) be prejudicial to the honour or reputation of the author(s); and/or (iii) imply endorsement by the author(s) and/or the Rightsholder and/or IOP Publishing Ltd. This licence does not apply to any article which is credited to another source and which does not have the copyright line '© The Electrochemical Society'. User must check the copyright line of the article from which the Work is to be reused to check that the Electrochemical Society and IOP Publishing Ltd has all the necessary rights to be able to grant permission. User is solely responsible for identifying and obtaining separate licences and permissions from the copyright owner for reuse of any such third party material/figures which the Rightsholder is not the copyright owner of. The Rightsholder shall not reimburse any fees which User pays for a republication license for such third party content. This licence does not apply to any material/figure which is credited to another source in the Rightsholder's publication or has been obtained from a third party. User must check the Version of Record of the article from which the Work is to be reused, to check whether any of the material in the Work is third party material. Third party citations and/or copyright notices and/or permissions statements may not be included in any other version of the article from which the Work is to be reused and so cannot be relied upon by the User. User is solely responsible for identifying and obtaining separate licences and permissions from the copyright owner for reuse of any such third party material/figures where the Rightsholder is not the copyright owner. The Rightsholder shall not reimburse any fees which User pays for a republication license for such third party content. User and CCC acknowledge that IOP Publishing Ltd and/or the Rightsholder may, from time to time, make changes or additions to these special terms and conditions without express notification, provided that these shall not apply to permissions already secured and paid for by User prior to such change or addition. User acknowledges that the Rightsholder and IOP Publishing Ltd (which includes companies within its group and third parties for whom it publishes its titles) may make use of personal data collected through the service in the course of their business. If User is the author of the Work, User may automatically have the right to reuse it under the rights granted back when User transferred the copyright in the article to the Rightsholder. User should check the copyright form and the relevant author rights policy to check whether permission is required. If User is the author of the Work and does require permission for proposed reuse of the Work, User should select 'Author of requested content' as the Requestor Type. The Rightsholder shall not reimburse any fees which User pays for a republication license. If User is the author of the article which User wishes to reuse in User's thesis or dissertation, the republication licence covers the right to include the Version of Record of the article, provided it is not then published commercially. User must include citation details and, for online use, a link to the Version of Record of the article on the IOPscience website. User may need to obtain separate permission for any third party content included within the article. User must check this with the copyright owner of such third party content. User may not include the article in a thesis or dissertation which is published by ProQuest. Any other commercial use of User's thesis or dissertation containing the article would also need to be expressly notified in writing to the Rightsholder at the time of request and would require separate written permission from the Rightsholder. As well as CCC, the Rightsholder and IOP Publishing Ltd shall have the right to bring any legal action that they deem necessary to enforce their rights should they consider that the Work infringes those rights in any way. For content reuse requests that qualify for permission under the STM Permissions Guidelines, which may be updated from time to time, the STM Permissions Guidelines supplement the terms and conditions contained in this license.

SPECIAL RIGHTSHOLDER TERMS AND CONDITIONS

When you transferred the copyright in your article to The Electrochemical Society, we granted back to you certain rights, including the right to include all or part of the Final Published Version of the article within any thesis or dissertation. Please note you may need to obtain separate permission for any third party content you included within your article. Please include citation details, "©The Electrochemical Society. Reproduced with permission. All rights reserved" and for online use, a link to the Version of Record. The only restriction is that if, at a later date, you wanted your thesis/dissertation to be published commercially, further permission would be required.

CCC Terms and Conditions

1. Description of Service; Defined Terms. This Republication License enables the User to obtain licenses for republication of one or more copyrighted works as described in detail on the relevant Order Confirmation (the "Work(s)"). Copyright Clearance Center, Inc. ("CCC") grants licenses through the Service on behalf of the rightsholder identified on the Order Confirmation (the "Rightsholder"). "Republication", as used herein, generally means the inclusion of a Work, in whole or in part, in a new work or works, also as described on the Order Confirmation. "User", as used herein, means the person or entity making such republication.

2. The terms set forth in the relevant Order Confirmation, and any terms set by the Rightsholder with respect to a particular Work, govern the terms of use of Works in connection with the Service. By using the Service, the person transacting for a republication license on behalf of the User represents and warrants that he/she/it (a) has been duly authorized by the User to accept, and hereby does accept, all such terms and conditions on behalf of User, and (b) shall inform User of all such terms and conditions. In the event such person is a "freelancer" or other third party independent of User and CCC, such party shall be deemed jointly a "User" for purposes of these terms and conditions. In any event, User shall be deemed to have accepted and agreed to all such terms and conditions if User republishes the Work in any fashion.

3. Scope of License; Limitations and Obligations.

   3.1. All Works and all rights therein, including copyright rights, remain the sole and exclusive property of the Rightsholder. The license created by the exchange of an Order Confirmation (and/or any invoice) and payment by User of the full amount set forth on that document includes only those rights expressly set forth in the Order Confirmation and in these terms and conditions, and conveys no other rights in the Work(s) to User. All rights not expressly granted are hereby reserved.

   3.2. General Payment Terms: You may pay by credit card or through an account with us payable at the end of the month. If you and we agree that you may establish a standing account with CCC, then the following terms apply: Remit Payment to: Copyright Clearance Center, 29118 Network Place, Chicago, IL 60673-1291. Payments Due: Invoices are payable upon their delivery to you (or upon our notice to you that they are available to you for downloading). After 30 days, outstanding amounts will be subject to a service charge of 1-1/2% per month or, if less, the maximum rate allowed by applicable law. Unless otherwise specifically set forth in the Order Confirmation or in a separate written agreement signed by CCC, invoices are due and payable on "net 30" terms. While User may exercise the rights licensed immediately upon issuance of the Order Confirmation, the license is automatically revoked and is null and void, as if it had never been issued, if complete payment for the license is not received on a timely basis either from User directly or through a payment agent, such as a credit card company.

   3.3. Unless otherwise provided in the Order Confirmation, any grant of rights to User (i) is "one-time" (including the editions and product family specified in the license), (ii) is non-exclusive and non-transferable and (iii) is subject to any and all limitations and restrictions (such as, but not limited to, limitations on duration of use or circulation) included in the Order Confirmation or invoice and/or in these terms and conditions. Upon completion of the licensed use, User shall either secure a new permission for further use of the Work(s) or immediately cease any new use of the Work(s) and shall render inaccessible (such as by deleting or by removing or severing links or other locators) any further copies of the Work (except for copies printed on paper in accordance with this license and still in User's stock at the end of such period).

   3.4. In the event that the material for which a republication license is sought includes third party materials (such as photographs, illustrations, graphs, inserts and similar materials) which are identified in such material as having been used by permission, User is responsible for identifying, and seeking separate licenses (under this Service or otherwise) for, any of such third party materials; without a separate license, such third party materials may not be used.

   3.5. Use of proper copyright notice for a Work is required as a condition of any license granted under the Service. Unless otherwise provided in the Order Confirmation, a proper copyright notice will read substantially as follows: "Republished with permission of [Rightsholder's name], from [Work's title, author, volume, edition number and year of copyright]; permission conveyed through Copyright Clearance Center, Inc. " Such notice must be provided in a reasonably legible font size and must be placed either immediately adjacent to the Work as used (for example, as part of a by-line or footnote but not as a separate electronic link) or in the place where substantially all other credits or notices for the new work containing the republished Work are located. Failure to include the required notice results in loss to the Rightsholder and CCC, and the User shall be liable to pay liquidated damages for each such failure equal to twice the use fee specified in the Order Confirmation, in addition to the use fee itself and any other fees and charges specified.

   3.6.

User may only make alterations to the Work if and as expressly set forth in the Order Confirmation. No Work may be used in any way that is defamatory, violates the rights of third parties (including such third parties' rights of copyright, privacy, publicity, or other tangible or intangible property), or is otherwise illegal, sexually explicit or obscene. In addition, User may not conjoin a Work with any other material that may result in damage to the reputation of the Rightsholder. User agrees to inform CCC if it becomes aware of any infringement of any rights in a Work and to cooperate with any reasonable request of CCC or the Rightsholder in connection therewith.

4. Indemnity. User hereby indemnifies and agrees to defend the Rightsholder and CCC, and their respective employees and directors, against all claims, liability, damages, costs and expenses, including legal fees and expenses, arising out of any use of a Work beyond the scope of the rights granted herein, or any use of a Work which has been altered in any unauthorized way by User, including claims of defamation or infringement of rights of copyright, publicity, privacy or other tangible or intangible property.

5. Limitation of Liability. UNDER NO CIRCUMSTANCES WILL CCC OR THE RIGHTSHOLDER BE LIABLE FOR ANY DIRECT, INDIRECT, CONSEQUENTIAL OR INCIDENTAL DAMAGES (INCLUDING WITHOUT LIMITATION DAMAGES FOR LOSS OF BUSINESS PROFITS OR INFORMATION, OR FOR BUSINESS INTERRUPTION) ARISING OUT OF THE USE OR INABILITY TO USE A WORK, EVEN IF ONE OF THEM HAS BEEN ADVISED OF THE POSSIBILITY OF SUCH DAMAGES. In any event, the total liability of the Rightsholder and CCC (including their respective employees and directors) shall not exceed the total amount actually paid by User for this license. User assumes full liability for the actions and omissions of its principals, employees, agents, affiliates, successors and assigns.

6. Limited Warranties. THE WORK(S) AND RIGHT(S) ARE PROVIDED "AS IS". CCC HAS THE RIGHT TO GRANT TO USER THE RIGHTS GRANTED IN THE ORDER CONFIRMATION DOCUMENT. CCC AND THE RIGHTSHOLDER DISCLAIM ALL OTHER WARRANTIES RELATING TO THE WORK(S) AND RIGHT(S), EITHER EXPRESS OR IMPLIED, INCLUDING WITHOUT LIMITATION IMPLIED WARRANTIES OF MERCHANTABILITY OR FITNESS FOR A PARTICULAR PURPOSE. ADDITIONAL RIGHTS MAY BE REQUIRED TO USE ILLUSTRATIONS, GRAPHS, PHOTOGRAPHS, ABSTRACTS, INSERTS OR OTHER PORTIONS OF THE WORK (AS OPPOSED TO THE ENTIRE WORK) IN A MANNER CONTEMPLATED BY USER; USER UNDERSTANDS AND AGREES THAT NEITHER CCC NOR THE RIGHTSHOLDER MAY HAVE SUCH ADDITIONAL RIGHTS TO GRANT.

7. Effect of Breach. Any failure by User to pay any amount when due, or any use by User of a Work beyond the scope of the license set forth in the Order Confirmation and/or these terms and conditions, shall be a material breach of the license created by the Order Confirmation and these terms and conditions. Any breach not cured within 30 days of written notice thereof shall result in immediate termination of such license without further notice. Any unauthorized (but licensable) use of a Work that is terminated immediately upon notice thereof may be liquidated by payment of the Rightsholder's ordinary license price therefor; any unauthorized (and unlicensable) use that is not terminated immediately for any reason (including, for example, because materials containing the Work cannot reasonably be recalled) will be subject to all remedies available at law or in equity, but in no event to a payment of less than three times the Rightsholder's ordinary license price for the most closely analogous licensable use plus Rightsholder's and/or CCC's costs and expenses incurred in collecting such payment.

8. Miscellaneous.

   8.1. User acknowledges that CCC may, from time to time, make changes or additions to the Service or to these terms and conditions, and CCC reserves the right to send notice to the User by electronic mail or otherwise for the purposes of notifying User of such changes or additions; provided that any such changes or additions shall not apply to permissions already secured and paid for.

   8.2. Use of User-related information collected through the Service is governed by CCC's privacy policy, available online here:https://marketplace.copyright.com/rs-ui-web/mp/privacy-policy

   8.3. The licensing transaction described in the Order Confirmation is personal to User. Therefore, User may not assign or transfer to any other person (whether a natural person or an organization of any kind) the license created by the Order Confirmation and these terms and conditions or any rights granted hereunder; provided, however, that User may assign such license in its entirety on written notice to CCC in the event of a transfer of all or substantially all of User's rights in the new material which includes the Work(s) licensed under this Service.

   8.4. No amendment or waiver of any terms is binding unless set forth in writing and signed by the parties. The Rightsholder and CCC hereby object to any terms contained in any writing prepared by the User or its principals, employees, agents or affiliates and purporting to govern or otherwise relate to the licensing

transaction described in the Order Confirmation, which terms are in any way inconsistent with any terms set forth in the Order Confirmation and/or in these terms and conditions or CCC's standard operating procedures, whether such writing is prepared prior to, simultaneously with or subsequent to the Order Confirmation, and whether such writing appears on a copy of the Order Confirmation or in a separate instrument.

8.5. The licensing transaction described in the Order Confirmation document shall be governed by and construed under the law of the State of New York, USA, without regard to the principles thereof of conflicts of law. Any case, controversy, suit, action, or proceeding arising out of, in connection with, or related to such licensing transaction shall be brought, at CCC's sole discretion, in any federal or state court located in the County of New York, State of New York, USA, or in any federal or state court whose geographical jurisdiction covers the location of the Rightsholder set forth in the Order Confirmation. The parties expressly submit to the personal jurisdiction and venue of each such federal or state court.If you have any comments or questions about the Service or Copyright Clearance Center, please contact us at 978-750-8400 or send an e-mail to support@copyright.com.

v 1.1

CURRICULUM VITAE

Alptekin AYDINLI

EDUCATION

Doctor of Philosophy,	**Middle East Technical University, Turkey** Metallurgical and Materials Eng. (02.2015-02.2022) *Thesis title: Development of Nanocomposite Electrodes and Separators for Supercapacitors* *Supervisor: Prof. Dr. Hüsnü Emrah Ünalan*
Master of Science,	**Middle East Technical University, Turkey** Micro and Nanotechnology (09.2010-07.2013) *Thesis title: Hydrogen Decrepitation of Magnesium-Rich Intermetallics* *Supervisor: Prof. Dr. Tayfur Öztürk*
Bachelor of Science,	**İstanbul University, Turkey** Metallurgical and Materials Eng. (09.2006-06.2010)

RESEARCH EXPERIENCE

02.2012 – 12.2012	**Middle East Technical University, TÜBİTAK Project** Funded project assistant *Project title: Combinatorial search for hydrogen separation membranes*
02.2015 – 03.2022	**Middle East Technical University, Department of Metallurgical and Materials Engineering** Research assistant
12.2015 – 03.2017	**Middle East Technical University, TÜBİTAK Project** Funded project assistant *Project title: Development of supercapacitors with carbon nanotubes*
10.2019 – 10.2020	**Drexel University, USA, TÜBİTAK Scholarship Program** Visiting researcher *Research title: Using of hexagonal boron nitride in supercapacitors* *Supervisor: Prof. Dr. Yury Gogotsi*

03.2022 – **Adana Alparslan Türkeş Science and Technology University, Department of Materials Science and Engineering**
Research assistant

PUBLICATIONS

- **AYDINLI ALPTEKİN**, AKTEKİN BURAK, ÖZTÜRK TAYFUR (2015). Size reduction in Mg rich intermetallics via hydrogen decrepitation. Journal of Alloys and Compounds, 645, 27-31., Doi: 10.1016/j.jallcom.2015.01.260
- YÜKSEL RECEP, UYSAL NİLPERİ, **AYDINLI ALPTEKİN**, ÜNALAN HÜSNÜ EMRAH (2018). Paper Based, Expanded Graphite/Polypyrrole Nanocomposite Supercapacitors Free from Binders and Current Collectors. Journal of The Electrochemical Society, 165(2), 283-290., Doi: 10.1149/2.1051802jes
- **AYDINLI ALPTEKİN**, YÜKSEL RECEP, ÜNALAN HÜSNÜ EMRAH (2018). Vertically aligned carbon nanotube – Polyaniline nanocomposite supercapacitor electrodes. International Journal of Hydrogen Energy, 43(40), 18617-18625., Doi: 10.1016/j.ijhydene.2018.05.126
- **AYDINLI ALPTEKİN**, ÇAKMAK GÜLHAN, ÖZTÜRK TAYFUR, ÜNALAN HÜSNÜ EMRAH (2019). Nanocomposite supercapacitor electrodes based on carbon nanoflakes produced by induction coupled plasma and manganese dioxide. mESC-IS, 4th Int. Symposium on Materials for Energy Storage and Conversion, 64-70.

PRESENTATIONS

- **AYDINLI ALPTEKİN**, ÖZTÜRK TAYFUR (2012). Production of Hydrogen Storage Alloys via Decrepitation Treatment. NanoTR, 8th Nanoscience and Nanotechnology Congress, Ankara, Turkey (Oral Presentation)
- **AYDINLI ALPTEKİN**, ÖZTÜRK TAYFUR (2012). Hydrogen Decrepitation of Mg_2Ni and $TiMn_{1.6}Ni_{0.4}$. International Symposium on Metal-Hydrogen Systems, Kyoto, Japan (Poster Presentation)
- **AYDINLI ALPTEKİN**, AKTEKİN BURAK, ÖZTÜRK TAYFUR (2015). Hydrogen decrepitation of Mg rich Intermetallics. International Symposium on Materials for Energy Storage and Conversion, Ankara, Turkey (Oral Presentation)
- **AYDINLI ALPTEKİN**, YÜKSEL RECEP, ÜNALAN HÜSNÜ EMRAH (2016). Graphene-Polypyrrole Nanocomposite Electrodes for Paper-Based Supercapacitors. MRS Fall Meeting and Exhibit, Boston, USA (Poster Presentation)
- **AYDINLI ALPTEKİN**, YÜKSEL RECEP, ÜNALAN HÜSNÜ EMRAH (2016). Vertically Aligned Carbon Nanotube—Polyaniline Nanocomposite

Electrodes for Supercapacitors. MRS Fall Meeting and Exhibit, Boston, USA (Poster Presentation)

- **AYDINLI ALPTEKİN**, YÜKSEL RECEP, ÜNALAN HÜSNÜ EMRAH (2017). Carbon Nanotube - Polyaniline Nanocomposite Supercapacitor Electrodes. mESC-IS, 2nd Int. Symposium on Materials for Energy Storage and Conversion, Cappadocia, Turkey (Oral Presentation)
- **AYDINLI ALPTEKİN**, YÜKSEL RECEP, ÜNALAN HÜSNÜ EMRAH (2017). Polyaniline - Carbon Nanotube Nanocomposite Electrodes for Supercapacitors. NanoTR, 13th Nanoscience and Nanotechnology Conference of Turkey, Antalya, Turkey (Oral Presentation)
- YÜKSEL RECEP, UYSAL NILPERI, **AYDINLI ALPTEKİN**, ÜNALAN HÜSNÜ EMRAH (2018). Expanded Graphite /Polypyrrole Nanocomposite Supercapacitors on Paper. mESC-IS, 3rd Int. Symposium on Materials for Energy Storage and Conversion, Belgrade, Serbia (Oral Presentation)
- **AYDINLI ALPTEKİN**, ÇAKMAK GÜLHAN, ÖZTÜRK TAYFUR, ÜNALAN HÜSNÜ EMRAH (2018). Supercapacitor electrodes with graphene synthesized via induction couple plasma. mESC-IS, 3rd Int. Symposium on Materials for Energy Storage and Conversion, Belgrade, Serbia (Oral Presentation)
- **AYDINLI ALPTEKİN**, DOĞAN ÖZNUR, KOYLAN SERKAN, BAT ERHAN, ÜNALAN HÜSNÜ EMRAH (2018). Reduced Graphene Oxide Aerogel – Molybdenum Disulfide Supercapacitor Electrodes on Nickel Foams. NanoTR, 14th Nanoscience and Nanotechnology Conference of Turkey, İzmir, Turkey (Oral Presentation)
- **AYDINLI ALPTEKİN**, DOĞAN ÖZNUR, KOYLAN SERKAN, BAT ERHAN, ÜNALAN HÜSNÜ EMRAH (2018). Reduced Graphene Oxide - Molybdenum Disulfide Aerogel Nanocomposite Electrodes for Supercapacitors. MRS Fall Meeting and Exhibit, Boston, USA (Poster Presentation)
- **AYDINLI ALPTEKİN**, ÇAKMAK GÜLHAN, ÖZTÜRK TAYFUR, ÜNALAN HÜSNÜ EMRAH (2019). Nanocomposite supercapacitor electrodes based on carbon nanoflakes produced by induction coupled plasma and manganese dioxide. mESC-IS, 4th Int. Symposium on Materials for Energy Storage and Conversion, Akyaka, Turkey (Oral Presentation)
- **AYDINLI ALPTEKİN**, ÜNALAN HÜSNÜ EMRAH (2019). 2D Hexagonal Boron Nitride – Molybdenum Disulfide Nanocomposite Supercapacitor Electrodes. MRS Fall Meeting and Exhibit, Boston, USA (Poster Presentation)
- **AYDINLI ALPTEKİN**, WANG XUEHANG, ÜNALAN HÜSNÜ EMRAH, GOGOTSI YURY (2020). Dielectric h-BN separators for Ti_3C_2-MnO_2 supercapacitors. Virtual MRS Spring/Fall Meeting and Exhibit, Online (Poster Presentation)
- **AYDINLI ALPTEKİN**, WANG XUEHANG, ÜNALAN HÜSNÜ EMRAH, GOGOTSI YURY (2021). Ti_3C_2 MXene Supercapacitor with

Thin Film h-BN Separator. mESC-IS, 5th Int. Symposium on Materials for Energy Storage and Conversion, Online (Oral Presentation)